8-2013

# DETAILED GEOLOGIC STUDIES OF PALEOSEISMIC FEATURES EXPOSED AT SITES IN THE EAST TENNESSEE SEISMIC ZONE: EVIDENCE FOR LARGE, PREHISTORIC EARTHQUAKES

Kathleen Frances Warrell
kwarrell@utk.edu

To the Graduate Council:

I am submitting herewith a thesis written by Kathleen Frances Warrell entitled "DETAILED GEOLOGIC STUDIES OF PALEOSEISMIC FEATURES EXPOSED AT SITES IN THE EAST TENNESSEE SEISMIC ZONE: EVIDENCE FOR LARGE, PREHISTORIC EARTHQUAKES." I have examined the final electronic copy of this thesis for form and content and recommend that it be accepted in partial fulfillment of the requirements for the degree of Master of Science, with a major in Geology.

Robert D. Hatcher Jr., Major Professor

We have read this thesis and recommend its acceptance:

James A. Mason, Gregory S. Baker

Accepted for the Council:
Carolyn R. Hodges

Vice Provost and Dean of the Graduate School

(Original signatures are on file with official student records.)

# DETAILED GEOLOGIC STUDIES OF PALEOSEISMIC FEATURES EXPOSED AT SITES IN THE EAST TENNESSEE SEISMIC ZONE: EVIDENCE FOR LARGE, PREHISTORIC EARTHQUAKES

A Thesis Presented for the
Master of Science
Degree
The University of Tennessee, Knoxville

Kathleen Frances Warrell
August 2013

## *DEDICATION*

I would like to dedicate this thesis to Dr. Kurt Frankel, who was a great teacher, mentor, and champion for all things geological. His life was tragically cut short by a bicycle accident on July 2, 2011. I hope that one day I will inspire students with the same passion and enthusiasm for science that came so easily to Kurt and live up to the example he set.

## *ACKNOWLEDGMENTS*

I would like to thank Dr. Robert D. Hatcher, Jr., for all of his guidance and support throughout this project. He took my mixed background in environmental sciences and helped me to become a geologist. I would also like to thank Dr. Gregory Baker and Dr. James Mason for their support and criticisms while on my committee. They have provided unique insights into this project. The co-PI's on this project greatly deserve my thanks: Dr. Randy Cox, James Vaughn, Dr. Steven Obermeier, and Ronald Counts.

I owe a great deal of gratitude to the Nuclear Regulatory Commission for their financial support of this project, with special thanks to Dr. Gerry Stirewalt and Dr. Alice Stevie for their input and enthusiasm. The UTK Department of Earth and Planetary Sciences and UTK Science Alliance Center for Excellence have also provided funding along the way, for which I am grateful. Additional thanks goes to all of the contributors to the George D. Swingle Fellowship for Excellence in Geological Field Research.

I would like to thank Nancy Meadows for all of her editing prowess, interesting conversations, and supply of chocolate. She is an invaluable resource to us all. I would also like to thank Andrew Wunderlich for putting up with all of my questions about various computer programs; the figures in thesis would not be nearly as aesthetically pleasing without his help. I especially want to thank those who have sacrificed their shoes to the mud to help me in the field: Mary Biswal, Annie Walker, Andrew Wunderlich, and Annie Blankenship. Additional thanks goes to Chris Howard and Phillip Derryberry for their contributions to the pilot study. I also thank my support system, the Hatchery graduate students who have kept me motivated all this time. Last but not least, I want to thank my family for their support and encouragement.

## *ABSTRACT*

The East Tennessee seismic zone (ETSZ) is the second most active in the eastern United States, but recorded earthquakes do not exceed $M_w$ [moment magnitude] = 4.6. Earthquake epicenters are located 5-26 kilometers deep in autochthonous basement, and faults producing these earthquakes do not break the surface. Detailed paleoseismic investigations at sites within the ETSZ include: detailed geological mapping, trenching, aerial photograph reconnaissance, X-ray diffraction (XRD), grain-size analysis, and optically stimulated luminescence dating of alluvium.

Site DL-6 near Dandridge, Tennessee, reveals a complex array of features providing evidence that at least 4–6 $M_w > 6$ earthquakes affected the area. A thrust fault with ~1 meter displacement is traceable for ~50 meters in the mapped area from Quaternary terrace sediments into Ordovician Sevier Shale saprolite where it develops multiple splays. This fault truncates a 30 centimeter-wide Quaternary sediment-filled fissure; the fissure is also offset ~10 centimeters by a small strike-slip fault that truncates against a splay of the main thrust fault. The fissure may be traceable for over 2 kilometers across Douglas Reservoir. Fault surface and slickenline orientations indicate west-vergent slip on many thrust splay surfaces. Fracture orientations measured at site DL-6 are close to those in Sevier Shale here; reactivation of near-vertical fractures is mostly strike-slip. Additionally, shale chips in Quaternary sediment at a nearby site at Dandridge, Tennessee, contain the same mineralogy as underlying Sevier Shale, indicating that these chips may have been liquefied and brought up through Quaternary terrace sediments during an earthquake.

Sites along the Chattooga River near Lyerly, Georgia, provide evidence for at least one

$M_w$ > 6 earthquake. Sand dikes emanating from a source bed in a cut bank contain liquefiable sediments that intruded overlying cap sediments; grain-size and XRD analyses suggest cap sediments are more clay-rich than source or dike sediments. Aerial photographs of the area contain elliptical discontinuities that may represent sand blow deposits. Field reconnaissance of the area identified possible feeder dikes to sand blows; further investigation is required.

Collectively, these data provide substantial evidence for the occurrence of $M_w$ > 6 earthquakes in the ETSZ, and motivate further paleoseismic studies here.

## *TABLE OF CONTENTS*

## *LIST OF FIGURES*

## *LIST OF ATTACHMENTS*

# *CHAPTER I*

# *INTRODUCTION*

## Present Investigation

Large intraplate earthquakes in the eastern United States are an enigma that geologists and seismologists have long attempted to understand (e.g., Tavakoli et al., 2010). Large earthquakes in the eastern United States are of particular interest, because damage from a M 4.5–7.5 earthquake can affect an area five times larger than an earthquake of equal magnitude in the western United States (Bollinger et al., 1993). The East Tennessee seismic zone (ETSZ) is one of the most active seismic zones in the eastern United States, second to the New Madrid seismic zone (Powell et al., 1994). The ETSZ encompasses a 50 km wide and 300 km long area, and extends from northeastern Alabama and northwestern Georgia into eastern Tennessee to just northeast of Knoxville (Fig. 1-1). Earthquakes in the ETSZ occur in autochthonous basement beneath the Appalachian foreland fold-thrust belt with most epicenters at depths of 5 to 26 km, but no M > 5 earthquakes have been recorded since European settlement ~300 years ago (Chapman et al., 1997). No major faults originating in the basement have been found that break the surface in the ETSZ. As a result, evidence for large earthquakes in the ETSZ must be sought by means of paleoseismic investigations.

This research was part of an ongoing study funded by the Nuclear Regulatory Commission wherein the ultimate goal is to determine: (1) the largest magnitude earthquakes that have occurred in the ETSZ, and (2) recurrence intervals for these earthquakes, as well as to investigate possible seismicity mechanisms. Results from the pilot study reported by Hatcher et

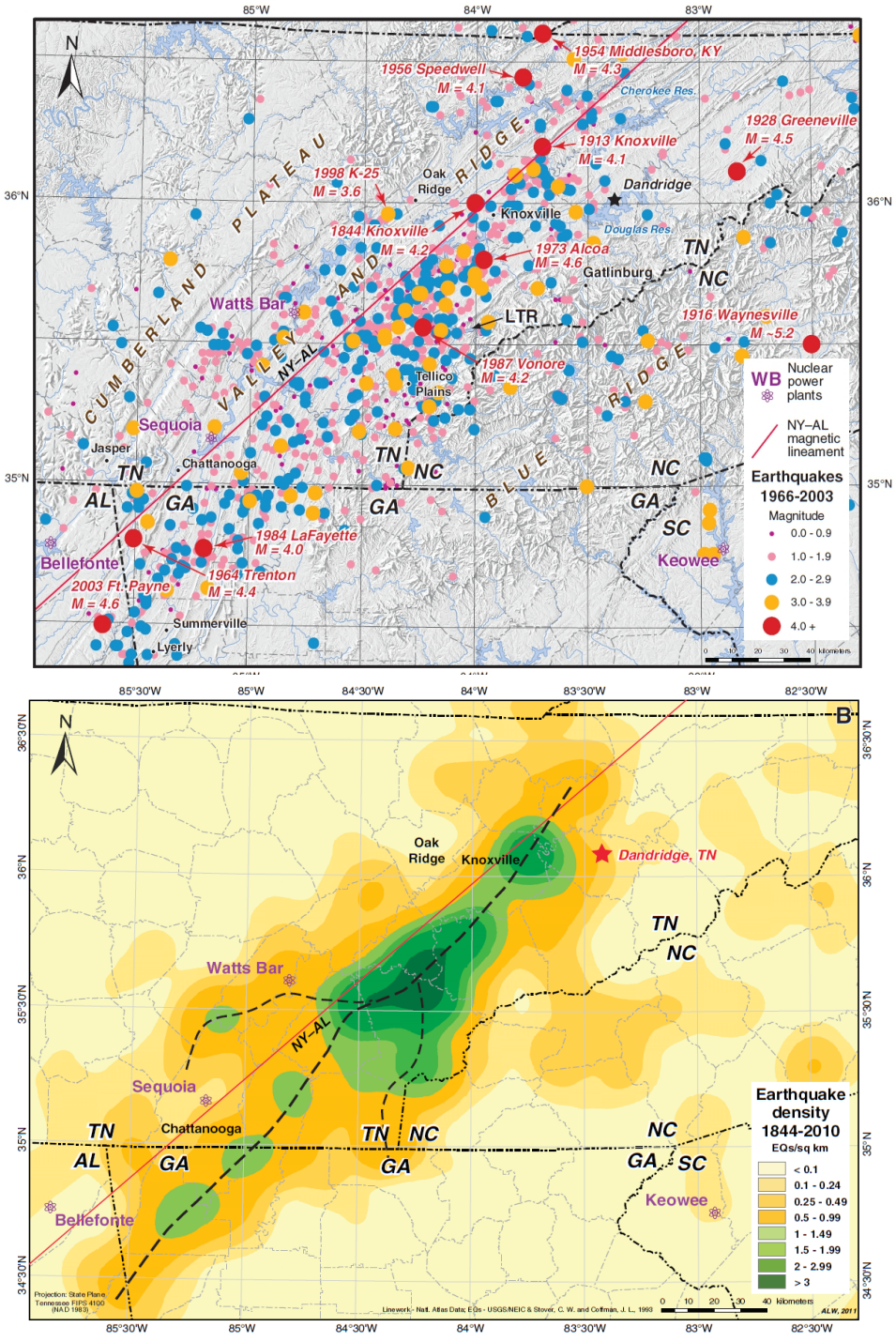


**Figure 1-1.** Earthquake epicenters and earthquake density in the ETSZ. The NY-AL lineament is depicted on both maps by a red line. (A) Location of Dandridge, TN, (black star) where a large part of the data in this study have been found. Lyerly, Georgia, is also located on this map. (B) Earthquake density map contoured using the Spatial Analyst extension of ArcGIS[tm]; areas of greatest earthquake density are connected by dashed black lines. (From Hatcher et al., 2012.)

al. (2012) are included later in this chapter. The purpose of this research is to present paleoseismic evidence for large, prehistoric (earlier than circa AD 1700) earthquakes in the ETSZ by identifying and analyzing recent coseismic faults and other paleoseismically generated features, such as liquefaction. This has been accomplished using a variety of methods: (1) identification of possible paleoseismic features on vintage aerial photographs; (2) reconnaissance of Quaternary sediments on foot and by boat; (3) areal- and trench-mapping of paleoseismic features; and (4) X-ray diffraction and grain-size analyses to characterize sediments.

## Geologic Setting

The locus of the ETSZ lies west of the Great Smoky fault in the foreland fold-thrust belt; the foreland fold-thrust belt is comprised of a series of Cambrian through Pennsylvanian sedimentary rocks that were deposited on undeformed basement following rifting of supercontinent Rodinia (Hatcher et al., 2007a). These rocks include a mixture of both siliciclastic and carbonate rocks; deformation producing the foreland fold-thrust belt occurred during the Alleghanian orogeny (325-260 Ma) (Hatcher et al., 2007a). Paleozoic faults are not related to the seismicity in the ETSZ, because hypocenters of the earthquakes lie 5 to 26 km below the ground surface within the Precambrian basement (Vlahovic et al., 1998), the top of which lies 3 to 6 km below the surface (Hatcher et al., 2007b).

Karst is a common feature in areas underlain by limestone or dolostone, and the structures identified around a sinkhole may mimic paleoseismic features; for this reason, field areas in this study have been chosen where the effects of karst activity are minimal. Fetter (2001) suggested that major karst openings are uncommon beyond 200 m below the water table,

although this is not always true. If a carbonate unit exists below a site of interest, the top of it must be located sufficiently below the water table, which is defined as the lake or river level in this study.

## Paleoseismic Features

Paleoseismic features are features found in sediments and rocks and were produced by an earthquake. While the study of paleoseismic features is not limited to earthquakes occurring prior to human settlement (e.g., the 1811-1812 New Madrid earthquakes are well recorded by people living in and around the area, and they have been the subject of extensive paleoseismic studies), paleoseismic features do provide valuable evidence for earthquakes that occurred before humans could record them. Paleoseismic features can be classified as primary or secondary: primary features are the direct result of movement along a fault, whereas secondary features are the result of coseismic shaking or erosional and depositional responses to the shaking (McCalpin and Nelson, 2009). All known paleoseismic features in the ETSZ are secondary: they record the response of surface materials to shaking originating from earthquakes at depths of 5 km or more. No primary fault that would extend to 5 km depth has been found to date (Hatcher et al., 2012; Warrell et al., 2012).

For the purpose of this study, secondary features have been classified as structural or liquefaction features. Structural features include faults, folds, and fractures. Hatcher et al. (2012) identified strike-slip, normal, and thrust faults, fractured alluvium, and branching fissures in bedrock filled with late Quaternary alluvium. Numerous small faults of unknown age occur in the bedrock in this area, so to ensure that structural features are related only to Quaternary seismic activity and not Paleozoic seismic activity, features that involve Quaternary sediments

were used in this study.

Liquefaction features include both large- and small-scale sand blows, sand dikes, and soft-sediment deformation. Liquefaction occurs where shear stress builds up in saturated, cohesionless sediments to the extent that the increased shear stress causes an increase in the pore-water pressure sufficient to overcome the normal stress acting on the sediment such that the grains are supported by pore water; this liquefied sediment vents to the surface through holes or fractures (Fig. 1-2) (Obermeier, 2009). The amount of energy required to liquefy and vent sediments is fairly high: a minimum of a $M_w = 6$ earthquake is required (Obermeier, 2009). If the liquefied sediment is overlain by a more cohesive fine-grained cap, more pressure will build up and cause the sediment to vent forcefully to the surface and form a sand blow, which has a triangular volcano-like shape in cross section, and can be up to one meter high and ten meters wide (Fig. 1-2) (Obermeier et al., 2005). Sand blows are often eroded or plowed away, and the only remaining evidence is the decapitated clastic dike through which the liquefied sand was transported (Obermeier et al., 2005). The formation of craters has also been associated with coseismic liquefaction; as underlying liquefied sand vents to the surface, it may erode and incorporate a larger volume of overlying sediments to produce a crater (Obermeier, 2009). In cross section, craters are bowl-shaped features that truncate the original layering of sediments and are filled with a mixture of sand and rip-up clasts of the surrounding strata that may fine upward; a clastic dike is often associated with crater structures (Obermeier, 2009). Small-scale liquefaction-induced features can often be found in association with the aforementioned large-scale features. These small-scale features are mm to cm-scale and include hydraulically fractured sediments, emplaced sediment sills, small clastic dikes, and bulbous intrusions of

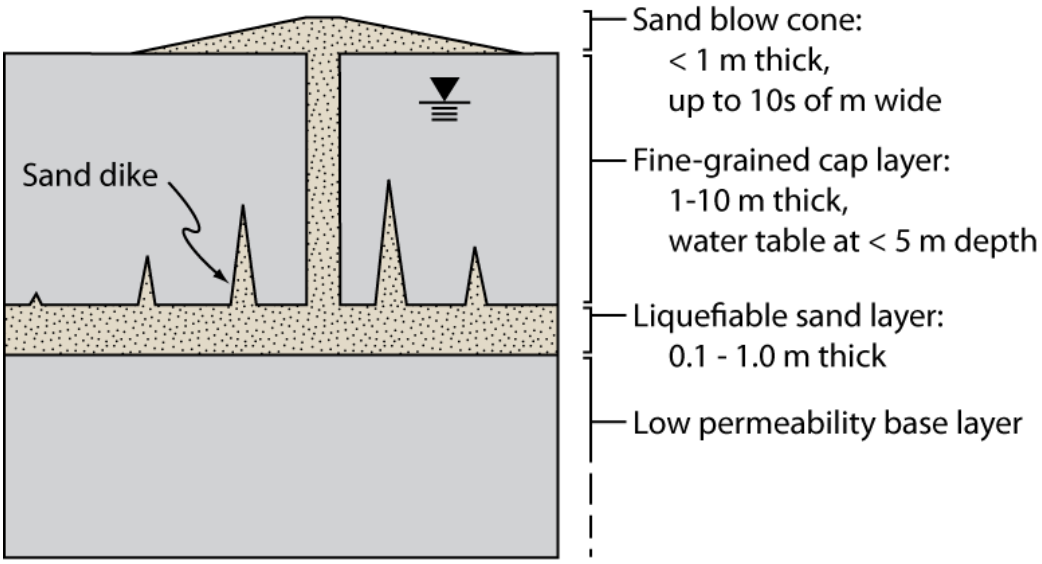


**Figure 1-2.** Typical liquefaction features, including sand dikes and a sand blow, and relative thicknesses. The bottom tip of the black triangle represents the top of the water table. (Adapted from Obermeier, 2009.)

sediments (Counts and Obermeier, 2012). Care must be taken when analyzing features to ensure that small-scale features are not the result of some other process, such as wetting and drying or animal burrowing. Sand dikes and a boat-shaped fluidization structure containing many small-scale, liquefaction-induced features have been identified in the ETSZ (Hatcher et al., 2012; Warrell et al., 2012).

Susceptibility to liquefaction is affected by sediment characteristics, local stratigraphy, and local hyrdogeologic factors. Sediments that readily liquefy often occur within a narrow range of grain sizes (Fig. 1-3A), and a wider range of grain sizes has been used to describe potentially liquefiable sediments (Tsuchida and Hayashi, 1971). To liquefy, the sediment must have minimal cohesion, so the clay content of the sediment must be less than 15 percent (Seed et al., 1983). Sediments where the liquefied layer is overlain by a fine-grained cap layer with significantly more cohesion are more likely to build up pressure and hydraulically fracture the cap during a seismic event; similarly, if the liquefied layer is underlain by a medium with a much lower permeability (e.g., another clay layer), liquefaction is much more likely (Obermeier, 2009). In hydraulic fracturing, the susceptible thickness of the liquefied layer is proportional to that of the overlying fine-grained cap; the ratio between these was described by Ishihara (1985) (Fig. 1-3B). Liquefiable sediments must be water saturated to build up significant pore fluid pressure and, as such, depth to the water table is a major factor in liquefaction susceptibility; succeptibility is significantly diminished in areas where the water table depth is greater than 5 m (Obermeier, 2009). After liquefaction occurs, the porosity of a liquefied layer generally decreases, which decreases the future susceptibility of that layer to liquefaction (Obermeier, 2009). Soil development and compaction also affect liquefaction susceptibility, as these reduce

A.

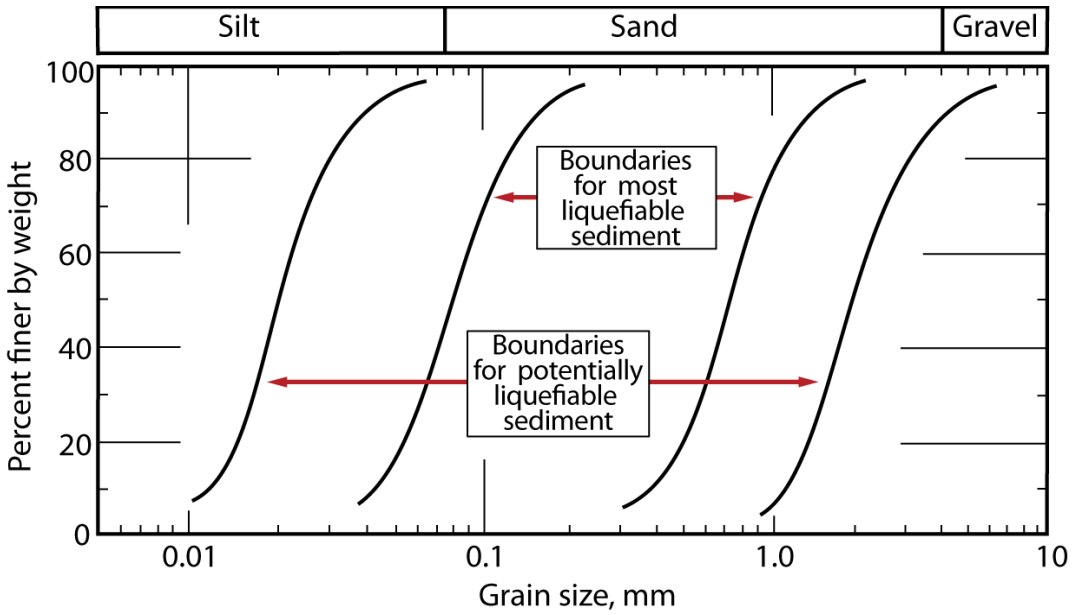


B.

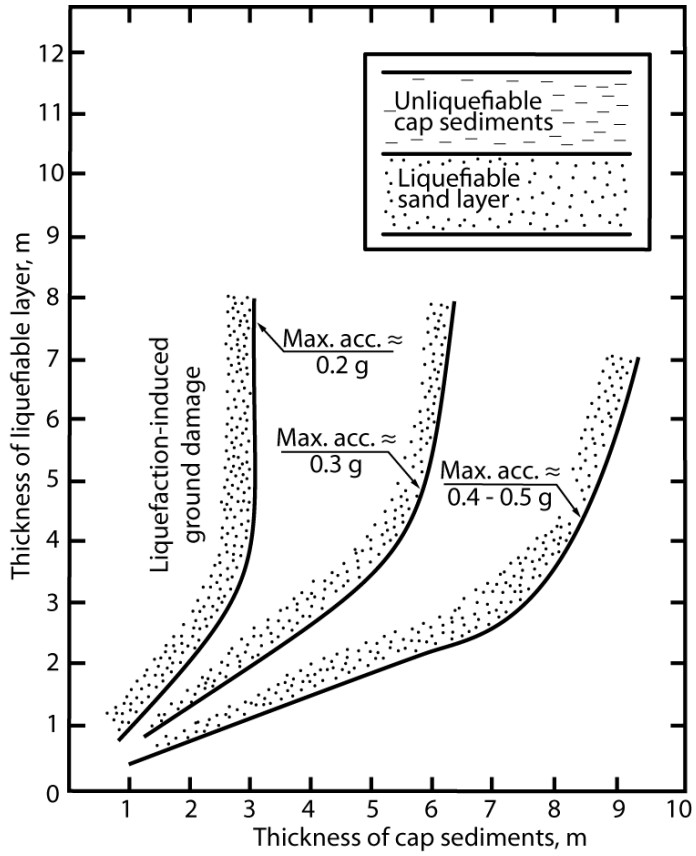


**Figure 1-3.** (A) Grain-size ranges for most liquefiable and readily liquefiable soils. (From Tsuchida and Hayashi, 1971.) (B) Relations between cap layer thickness and liquefiable layer thickness for three different ground accelerations relative to the acceleration of gravity (g=9.8 m/s$^2$). (From Ishihara, 1985.)

the porosity of sediments over time (Obermeier, 2009).

Certain aspects of potentially liquefied sediments are used in the field to distinguish between seismically induced liquefaction and aseismic features with similar appearance. Liquefaction will destroy any original bedding or fabrics, because the upward hydraulic force rotates bedding-parallel elongate grains to an angle highly oblique to bedding (Obermeier, 2009). More than one type of liquefaction feature should be found in multiple locations within a few km of each other in a regional study (Obermeier, 2009). There should also be evidence that liquefaction events are limited to discrete events in time, rather than continuously occurring (Obermeier, 2009). The age of liquefied sediments can be determined by radiocarbon dating (e.g., Guccione, 2005), optically stimulated luminescence (OSL) dating (e.g., Hatcher et al., 2012), cosmogenic nuclide dating (e.g., Gosse and Phillips, 2001), degree of soil development (e.g., Kelson et al., 1996), dendrochronology (e.g., Jacoby, 1997), and palynology (e.g., Lienkaemper et al., 2002). Finally, these events should occur in areas where water table depth is shallow, such as on floodplains.

## Earthquake Magnitude Estimation from Paleoseismic Data

Many paleosesimic investigations describe coseismic deformation resulting from pre-human settlement earthquakes that usually have no associated magnitude, because the earthquakes were not felt or measured. As a result, it is necessary in estimating seismic hazard from paleoseismic data to relate the deformation from an earthquake to an estimated magnitude. In many cases (e.g., Gutierrez et al., 2009; Ortuno et al., 2012), the empirical relations presented by Wells and Coppersmith (1994) are used to make a reasonable estimate of magnitude. These

relations use a database of 421 well-documented earthquakes with known magnitudes and measured fault parameters to create empirical relations between measurable coseismic deformation and magnitude. Wells and Coppersmith (1994) have empirically related maximum and average displacement, surface rupture length, and rupture area to earthquake magnitude (Fig. 1-4).

Other workers have fine-tuned the application of magnitude estimation using Wells and Coppersmith's (1994) results to paleoseismic data. Hemphill-Haley and Weldon (1999) recognized that in paleoseismic investigations, the most-often measurable attribute used to estimate magnitude is fault displacement. Since many paleoseismic investigations are preformed by trenching, fault displacement is often the only directly measurable parameter available. Biasi and Weldon (2006) suggested that surface rupture length could be estimated by fitting multiple displacements along a fault to an ellipse, which would give an additional parameter with which to measure earthquake magnitude. Hemphill-Haley and Weldon (1999) showed the extent that displacement can vary along the length of a fault, and concluded that five to ten displacement measurements are required to accurately estimate magnitude empirically. Additional statistical parameters were applied to the relations set fourth by Wells and Coppersmith (1994) based on the number of displacements obtained to minimize effects from sample size variations (Hemphill-Haley and Weldon, 1999).

Hemphill-Haley and Weldon (1999) recognized many issues using surface rupture length to estimate magnitude: (1) surface rupture length may include a varied number of fault segments; (2) some segments may be multiply reactivated and others may only have one episode of displacement; and (3) the surface rupture may not be completely preserved. Carpenter et al.

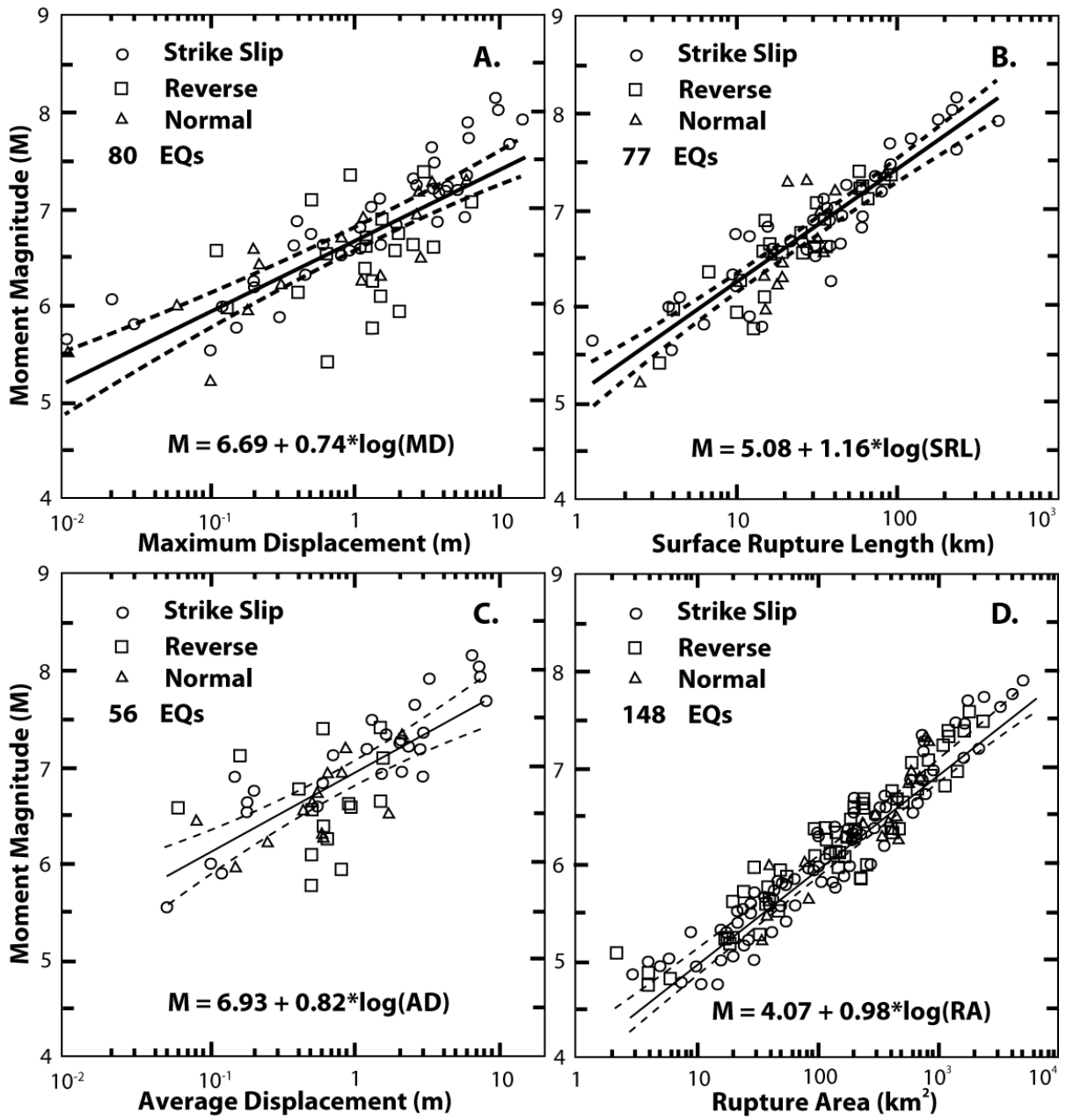


**Figure 1-4.** Empirically derived relationships between earthquake moment magnitude and (A) maximum displacement, (B) surface rupture length, (C) average displacement, and (D) rupture area. (From Wells and Coppersmith, 1994.)

(2012) further explored the discrepancies between magnitude estimates using surface rupture length versus fault segment length and found that using surface rupture length tends to underestimate the earthquake magnitude. Hemphill-Haley and Weldon (1999) also showed that displacement along a fault can vary greatly, and no one displacement should be used to estimate earthquake magnitude. The best solution is to use at least five measurements each of multiple fault parameters to estimate magnitudes. These studies by Hemphill-Haley and Weldon (1999), Biasi and Weldon (2006), and Carpenter et al. (2012) indicate that the work by Wells and Coppersmith (1994) is reliable enough to apply to paleoseismic environments. Efforts to satisfy these criteria were made in this project, although limited excavation sites prevented satisfactory application of the criteria. While the data collected for this thesis are limited in number, they do provide a measure of maximum recorded displacement along faults; it is possible that maximum displacement is larger in other locations that were not able to be measured.

## Intraplate Seismicity

Intraplate earthquakes are difficult to explain in the context of modern plate tectonics, because they do not occur along plate boundaries, but they do provide valuable insight into deformation occurring within plates. Intraplate seismicity occurs throughout the world. Examples of intraplate seismic zones include, but are not limited to: southwest Australia (e.g., Dentith et al., 2010), north China (e.g., Liu et al., 2011), and northeastern Brazil (e.g., Bezerra et al., 2011). A majority of paleoseismic work in the eastern United States has historically focused on the New Madrid, New England, and Charleston seismic zones (e.g., Ebel, 1984; Talwani and Cox, 1985; Kelson et al., 1996); however, the paleoseismic features found in the New Madrid

seismic zone are more abundant and thoroughly studied than those in the Charleston seismic zone, and will be the focus of the following case study. The systematic study of features in the New Madrid seismic zone provides a template with which paleoseismic investigations in other areas, such as the ETSZ, can be executed.

***Case study: The New Madrid seismic zone***

The New Madrid seismic zone is the most active seismic zone in the eastern United States and lies in the Mississippi River Valley in parts of Arkansas, Missouri, Kentucky, and Tennessee (Fig. 1-5). A series of four large earthquakes from December, 1811, to February, 1812, resulted in widespread liquefaction and surface deformation related to movement along one or more subsurface faults; magnitudes of three earthquakes have been estimated to be > 8 (Kelson et al., 1996), although Hough and Page (2011) recently suggested the maximum magnitude did not exceed $M_w$ = 7.0. Damage from these earthquakes has been extensively studied and has been an integral part of the development of paleoseismic technology to identify liquefaction features (Obermeier, 2009). Instrumentally recorded seismicity from the past 37 years in the New Madrid seismic zone has delineated a series of conjugate synthetic and antithetic faults that are favorably oriented in the present-day stress field, which may be related to reactivation of a deep-seated strike-slip basement fault system within the Cambrian Reelfoot rift (Fig. 1-5A) (Tavakoli et al., 2010). Recurrence interval estimates for M ≥ 7 earthquakes in the New Madrid seismic zone are 400–500 years (Johnston and Nava, 1985; Kelson et al., 1996). A paleoseismic study by Guccione (2005) found evidence for additional prehistoric earthquakes that support this recurrence interval.

Tavakoli et al. (2010) concluded that the faults in the New Madrid seismic zone fit a

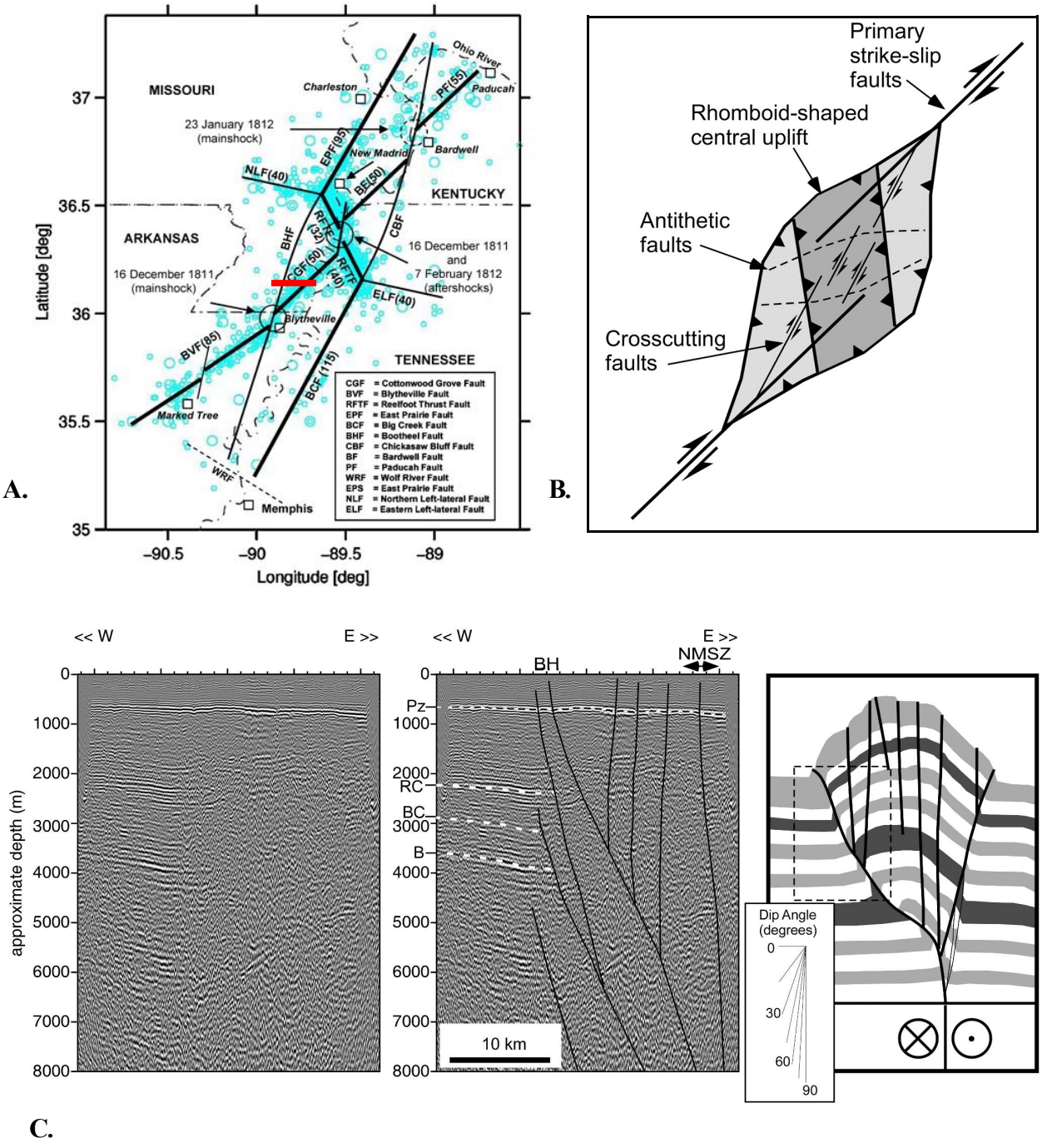


**Figure 1-5.** (A) Hypocenters and fault surface traces in the New Madrid seismic zone; locations of the four earthquakes between 1811 and 1812 are shown as black circles (from Tavakoli et al., 2010). Red line indicates the location of the seismic profile in C. (B) Model of a restraining stepover structure in a right-lateral fault derived from sandbox models (from Pratt, 2012). (C) Seismic reflection profile (left, uninterpreted; center, interpreted) from the New Madrid seismic zone (red line in A shows location); model of a flower structure to the right for comparison. Dashed box indicates a comparable portion of the model to the profile. Pz—Paleozoic rocks; RC—red clay unit; BC—basal clastic unit; B—basement rocks; BH—Bootheel lineament; NMSZ—New Madrid seismic zone. (from Pratt et al., 2012).

flower structure geometry, and that surface faults follow clay models of idealized right-lateral shear (Fig. 1-5B). Pratt et al. (2012) interpreted seismic reflection profiles of the Blytheville arch in the New Madrid seismic zone to show that the structure resembles a flower structure (Fig. 1-5C). Pratt (2012) compared the New Madrid seismic zone to an analog sandbox model of a restraining stepover structure along a right-lateral fault (Fig. 1-5B). These models, however, require that seismicity occur only on a subset of the faults in the original model (Tavakoli et al., 2010; Pratt, 2012; Pratt et al., 2012). Alternatively, Grollimund and Zoback (2001) attributed reactivation of the New Madrid seismic zone to isostatic rebound following deglaciation. The nature of the New Madrid and other intraplate seismic zones in North America remain uncertain.

## Previous Work in the East Tennessee Seismic Zone

Relatively little was known about the capabilities and origins of seismicity in the ETSZ until the NRC-sponsored pilot study began in 2008. Lack of large historic earthquakes, coupled with limited documented paleoliquefaction features, has necessitated development of new methods for paleoseismic research in the ETSZ. Despite the limited amount of work done to date in the ETSZ compared with other seismic zones, it is still a vital area for study, because it contains large population centers (e.g., Chattanooga and Knoxville, Tennessee) as well as numerous hydroelectric and nuclear power plants (e.g., Douglas Dam and Watts Bar Nuclear Plant), and other large engineered structures (e.g., bridges along Interstates 40 and 75) (Powell et al., 1994).

The spatial distribution of earthquakes in the ETSZ lies in a N30°E-trending cluster that stretches from northeastern Alabama to just east of Knoxville, Tennessee. A contoured map of

earthquake density delineates this trend, as well as two smaller splays of earthquakes that merge to the northeast with the main band (Fig. 1-1B). Determined focal mechanisms in the ETSZ are strike-slip, with dominant orientations of N95°E (left-lateral) and N50°E (right-lateral) (Chapman et al., 1997). Chapman et al. (1997) suggested that the epicenters delineate a series of northeast-striking en-echelon groups of faults and a series of east-striking groups of faults that dip 35°N and may be part of a conjugate fault system. Dunn and Chapman (2006) further analyzed three subsets of earthquake hypocenters and found a cluster of northwest-striking hypocenters with a nearly vertical dip near the Tennessee-North Carolina border in central East Tennessee. These focal mechanisms are compatible with the orientation of maximum principal stress in the ETSZ at N70°E, which is likely due to ridge-push forces from the Mid-Atlantic ridge (Zoback and Zoback, 1991).

Some workers (e.g., Powell et al., 1994; Steltenpohl et al., 2010; Powell and Chapman, 2012) attempted to correlate ETSZ earthquakes with the New York-Alabama (NY-AL) magnetic-gravity lineament of King and Zietz (1978). The NY-AL lineament is thought to represent the southeast margin of a major crustal boundary in the Grenville orogen that may have been reactivated as a sinistral (King and Zietz, 1978; Bartholomew and Hatcher, 2010) or dextral (Steltenpohl et al., 2010) strike-slip fault. Several differences between the orientation of the NY-AL lineament and the loci of ETSZ earthquakes make the connection more difficult (Hatcher et al., 2012). Most notable is the difference in the trends of the two features: the NY-AL lineament trends N40°E, which is notably different from the N30°E trend of the ETSZ (Fig. 1-1B). The greater extent of the NY-AL lineament also poses a problem. If the NY-AL lineament represents a fault that has been reactivated, then why is the whole lineament not seismically active (Hatcher

et al., 2012)? The contrast in trend between the NY-AL lineament and the focal mechanisms of the earthquakes also poses a problem (Chapman et al., 1997). Bartholomew and Van Arsdale (2012) attributed East Tennessee seismicity to a series of Neoproterozoic fracture sets oriented N20-30°E and Mesozoic fracture sets oriented N80-110°E, although no evidence is provided that these fractures exist in the ETSZ. Orientations of bedrock fractures measured in the Valley and Ridge and the Blue Ridge Foothills do not necessarily match these orientations: the dominant orientations measured are N70-90°E, N40-60°E, N10°E to N10°W, N20-30°W, and N50-70°W (Hatcher et al., 2012, their Fig. 12); fractures oriented N20-30°E are not common in the sets measured.

***Results from an 18-month pilot study***

Hatcher et al. (2012) conducted an extensive field reconnaissance throughout the ETSZ in an 18-month pilot study (funded by the Nuclear Regulatory Commission) that described possible seismogenic features including: thrust, normal, and strike-slip faults; a fissure cut by faults; anomalous bleached-clay fractures that have also been faulted; paleoliquefaction; shale "boils"; and disturbed sediments. The majority of their published work focused on field sites along the banks of Douglas Reservoir, which is also the location of field sites presented in the second chapter of this paper. This paper builds on some of the features from the pilot study, so it is best to summarize the pilot study results here to separate them from research for this thesis and that completed by Hatcher et al. (2012).

Abundant bleached fractures in Quaternary sediments were identified and mapped by Hatcher et al. (2012) at sites DL-3, DL-4, and DL-5. These bleached fractures appear tan against the red-brown alluvium due to groundwater-induced leaching of iron from clay minerals along

these fractures (Vepraskas, 1994). The DL-4 site contains abundant fracturing of $T_3$, $T_4$, or older terrace alluvium, some which overprinted earlier fractures (Fig. 1-6); these fractures are truncated by a contact with overlying colluvium that has an OSL age of >73.4 ka. A map of fractures in Quaternary "bedrock" was made for the area (Hatcher et al., 2012, their Fig. 8). At site DL-5 a second, larger map of Quaternary bedrock in $T_3$ or $T_4$ alluvium revealed a sinistral fault that offsets a series of bleached fractures ~25 cm (Fig. 1-7). Analysis of fracture orientations from these two sites reveals that fracture orientations are site-specific and there are fracture orientations that are not present in the underlying Paleozoic bedrock. Features described as "boils" of weathered shale chips were identified at this site (green areas in Fig. 1-7; Fig. 2-3), and are crosscut by later red clay-filled fractures. Excavation at site DL-3 revealed an ~80 cm-long fracture in undisturbed terrace material that was filled with the same weathered shale chips carried upward by liquefied sediments. The characteristics of this fracture provide a possible mechanism that emplaced the shale chips at site DL-5. In a pit in a $T_3$ terrace at site DL-5 are tilted Quaternary sediments that have been offset ~25 cm dip-slip by a NW-trending fault. An OSL date of these sediments indicates that they are 203 ± 13 ka. Downstream near Douglas Dam, reconnaissance of some $T_2$ or $T_3$ terraces revealed an abundance of fractures and a small fault (Hatcher et al., 2012).

Further upstream at site DL-1, paleoliquefaction features occur in $T_2$ alluvium. A clastic dike that is at least 1 m in plan view cuts upwards through at least 1 m of a sand-rich host material. Additional smaller "dikelets" are described as having associated microfaults, sills, and rip-up clasts (Fig. 1-8).

Site DL-6 revealed the largest variety of paleoseismic features during the pilot study. A


**Figure 1-6.** Three generations of fractures exposed at site DL-4. The numbers indicate the relative chronology of fractures, with 1 the oldest and 3 the youngest. The scale is 30 cm long. (From Hatcher et al., 2012.)

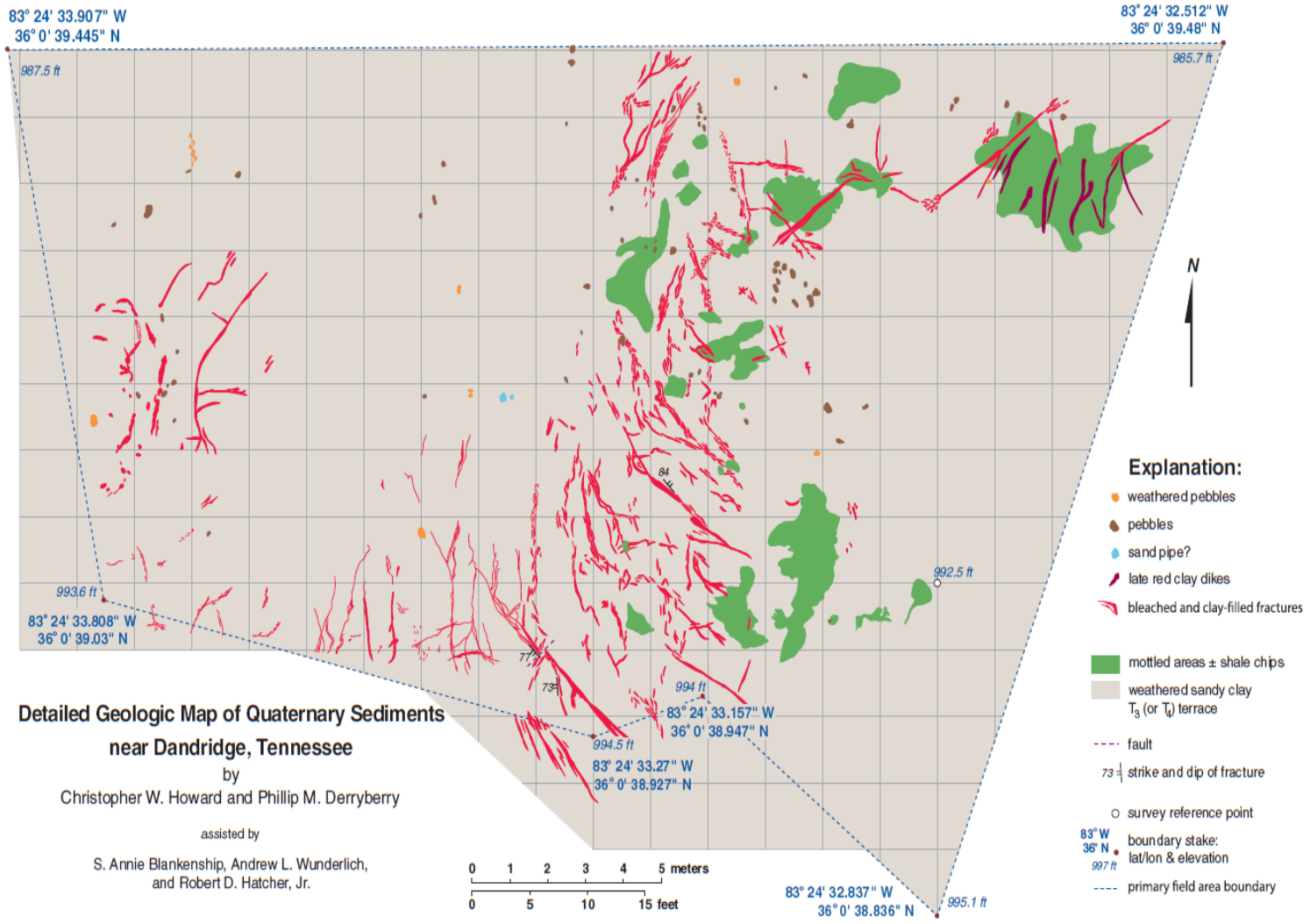


**Figure 1-7.** Detailed geologic map of site DL-5 east of the Tennessee Highway 92 bridge at Dandridge, Tennessee. Fractures appear systematic, and some cut the shale boils (green areas). (From Hatcher et al., 2012.)

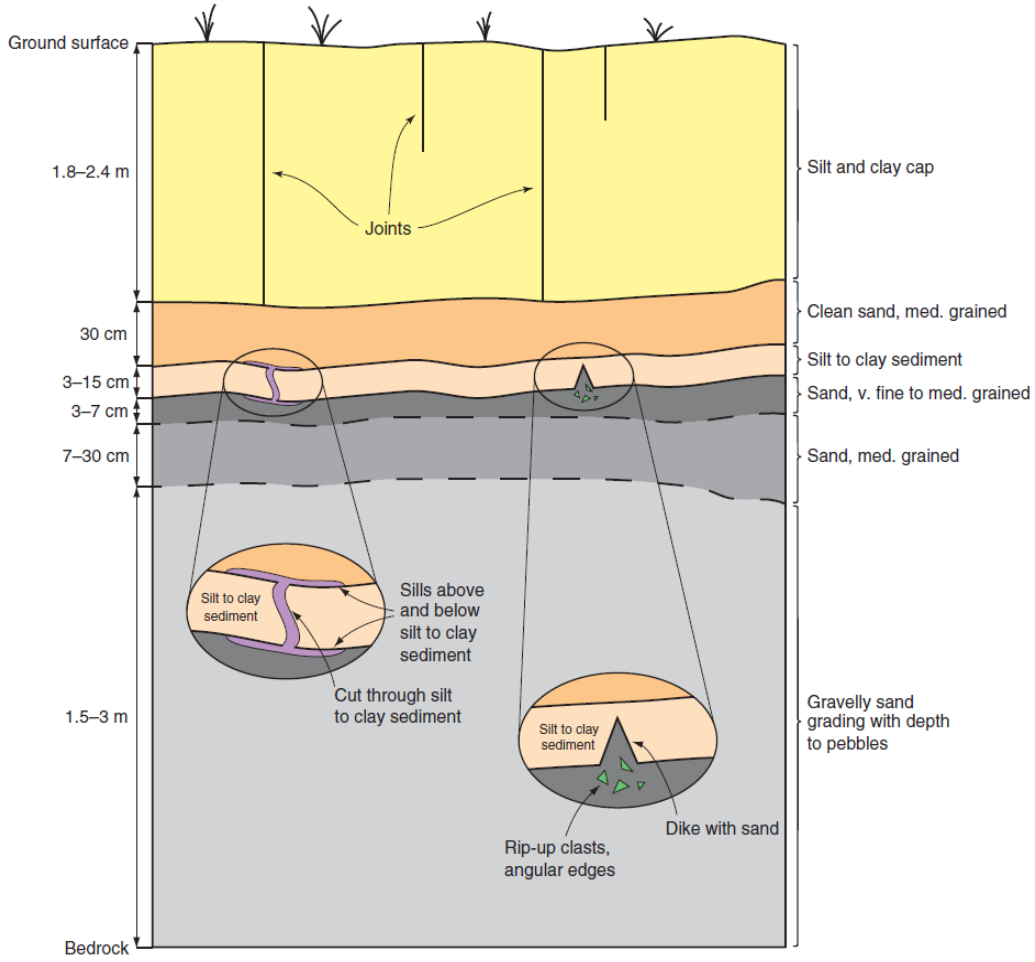


**Figure 1-8.** Field relationships of liquefied sediments exposed in $T_3$ terrace at site DL-1. (From Hatcher et al., 2012.)

more complete discussion of the location, bedrock, and stratigraphy of site DL-6 can be found in Chapter 2 of this thesis, as additional work at this site makes up a large part of that section. The main features at Hatcher et al. (2012) site DL-6 include: (1) a 15 m-long fissure filled with Quaternary sediments; (2) three thrust faults and one strike-slip fault with 10 cm to 1 m of offset; and (3) a boat-shaped fluidization structure that provides evidence for 2-3 paleoseismic events.

The 15 m-long fissure trends N33°E and has a nearly vertical dip (Fig. 1-9). It is filled with sandy to gravelly to cobbly $T_2$ or $T_3$ alluvium. The southern extension of the fissure is truncated by a thrust fault that strikes N38°E (Fig. 2-9). Approximately 6 m from the southern truncation, the fissure is cut by a small strike-slip fault with 10 cm of offset. One major branch occurs along this fissure approximately 3 m northeast of the strike-slip fault. The northern extension of the fissure continues for an unknown distance below recent alluvium. Trenching across the fissure in April, 2012, revealed that the base of the fissure is truncated by a thrust fault with 1 m of displacement. This thrust fault strikes N55°E and has a listric geometry that places Sevier Shale saprolite in the hanging wall above Quaternary sediments in the footwall, with splays into both (Fig. 1-9). Oblique slip on this fault bears N70-80°W. This fault is not likely related to mass wasting, because the hanging wall moved uphill, away from the river channel.

Several sets of curving, elongate fractures were identified in Quaternary sediments just above the northern extension of the fissure. These fractures bound a fluidization crater that has a boat-shaped geometry in cross section (Fig. 1-10). This boat-shaped structure truncates the original layering of nearby Quaternary sediments; OSL dating of unfluidized and fluidized sediments indicates that these sediments are >103 ka and >112 ka, respectively (Fig. 1-10), suggesting the boat-shaped structure is younger than 100 ka. Two fluidization events are

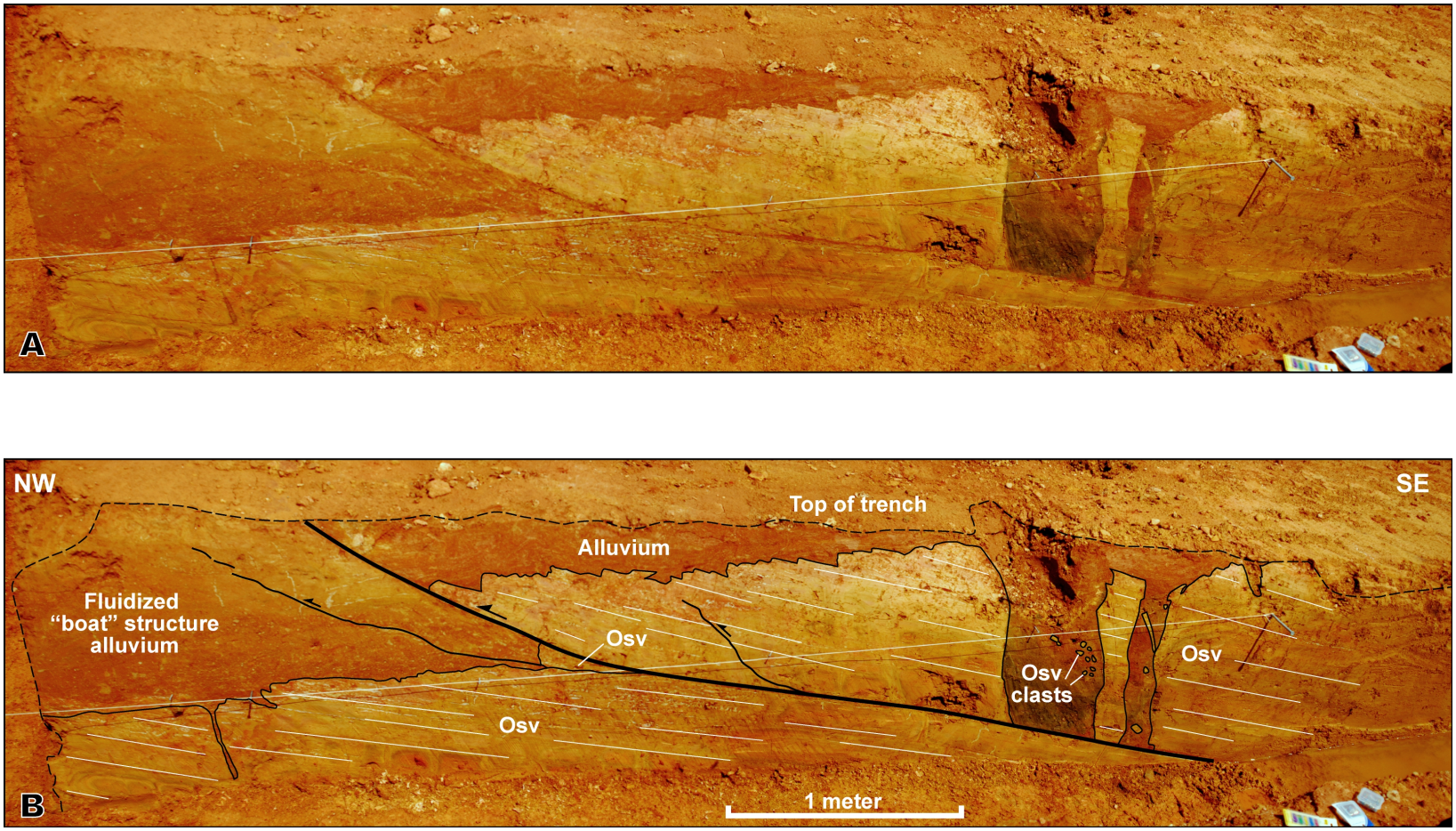


**Figure 1-9.** (A) Composite photograph of the April 2012 trench at Hatcher et al. (2012) site DL-6 that exposes the N55°E listric thrust fault that truncates the N33°E fissure. The fault has ~1 m upslope displacement. (B) Sketch overlay of the same photo, also identifying two faults splaying from the main thrust. The location of the southern end of the boat-shaped structure is also identified. Osv – Sevier shale. (Figures from Hatcher et al., 2012.)

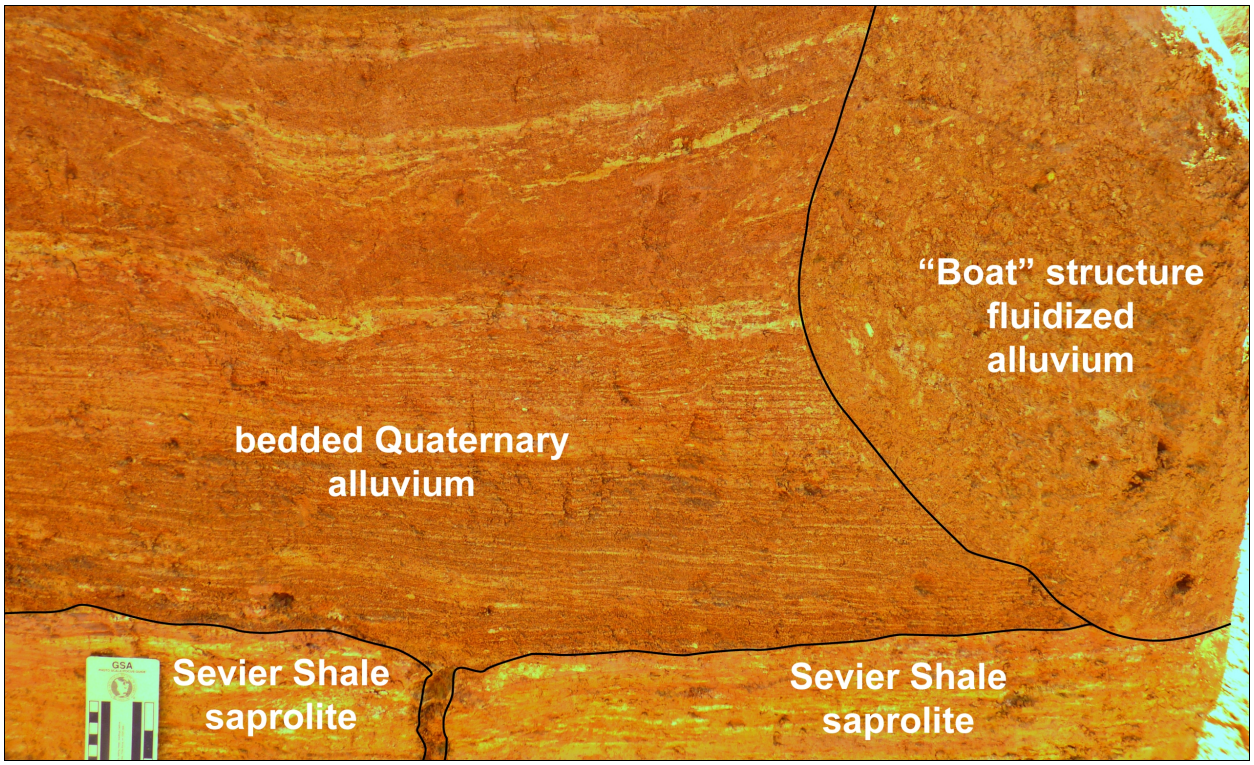


**Figure 1-10.** Trench wall exposing a partial cross section through the boat-shaped structure at site DL-6. The finely laminated Quaternary alluvium in the left of the photo is clearly truncated by fluidization in the boat-shaped structure.

recognizable within the structure that exhibit crosscutting relationships; these two events occurred >112 to >103 ka and are poorly constrained. The top 20 to 30 cm of the boat-shaped structure has developed a Bt or BCt soil horizon that indicates several to a few tens of thousands of years of weathering, which was later fractured, indicating a possible third event since 100 ka. Below the boat-shaped structure, there is a small thrust fault with ~10 cm offset placing Sevier Shale saprolite above fluidized alluvium and appears to indicate expulsion of groundwater along the fault during the event (Fig. 1-11).

Hatcher et al. (2012) concluded that collectively these data provide excellent support for the capability of the ETSZ to produce a large earthquake. Using the empirical relationship provided by Wells and Coppersmith (1994), the largest displacement found in the pilot study (1 m from the listric thrust fault in Fig. 1-9) relates to at least a magnitude 6.5 earthquake, which has the potential to significantly alter seismic risk in East Tennessee.

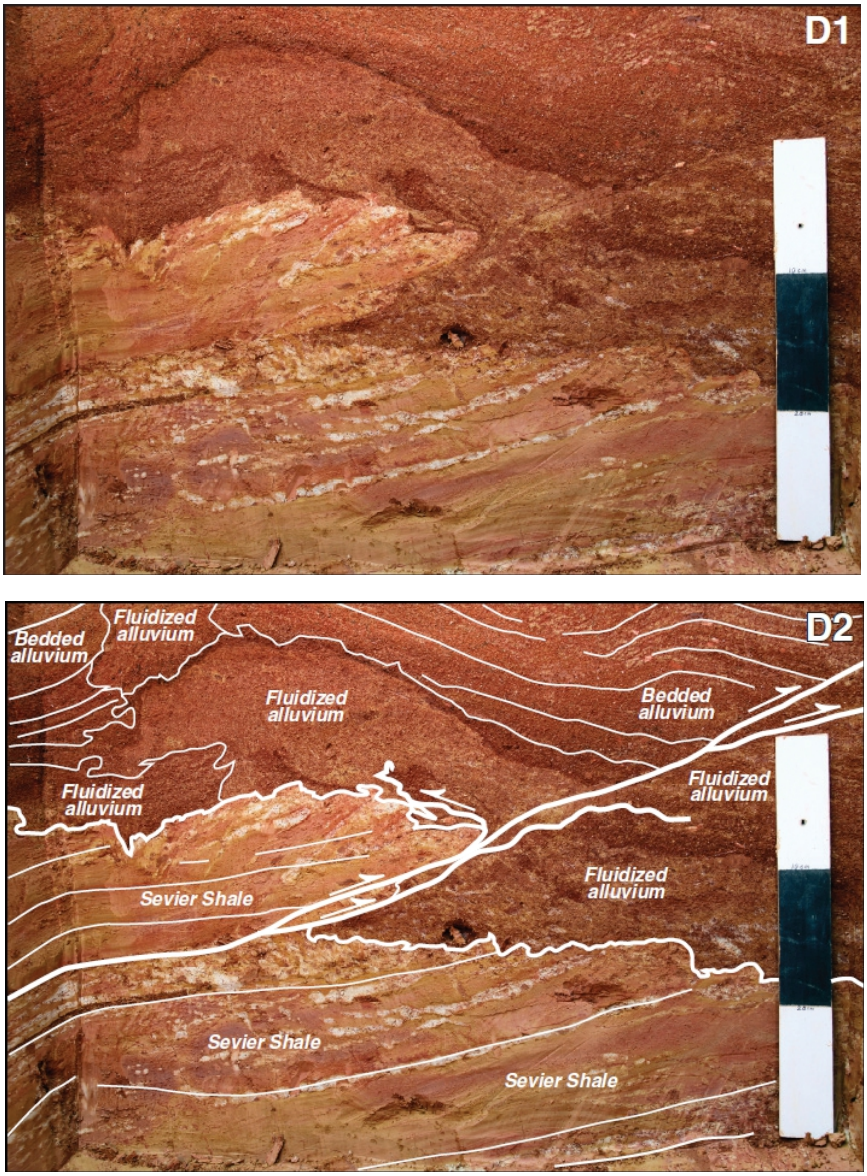


**Figure 1-11.** (D1) Thrust fault exposed in the trench below the boat-shaped structure with ~10 cm of offset at Hatcher et al. (2012) site DL-6. The Quaternary sand was fluidized in an event prior to the faulting, indicating that at least two events have affected this area. The scale is 30 cm long. (D2) is an annotated version of the same photo. (Figures from Hatcher et al., 2012.)

# *CHAPTER II*

# *PALEOSEISMIC EVIDENCE NEAR DANDRIDGE, TENNESSEE*

## Study Area

Douglas Reservoir near Dandridge, Tennessee, provides a unique area in which to study paleoseismic features. In 1943 the Tennessee Valley Authority (TVA) flooded a 65 km (40 mile)-portion of the French Broad River by building a hydroelectric dam that created Douglas Reservoir (Tennessee Valley Authority, 2012). The TVA seasonally varies the water level of the lake some 15 m to provide protection against flooding; as a result, large areas of the lake bed are exposed from late October until mid-April. The exposed lake bed includes multiple Quaternary French Broad River terraces, which overlie shale and limestone bedrock outcrops. Lack of vegetation on the exposed banks permits very high-quality reconnaissance and detailed geologic mapping of possible paleoseismic features that occur in bedrock and overlying Quaternary sediments.

The French Broad River along Douglas Reservoir meanders through a valley underlain primarily by Middle Ordovician Sevier Shale; the contact with underlying Knox Group carbonates is exposed on both sides of the river (Hardeman et al., 1966; Hatcher and Bridge, 1973). The Knox Group dominates the ~4 km-wide, northeast-trending belt immediately northwest of the reservoir (Hardeman et al., 1966). Karst is common in the Knox and lower Middle Ordovician carbonate rocks, so paleoseismic investigations must occur southeast of this region in areas underlain by Sevier Shale to eliminate the possibility of sinkhole collapse features mimicking paleoseismic features. Sevier Shale is a fissile, dark gray, calcareous shale that

weathers yellowish brown, with 5 cm-thick layers of shaly limestone that increase in frequency near the Lenoir Limestone contact (Hatcher and Bridge, 1973). Sevier Shale also has sufficiently high fracture porosity and permeability that allows it to serve as an aquifer (Hatcher et al., 2012).

At least five distinct terraces have been identified along the banks of Douglas Reservoir; these terraces descend "step-like" to the modern channel of the French Broad River (Hatcher et al., 2012). The modern floodplain ($T_0$) prior to the construction of Douglas Dam is the lowest terrace and is only partly exposed in the upstream limits of Douglas Reservoir during maximum drawdown. Older, higher terraces are better exposed during winter drawdown, and are the focus of this chapter. A $T_2$ or $T_3$ terrace exposed at site DL-5 yielded an OSL age of 203 ± 13 ka (Hatcher et al., 2012). Radiocarbon dating of similar terraces along the Little Tennessee River in central East Tennessee has revealed an age of 27,595 ± 980 y on a $T_2$ terrace (Mills and Delcourt, 1991), which corresponds well with the radiocarbon ages 32,330 ± 4,140 y and 31,230 ± 1,930 y of $T_2$ terraces at the Watts Bar Nuclear Plant along the Tennessee River (Chapman, 1977). Chapman (1977) assigned an age of 10 to 12 ka to $T_1$ terraces in the Little Tennessee River valley. The ages of French Broad River terraces are poorly constrained, and OSL ages obtained from the terraces only provide a maximum age for the deformation in a terrace.

***Site DL-5 (36.01025° N, 83.40790° W)***

Site DL-5 is located just east of the Tennessee Highway 92 bridge on the southern bank of the reservoir, less than 1 km from Dandridge, Tennessee (Fig. 2-1A). The site is located on the inside of a meander of the French Broad River, where an extensive series of terraces is developed (Fig. 2-1B). Site DL-5 is located on a $T_3$ or $T_4$ terrace exposure. This site is underlain by Knox Group carbonates and Sevier Shale (Hatcher and Bridge, 1973; Hatcher, R.D., Jr., 2013,

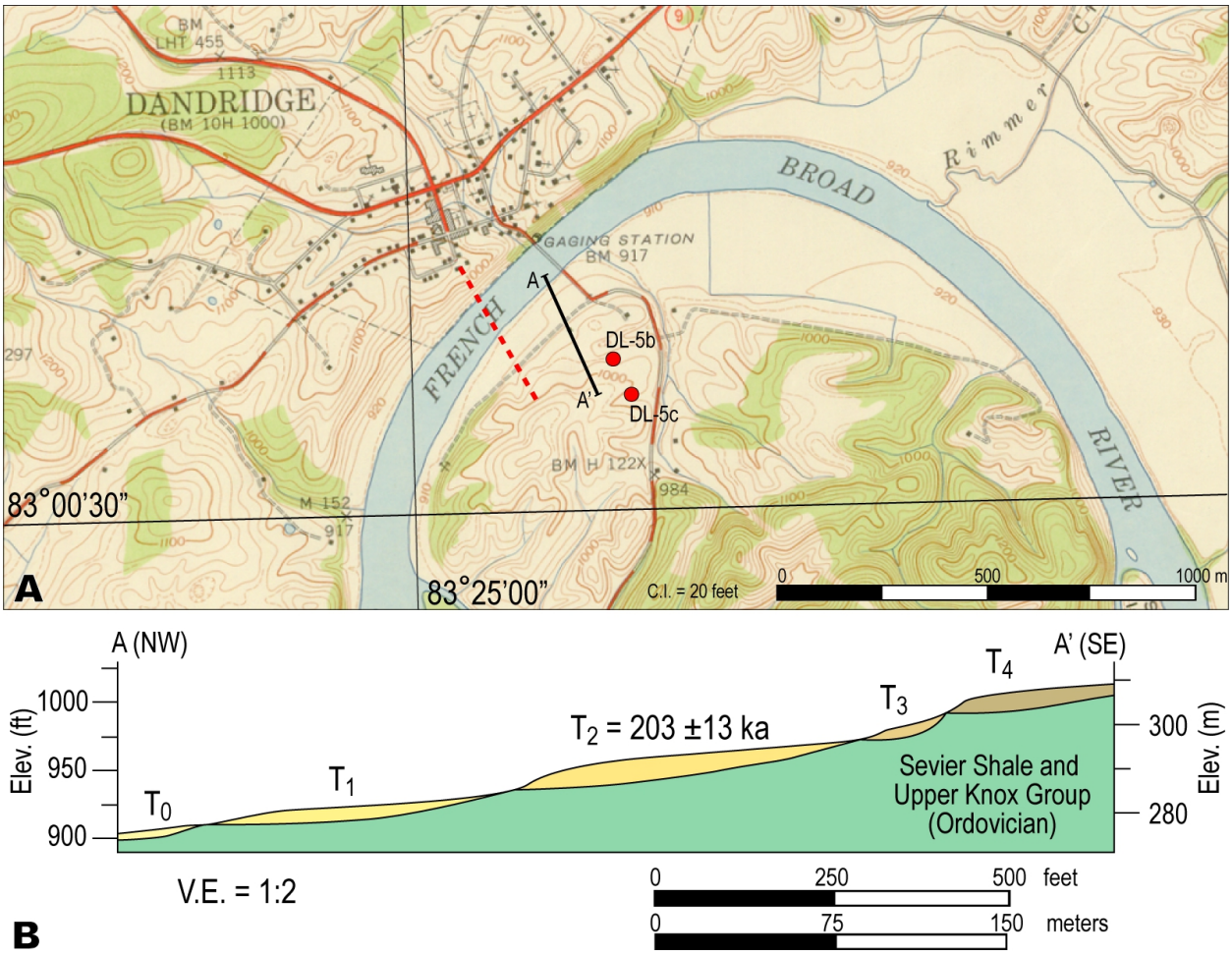


**Figure 2-1.** (A) Part of the Jefferson City 7.5 minute quadrangle, Tennessee (1939 version), showing the locations of the cross section in B and sites DL-5b and DL-5c. Dashed red line indicates the location of the current Tennessee Highway 92 bridge. C.I.—contour interval. (B) Cross section showing relative positions and ages of stream terraces along the French Broad River. The OSL age of the $T_2$ (?) terrace here is also shown. V.E.—vertical exaggeration.

personal commun.), so there is a possibility that some features could be related to karst collapse.

At site DL-5, there are two locations for which this chapter provides additional data: DL-5b and DL-5c (Fig. 2-1A). DL-5b is located on the banks of the French Broad River, ~300 m from the modern channel; DL-5c is located along a small tributary of the French Broad River, which flowed ~500 m north from the site to its confluence with the modern French Broad River. Site DL-5b is subjected to large amounts of erosion and deposition by flow in the reservoir. A pit dug in this area in 2010 had been completely filled during the seven months it was inundated. Movement of large cobbles and boulders is common at site DL-5b. The same is not true for site DL-5c; flow of the reservoir does not deposit large particles here. This site is near an area that has been recently excavated for recreational purposes, which has provided additional exposures of Quaternary sediments and bedrock.

***Site DL-6 (35.97350° N, 83.44115° W)***

Site DL-6 is located on the inside of a meander of the modern French Broad River ~5 km southwest of Dandridge, Tennessee (Fig. 2-2). Sevier Shale underlies this site with an orientation of ~N70°E, 15°SE, and the contact with the overlying Lenoir Limestone is ~1.9 km northwest of the site. At the contact, the rocks dip steeply to the south, and the dip gradually shallows to 15°SE at site DL-6. A 15° dip places the top of the underlying carbonate units ~500 m below the surface, which is well below the minimum 200 m limit for karst solution openings suggested by Fetter (2001).

A series of terraces unconformably overlie the Sevier Shale (Fig. 2-2C). Site DL-6 is a south-facing exposure of $T_3$ (?) terrace and Sevier Shale along a small tributary stream of the French Broad River, which flowed ~1 km SW to its confluence with the modern channel (Fig. 2-

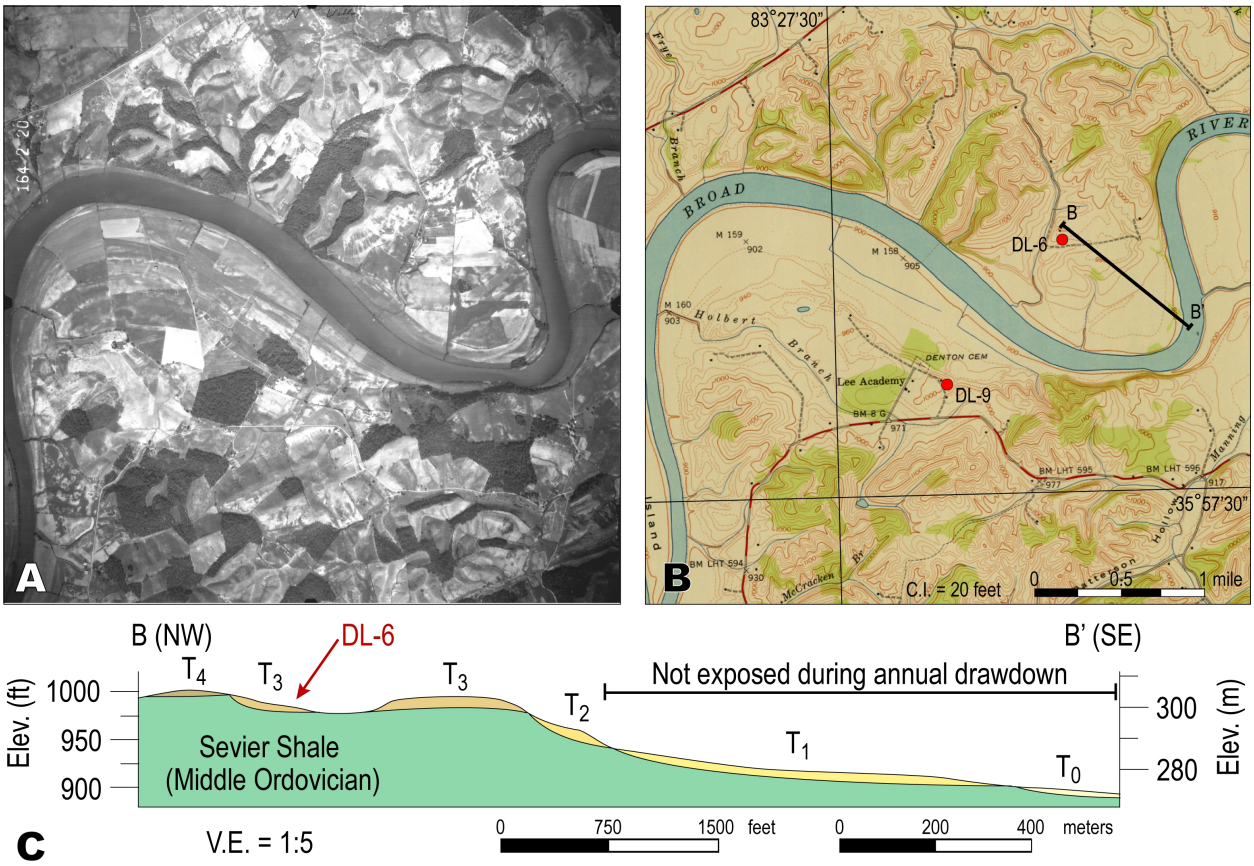


**Figure 2-2.** (A) 1938 Tennessee Valley Authority aerial photo of site DL-6 and the surrounding area. (B) Part of the Shady Grove 7.5 minute quadrangle, Tennessee (1939 version), showing the same area in A and locations of the cross section in C and sites DL-6 and DL-9. C.I.—contour interval. (C) Cross section showing relative positions and ages of stream terraces along the French Broad River near site DL-6. V.E.—vertical exaggeration.

2 A and B). Strong currents in the reservoir at this site have partially eroded the terrace material, leaving a layer of sediment 0-4.0 m-thick above the shale. The terrace material has been classified as silty clay loam to loam to clay loam to sandy loam, with a Munsell color range of 2.5 YR 4/6 to 4/8; a dark brown to reddish yellow BC or BCt soil horizon may be locally developed (Hatcher et al., 2012). The surface soil is a well-developed ultisol, which suggests that there has been ~100 ka of weathering (Hatcher et al., 2012). Some areas contain 0.5 m thick layers of pebbles, cobbles and boulders; elsewhere in the alluvium are stray pebbles composed mostly of rounded granitoid, quartzite, vein quartz, and rounded to angular chert, many of which have completely weathered to yellow, gray, green, red, or white sand.

## Additional Paleoseismic Evidence at Site DL-5

Much of the work at site DL-5 for this thesis supplemented that done by Hatcher et al. (2011) and Hatcher et al. (2012). The data presented here provide clarification of features at Site DL-5.

### *X-ray diffraction applied to shale "boils" at DL-5b*

Shale chips from the shale "boils" mapped by Hatcher et al. (2012) were analyzed using X-ray diffraction (Fig. 2-3). It is important to determine that the mineralogical makeup of the shale "boil" liquefaction fragments is in fact identical to the shale in the area and is not altered or reworked Quaternary sediment. Shale chips were collected from the site, dried, and powdered before analysis performed by the Rigaku Ultima IV unit at the University of Tennessee–Knoxville. The data from these shale chips were compared with diffraction data from fresh Sevier Shale, which was collected from a roadcut on Tennessee Highway 92 just south of the

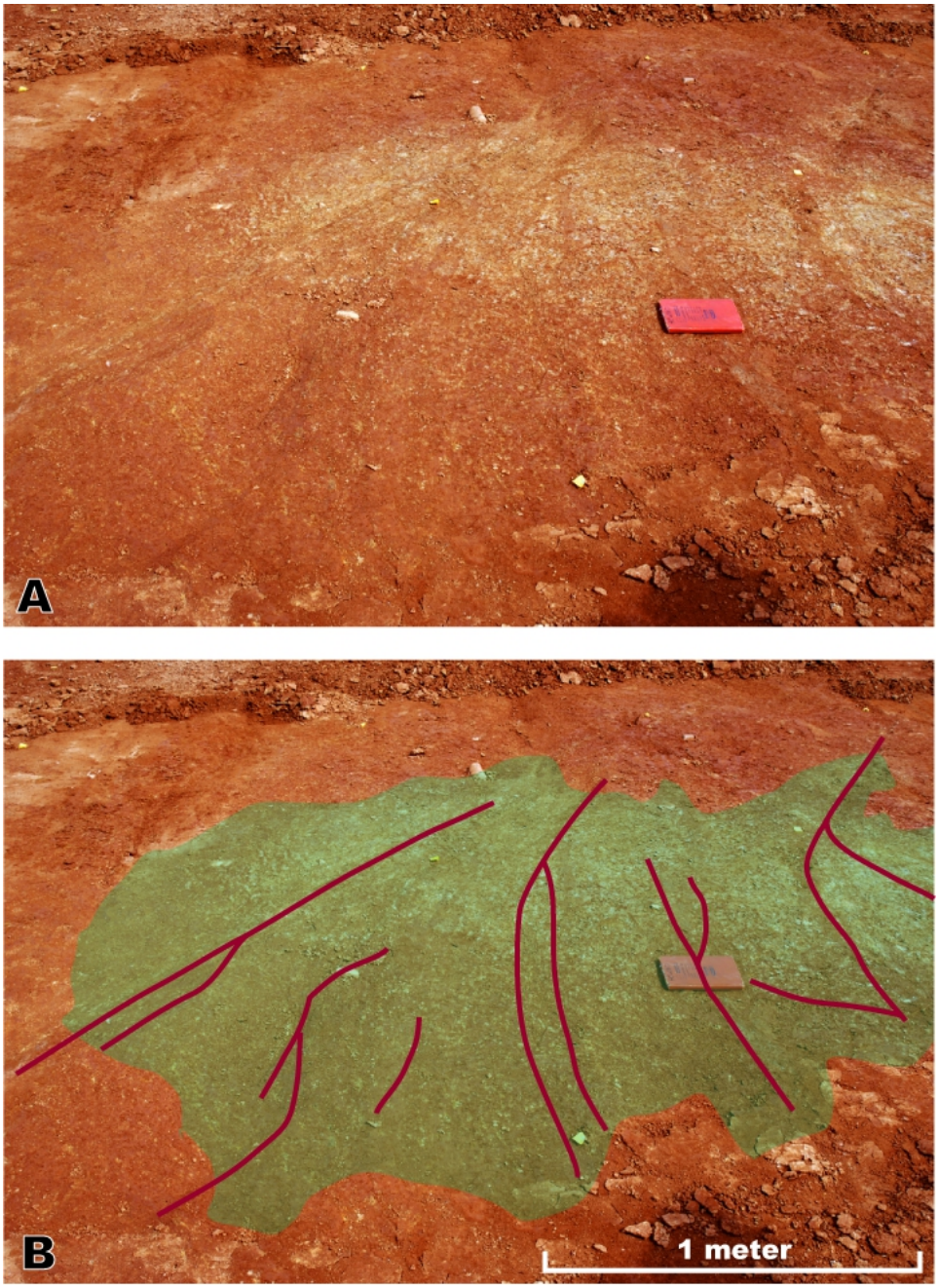


**Figure 2-3.** (A) Shale-clay boil exposed at site DL-5b during grading. This boil is located in the NE corner of Figure 1-7. Note the darker red fractures that cut the boil. (B) Sketch overlay showing the extent of the boil (green) and fractures that cut the boil (dark red). (Photos by R.D. Hatcher, Jr.)

site. The unweathered shale was powdered before analysis.

Data from the XRD analyses reveal that the shale chips are composed primarily of quartz, kaolinite-1A, and illite-$2M_2$ (Fig. 2-4A), and Sevier Shale is composed primarily of quartz, calcite, kaolinite-1A, and illite-$2M_2$ (Fig. 2-4B). The lack of calcite in the shale chips is likely the result of dissolution prior to emplacement. The proportion of clay minerals is greater in the shale chips, likely due to removal of calcite or weathering of minor feldspar. Matching clay mineralogy of the shale chips and Sevier Shale suggests that the chips in the shale boils could have originated from underlying Sevier Shale.

***Trenching paleolandslide deposits at DL-5c***

An outcrop of Lenoir Limestone striking N49°E and dipping 24°SE at this site lies structurally above material that resembles highly fractured Sevier Shale saprolite (Fig. 2-5). Further interest in the site was generated by late Quaternary pebbles in the saprolite, which were hypothesized to be: (1) embedded in the shale; (2) resting on an exposed Quaternary erosional surface; or (3) embedded within a structurally disturbed mixture of terrace material and Sevier Shale saprolite (Hatcher et al., 2011).

Trenching across the saprolite-limestone contact may have resolved this issue. The trench, measuring 12 m by 1.5 m, was photographed and documented in detail. The east wall (Fig. 2-6) of the trench was the only wall that contained significant exposure of Lenoir Limestone. The material that appeared to resemble fractured Sevier Shale saprolite was revealed to be layered terrace alluvium and Sevier Shale. The alluvium contains multiple thrust faults and one normal fault with small offsets on the order of 5 cm with associated alluvium folding, fault displacement verges downhill. The alluvium is interpreted to be a paleolandslide deposit that

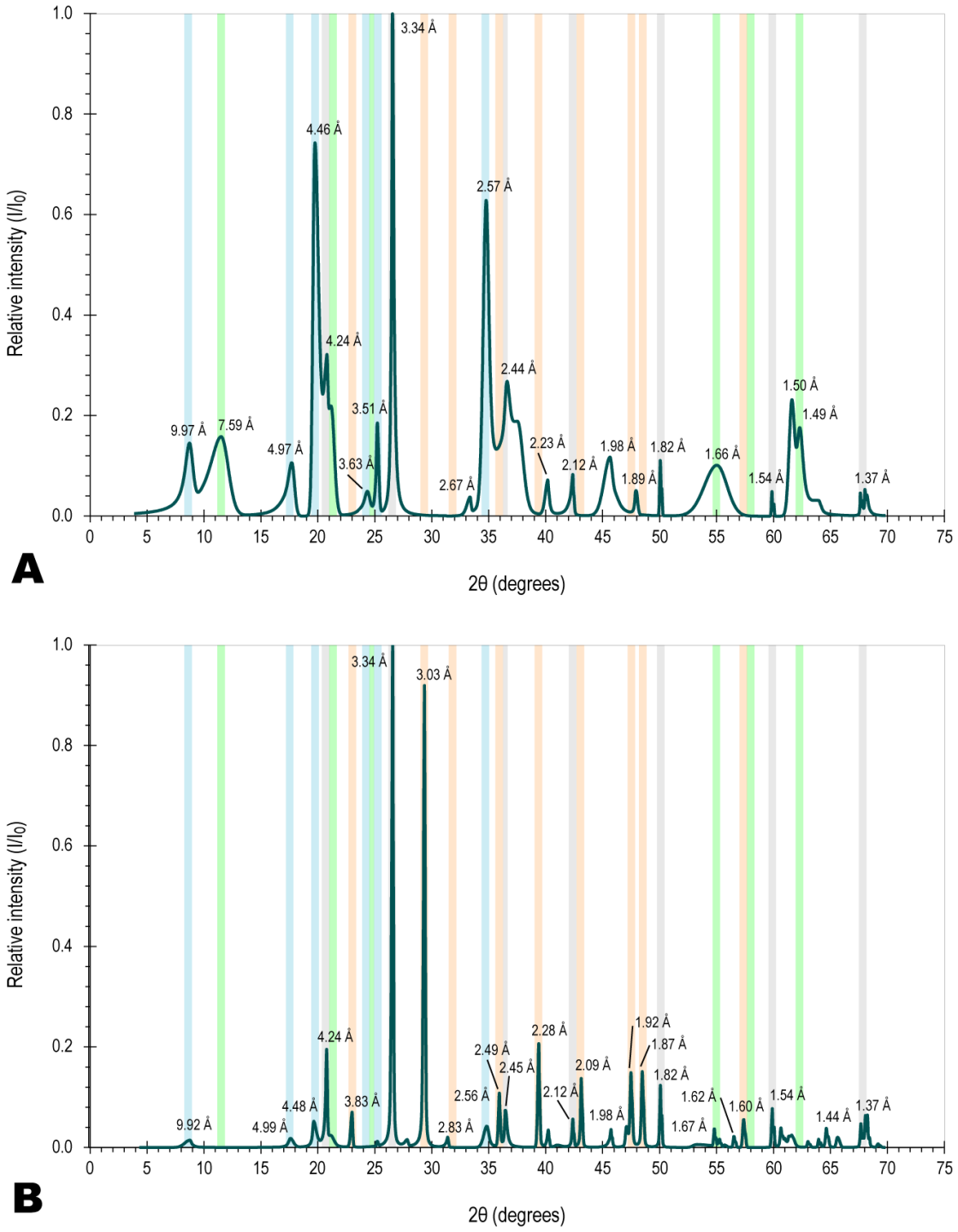


**Figure 2-4.** X-ray diffraction data derived from (A) shale "boil" chips and (B) Ordovician Sevier Shale. Gray bars—quartz peaks; blue bars—illite-2$M_2$ peaks; pink bars—calcite peaks; green bars—kaolinite-1A peaks. Note that the shale chips do not display any calcite peaks and that quartz, illite-2$M_2$, and some kaolinite-1A peaks persist in both samples, and that the proportion of clay minerals is greater in the shale chips.

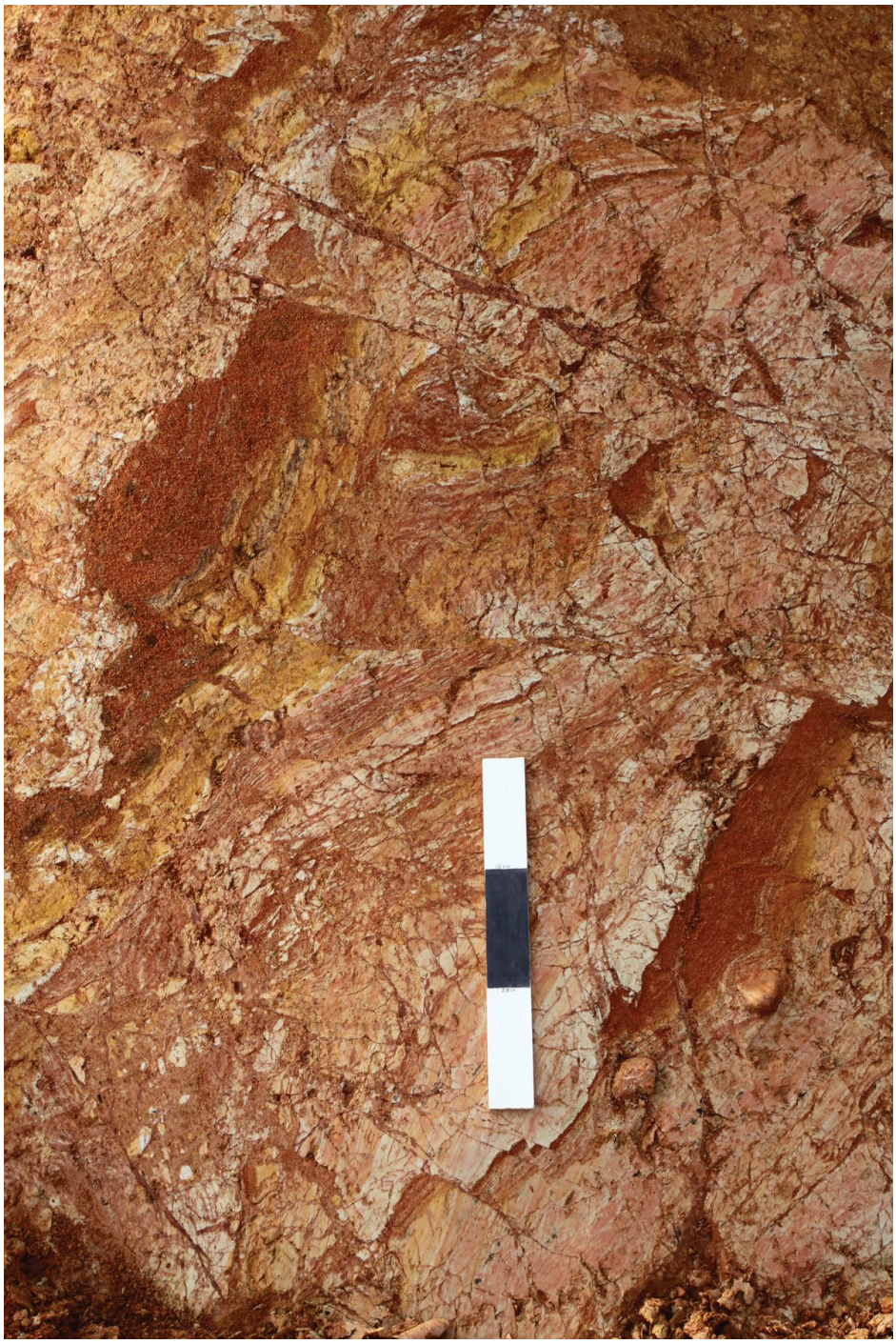

**Figure 2-5.** Pebbles embedded in mixed fractured Sevier Shale saprolite and terrace alluvium at site DL-5c. Numerous small faults cut the saprolite and alluvium. Scale is 30 cm. (Photo by J.D. Vaughn.)

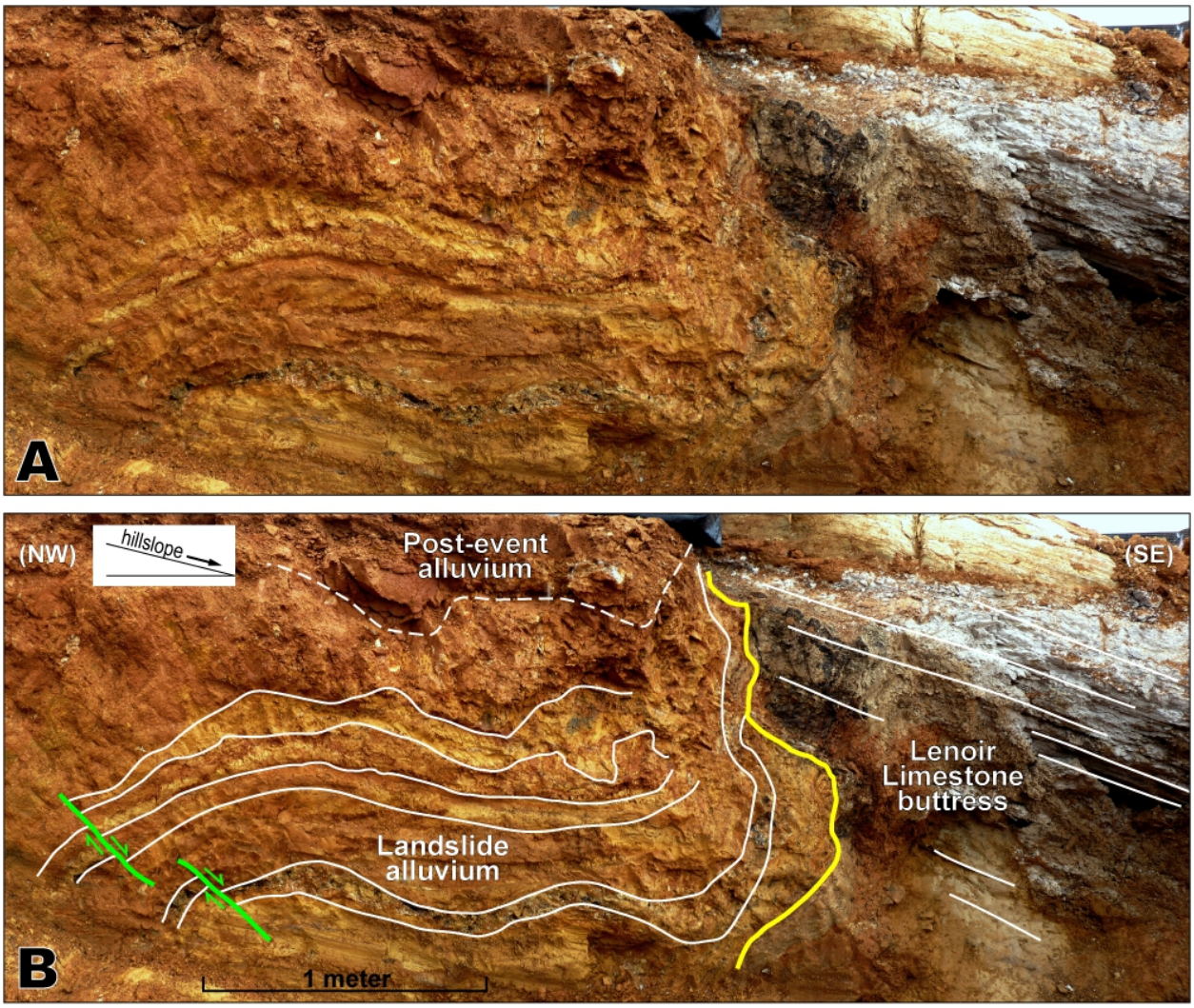


**Figure 2-6.** (A) Composite photo of a portion of the NE wall of the trench at DL-5c (location shown in Fig. 2-1A) featuring layered Quaternary alluvium landslide deposits buttressed against an outcrop of Lenoir Limestone. Small normal faults displace the layered alluvium. (B) Sketch overlay identifying the contact between alluvium and limestone (yellow), as well as two small normal faults (green). The hillslope gradient relative to the trench is also shown. White lines in limestone are bedding.

was buttressed at its toe against an exposure of Lenoir Limestone. While landslides can be triggered by seismic activity, there is no way to determine if this paleolandslide was produced by an earthquake or some other event, such as sinkhole collapse.

## Additional Paleoseismic Evidence at Site DL-6

The data collected at site DL-6 for this thesis both provide additional information on features previously described by Hatcher et al. (2012) and describe new features mapped in detail at this site.

### *Additional data delimiting branching fissure fill sediments*

Two OSL samples were collected from sediment filling the branching fissure (locations on Fig. 2-7) and one from the west wall of the April, 2012, trench at DL-6 in Hatcher et al. (2012) (Fig. 2-8). These samples were collected by hammering ~30 cm polyvinyl chloride (PVC) pipe into the sediment; the open end of the pipe was shielded from sunlight using a PVC cap and/or duct tape before each sample was collected. After collection, the open end of the pipe was sealed in the same manner as quickly as possible. The samples were processed by Dr. Steven L. Forman at the University of Illinois—Chicago Luminescence Dating Research Laboratory.

The data from these samples (Table 2-1) reveal that the sediments filling the branching fissure are much younger than the terraces at DL-6 sampled by Hatcher et al. (2012). The two samples collected along the surface trace of the fissure reveal OSL ages of 15,450 ± 1,745 y at DL-6-01 and 4,890 ± 700 y at DL-6-02. The difference in these two ages may be the result of an additional seismic event; it is also possible that over-land water flow from a large rain event

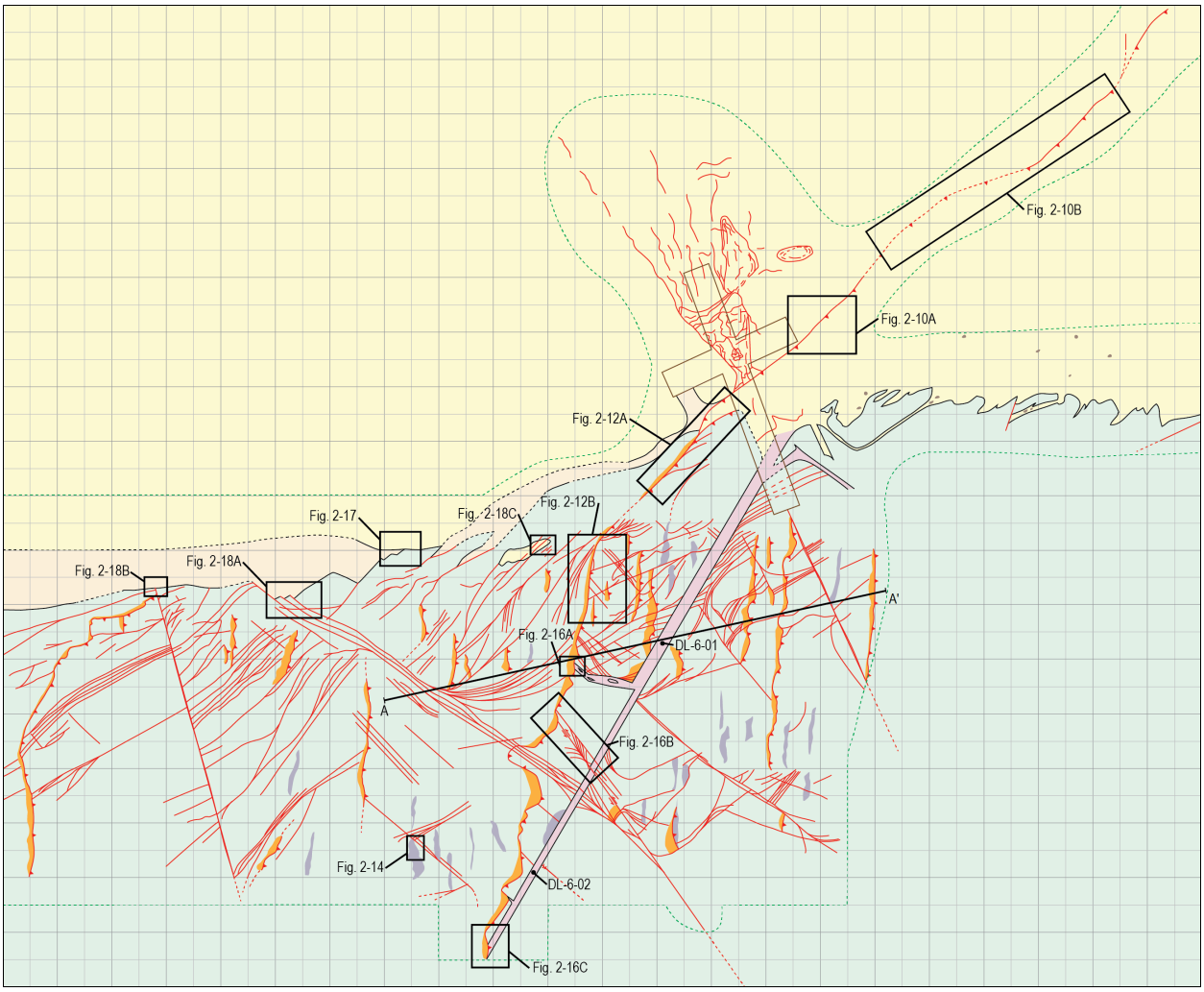


**Figure 2-7.** Map from Plate 1 and Figure 2-11 showing the locations of OSL samples DL-6-01 and DL-6-02, as well as locations of photos in Figures 2-10, 2-12, 2-14, 2-16, 2-17, and 2-18. Line A-A' denotes the line of cross section in Figure 4-3 and on Plate 1.

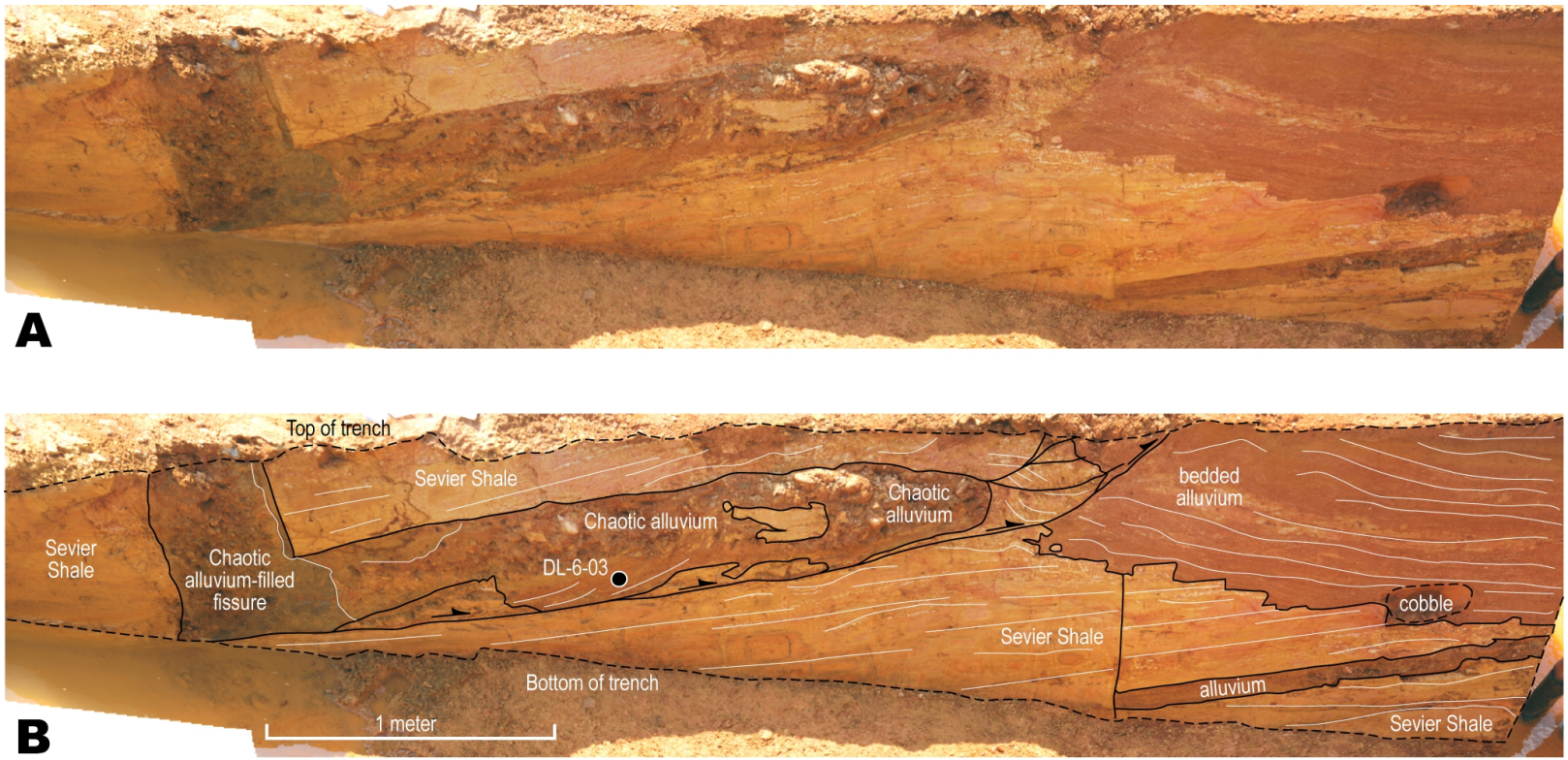


**Figure 2-8.** (A) Composite photo of the west side of the April 2012 trench at site DL-6 that exposes a faulted branch of the fissure. (B) Sketch overlay showing the location of OSL sample DL-6-03; (B) interpretation. (Composite photo by R.D. Hatcher, Jr.)

**Table 2-1.** Optically stimulated luminescence (OSL) ages and associated chronologic data for sediments filling the branching fissure at site DL-6.

| Field number[a] | Laboratory number [a] | Equivalent dose (Gray)[b] | Uranium (ppm)[c] | Thorium (ppm)[c] | $K_2O$ (%)[c] | $H_2O$ (%) | Cosmic dose (mGray/yr)[d] | Total dose rate (mGray/yr) | OSL age (yr)[e] |
|---|---|---|---|---|---|---|---|---|---|
| DL-6-01 | UIC3217 | 40.08 ± 4.01 | 3.4 ± 0.1 | 16.2 ± 0.1 | 0.61 ± 0.01 | 5 ± 2 | 0.12 ± 0.01 | 2.59 ± 0.13 | 15,450 ± 1745 |
| DL-6-02 | UIC3215 | 17.05 ± 2.25 | 4.5 ± 0.1 | 16.2 ± 0.1 | 0.61 ± 0.01 | 5 ± 2 | 0.12 ± 0.01 | 3.49 ± 0.21 | 4890 ± 700 |
| DL-6-03 | UIC3222 | 18.14 ± 1.95 | 1.5 ± 0.1 | 8.0 ± 0.1 | 0.56 ± 0.01 | 5 ± 2 | 0.12 ± 0.01 | 1.53 ± 0.08 | 11,880 ± 1420 |
| DL-9-01 | UIC3221 | 39.60 ± 3.83 | 2.8 ± 0.1 | 12.3 ± 0.1 | 0.97 ± 0.01 | 5 ± 2 | 0.12 ± 0.01 | 2.50 ± 0.13 | 15,865 ± 1735 |
| DL-9-02 | UIC3323 | 38.39 ± 1.36 | 2.0 ± 0.1 | 9.1 ± 0.1 | 0.70 ± 0.01 | 10 ± 3 | 0.14 ± 0.01 | 1.76 ± 0.09 | 21,765 ± 1445 |

[a] Analyses were performed by Steven L. Forman, Luminescence Dating Research Laboratory, Department of Earth and Environmental Science, University of Illinois—Chicago, Chicago, Illinois 60607-7059, USA.

[b] Equivalent dose analyzed under blue-light excitation (470 ± 20 nm) by single aliquot regeneration protocols (Murray and Wintle, 2003). The coarse-grained (150-250 μm) quartz fraction was analyzed.

[c] U, Th and $K_20$ content analyzed by inductively coupled plasma-mass spectrometry analyzed by Activation Laboratory LTD, Ontario, Canada.

[d] Cosmic dose rate component is from Prescott and Hutton (1994).

[e] Ages calculated using the minimum age model of Galbraith et al. (1999) because of high overdispersion values (>35%), which weights for the youngest equivalent dose population. All errors are 1σ, and ages were calculated from A.D. 2000.

could become channelized into the fissure and partially erode the sediment filling the fissure. The sediments from the fissure branch in the west wall of the April, 2012, trench (DL-6-03) revealed an OSL age of 11,880 ± 1,420 y, which is similar to the 15 ka age of sample DL-6-01. An additional sample (DL-9-01) obtained from sediment filling a similar branching fissure at site DL-9 by James D. Vaughn (location in Fig. 2-2) yielded an OSL age of 15,865 ± 1,735 y, which is younger than a nearby sample obtained from undisturbed terrace material (DL-9-02) by Randel T. Cox that yielded an OSL age of 21,765 ± 1,445 y. The age of sediment filling this fissure is very close to the age from sample DL-6-01; combining these two ages suggests that the fissures were filled 13,705–17,600 years ago. Faulting that truncates these fissures occurred since that time.

X-ray diffraction analysis of sediment from the DL-6-02 sample reveals few surprises concerning the makeup of the sediment filling the fissure: quartz, kaolinite-1A, and illite-$2M_1$ are the primary minerals (Fig. 2-9). These two clay minerals are common weathering products, resulting from hydration of silicate minerals, such as feldspars (Nesse, 2000).

***Fracture array and faults in Sevier Shale saprolite***

In April, 2012, while Douglas Reservoir was drawn down, the exposed terrace alluvium at site DL-6 was cleared prior to excavating Trench 2; only recent surficial materials were removed to expose the Quaternary "bedrock." The lower portion of the site was not excavated at this point, as the rising water level had concealed the area. A 2-m grid was superimposed on the cleared portion of the site using a Trimble Ranger handheld device with both a Trimble Pathfinder ProXH GPS receiver and a Trimble GeoBeacon GPS receiver, both of which have centimeter-scale resolution. Nails with flagging tape were driven into the ground at each

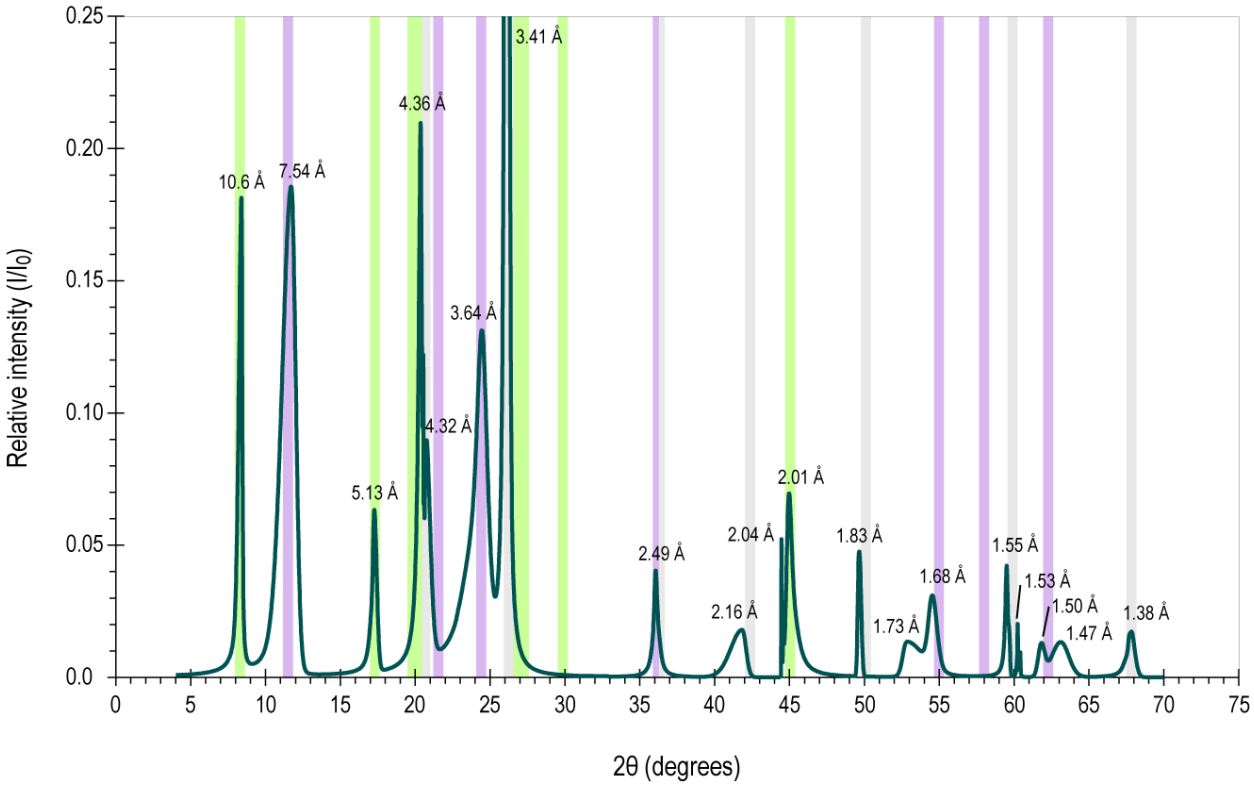


**Figure 2-9.** X-ray diffraction data obtained from sample DL-6-02. Background noise has been removed from the data to better illustrate peaks. The 3.41 Å quartz peak has a relative intensity ($I/I_0$) of 1; all other peaks have a relative intensity less than 0.25. Green bars—illite-2$M_1$ peaks; purple bars—kaolinite-1A peaks; gray bars—quartz peaks.

measured vertex to facilitate recognition of the grid during the next winter drawdown. Using this grid, the lower 4 m of the excavated area were mapped in detail, including the shale-terrace contact east of Trench 2. The rising water level prevented access to the site soon after mapping began, although it was determined that the next field season should focus on features in the Sevier Shale. Terrace alluvium north of the mapped 4 m contains few recognizable features due to soil development.

During the winter 2012-2013 drawdown of Douglas Reservoir, it was discovered that summer inundation of the site had preferentially eroded the sandy terrace alluvium and exposed a fault-line scarp of red clay extending northeast from Trench 2 (Fig. 2-10). This fault may be the same fault shown in Figures 1-9 and 2-8. The surface trace of the thrust fault was mapped using the grid laid in April, 2012. Additional clearing at site DL-6 was done to map the surface trace of the fault to the southwest of Trench 2 into terrace alluvium and Sevier Shale. The grid from April, 2012, was extended into the newly cleared area.

Plate 1 and Figure 2-11 show a complicated array of fractures and fault segments contained within the Sevier Shale outcrop at site DL-6. The southwestern continuation of the fault exposed in Trench 2 splays into multiple faults that have smaller displacements. Only one splay of this fault is continuously traceable through the entire mapped area. This fault splay was best identified by a 1 cm-thick gouge of red clay along the fault surface (Fig. 2-12). Pieces of the hanging wall were removed by excavation of the site, leaving extensive, continuous exposures of the red clay gouge. Similar exposures of red clay-coated fault surfaces occur throughout the site, although many are not as continuous, and those that were continue into areas not cleared. These features are identified with orange polygons in Figures 2-7, 2-11, and Plate 1,

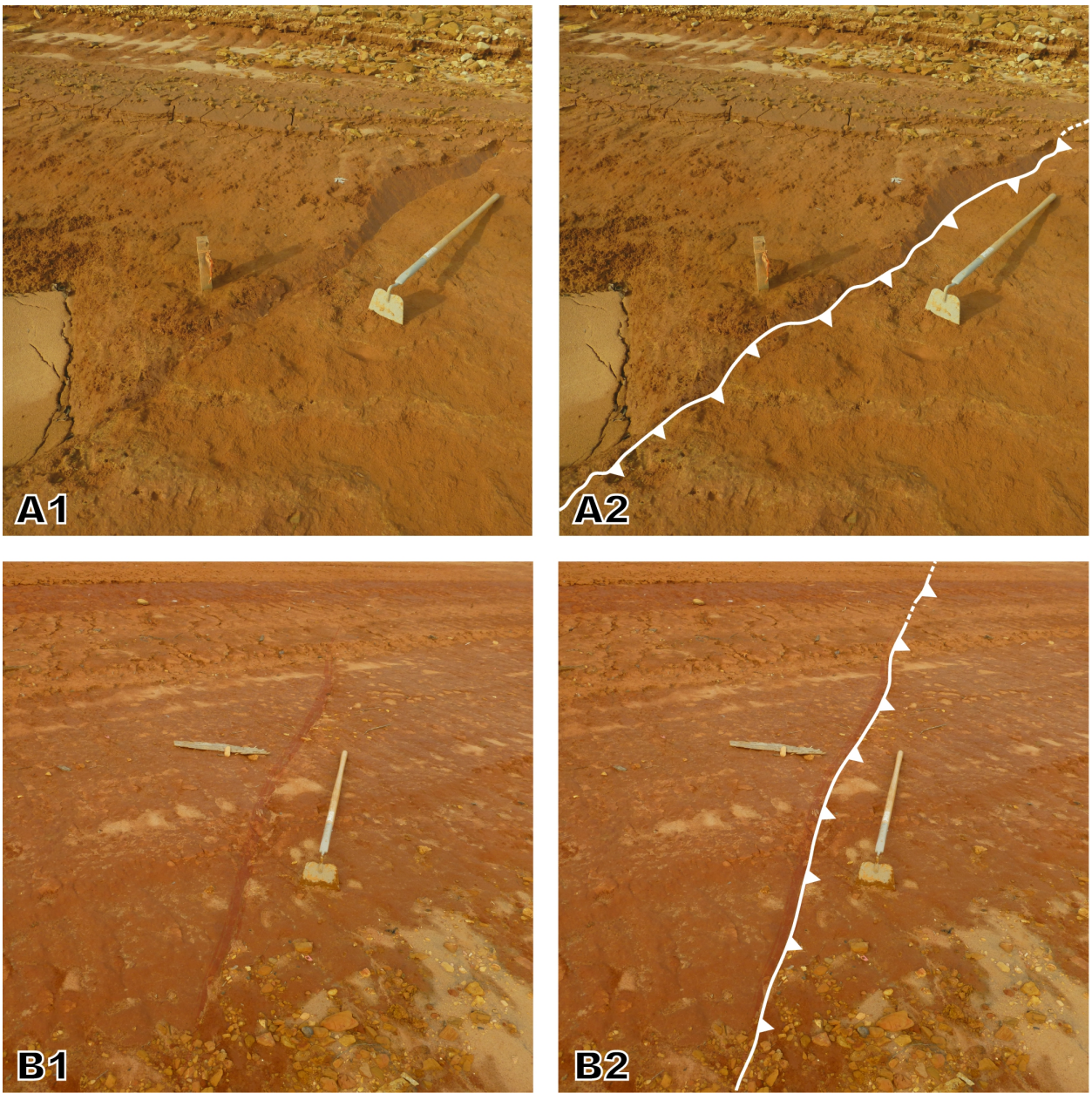


**Figure 2-10.** Fault-line scarp exposed after the summer 2012 inundation (locations in Fig. 2-7). (A1) Scarp exposed just E of the E-W portion of Trench 2; (A2) interpretation. Slickenlines are visible on the scarp face. (B1) Fault-line scarp exposed further uphill; (B2) interpretation. Hoe is ~125 cm long. (Photos by R.D. Hatcher, Jr.)

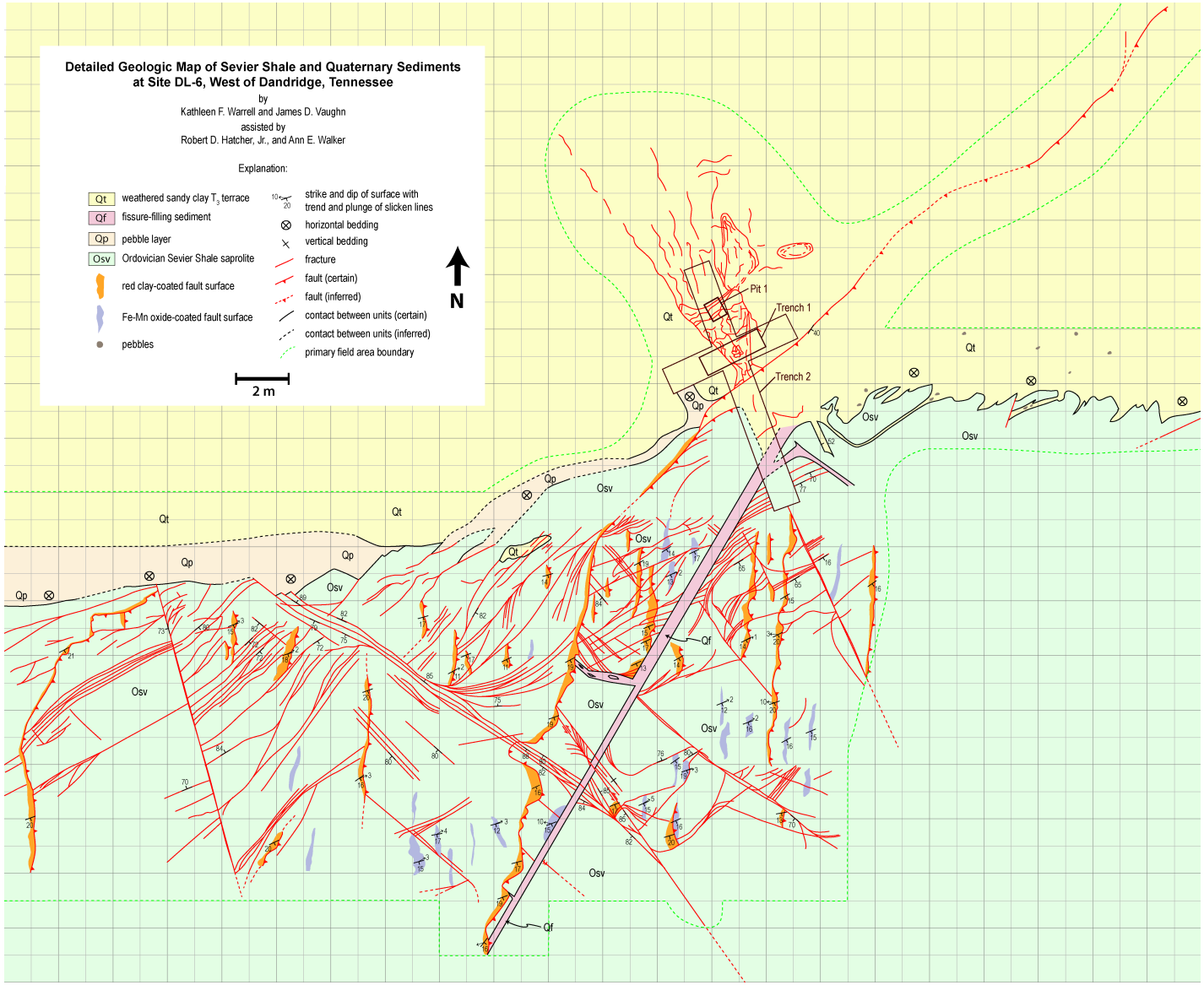


**Figure 2-11.** Detailed geologic map of fracture arrays and faults in Sevier Shale saprolite and Quaternary sediments at site DL-6, west of Dandridge, Tennessee.

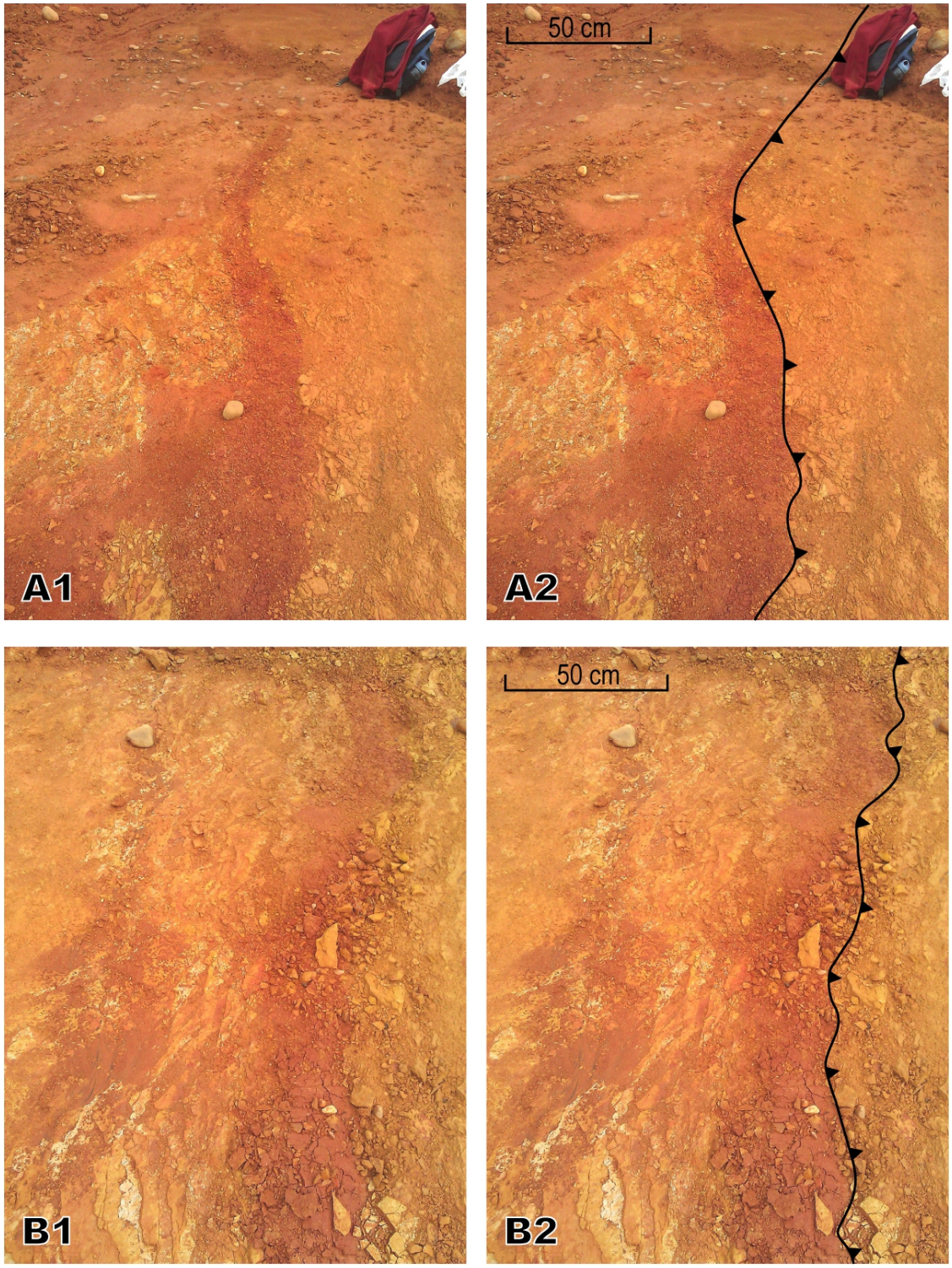


**Figure 2-12.** Clay gouge fault plane immediately west of the fissure (locations in Fig. 2-7). (A1) Clay-filled fault plane just west of Trench 2 with backpack for scale; (A2) interpretation. (B1) Clay-filled fault plane just north of the west-trending branch of the fissure, (B2) interpretation.

and, wherever possible, strike and dip measurements were made of the fault planes and trend and plunge measurements of the slickenlines (Fig. 2-13B). Slickenlines were also identified on Mn-Fe oxide-coated fracture planes (Fig. 2-14; purple polygons on Fig. 2-11 and Plate 1), although these Fe-Mn oxide-coated planes are not as areally extensive or as traceable through the map area as the clay-coated fault planes. Orientations of these planes and slickenlines were recorded as well (Fig. 2-13B and C).

X-ray diffraction analysis was also performed on the red clay gouge (Fig. 2-15). Quartz peaks are easily identifiable in the pattern. The 15.5 Å d-spacing (5.68° 2θ peak) is either a smectite group or chlorite group clay peak (Nesse, 2000). The peaks displayed match with a mixture of quartz, dickite (a polymorph of kaolinite), and saponite-15A, which is a smectite group clay. Saponite can form from weathering of Mg-rich limestones or dolostones in warm, moist climates (Post, 1984). Knox Group carbonates contain layers of dolomite, which may increase the concentration of Mg in local groundwater. The overall composition of this clay is different from other sediments identified in this study, and is likely related to enhanced weathering and flow of groundwater through the fractures or gouge from movement along fractures.

Crosscutting relationships between the fractures, faults, and fissures reveal a complicated deformation history. Trench 2 exposes a listric thrust fault offsetting Sevier Shale ~1 m uphill, with splays on both sides of the main fault (Figs. 1-9 and 2-8). This fault also forms the lower truncation of the sediment-filled fissure indicating that the fissure either formed prior to or during the faulting event. The continuous, clay-gouge fault just west of the fissure truncates the west-trending branch of the fissure (Fig. 2-16A), a small strike-slip fault with ~10 cm of offset

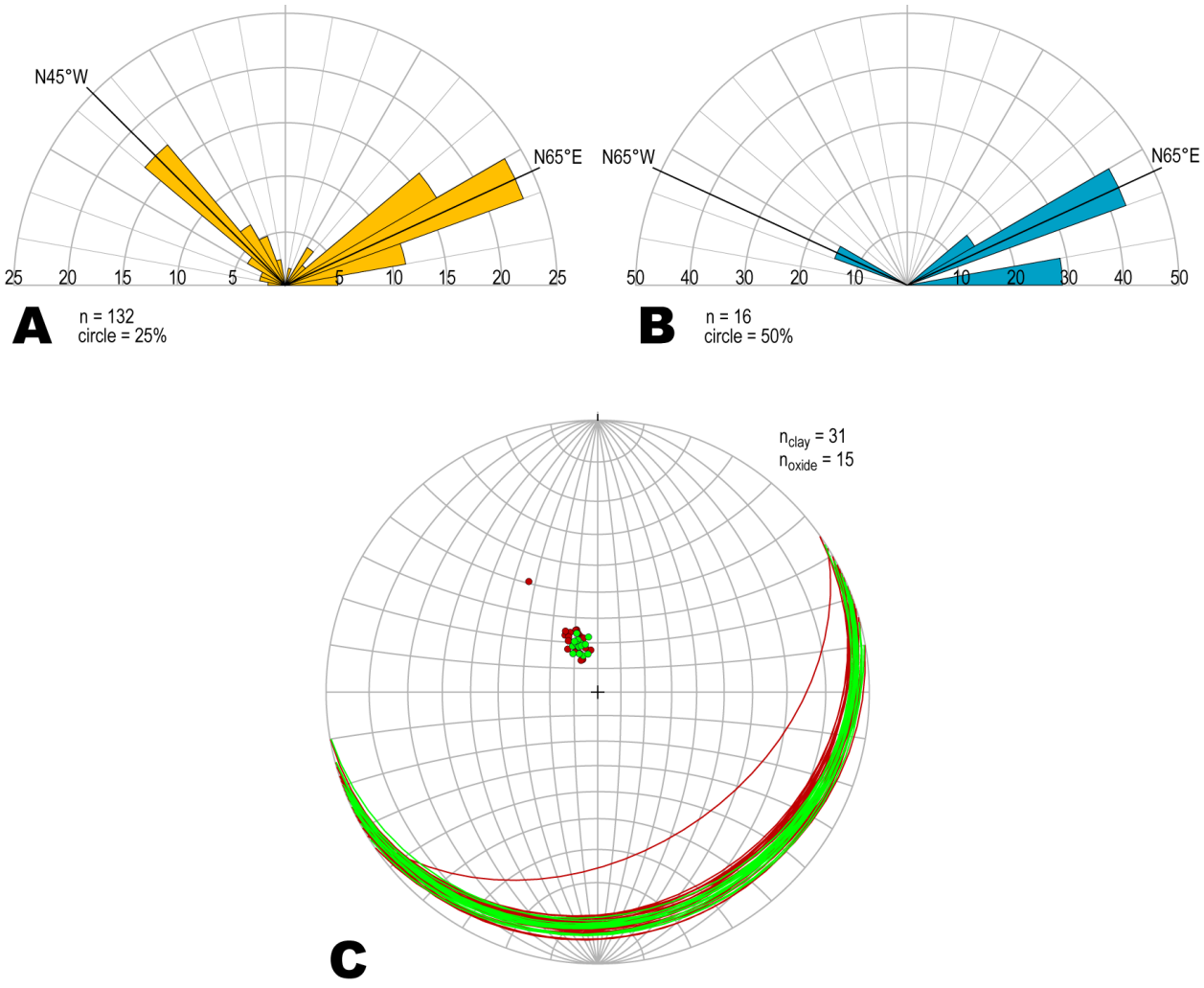


**Figure 2-13.** Rose diagrams and a stereonet from features on the detailed geologic map of site DL-6 in Figure 2-11 and Plate 1. The data used were directly measured in the field. (A) Rose diagram of fracture azimuths recorded from the map area. (B) Rose diagram of slickenline azimuths from the map area. The plunges of slickenlines are generally less than 5°. (C) Great circles and poles from fault surfaces in the map area. Red lines and poles—clay-coated fault planes; green lines and poles—Fe-Mn oxide-coated fault planes. (Plotted using software by Allmendinger et al., 2012.)


**Figure 2-14.** Iron-manganese oxide-coated fault surface cut by a clay-filled fracture at the top of the photo (location in Fig. 2-7). Slickenlines on this plane trend N60°E. Scale is aligned to the north.

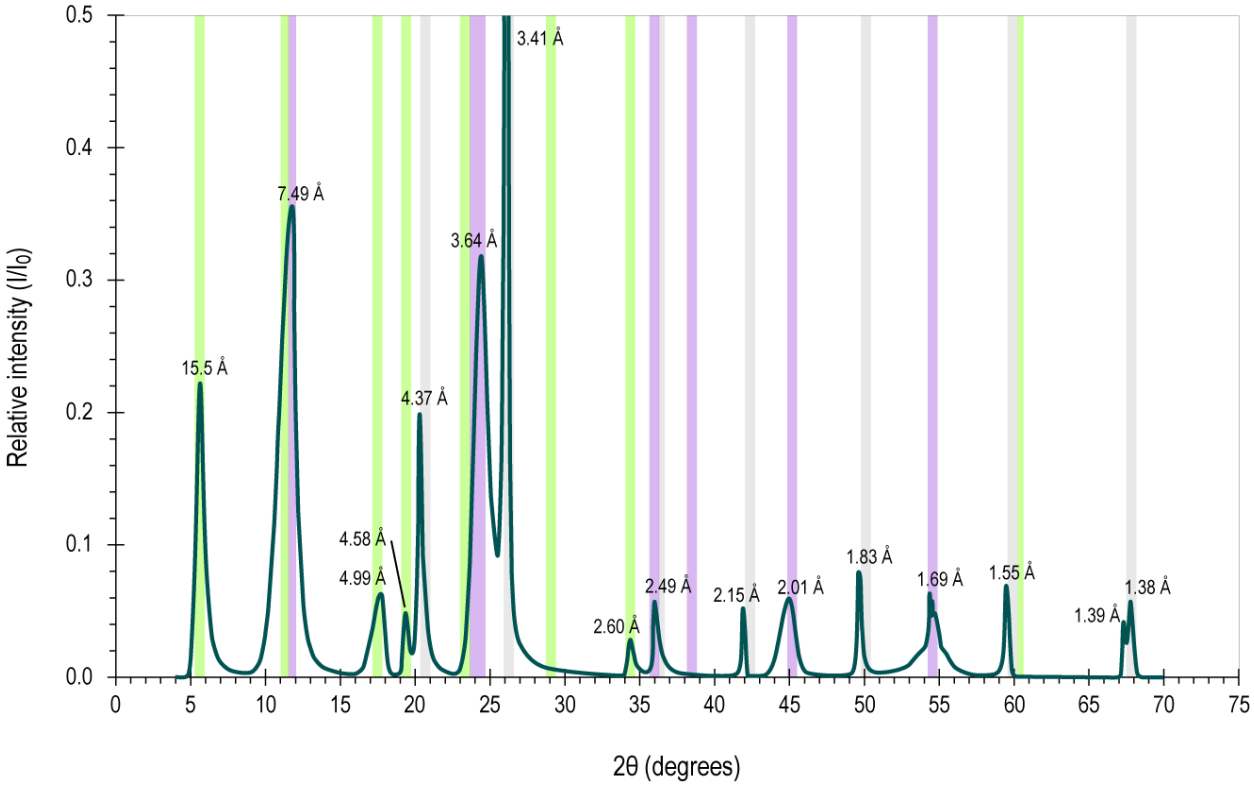


**Figure 2-15.** X-ray diffraction data obtained from clay gouge in the fault surfaces at site DL-6. Background noise has been removed from the data to better illustrate peaks. The 3.41 Å quartz peak has a relative intensity ($I/I_0$) of 1; all other peaks have a relative intensity less than 0.5. Green bars—saponite 15A peaks; purple bars—dickite peaks; gray bars—quartz peaks.

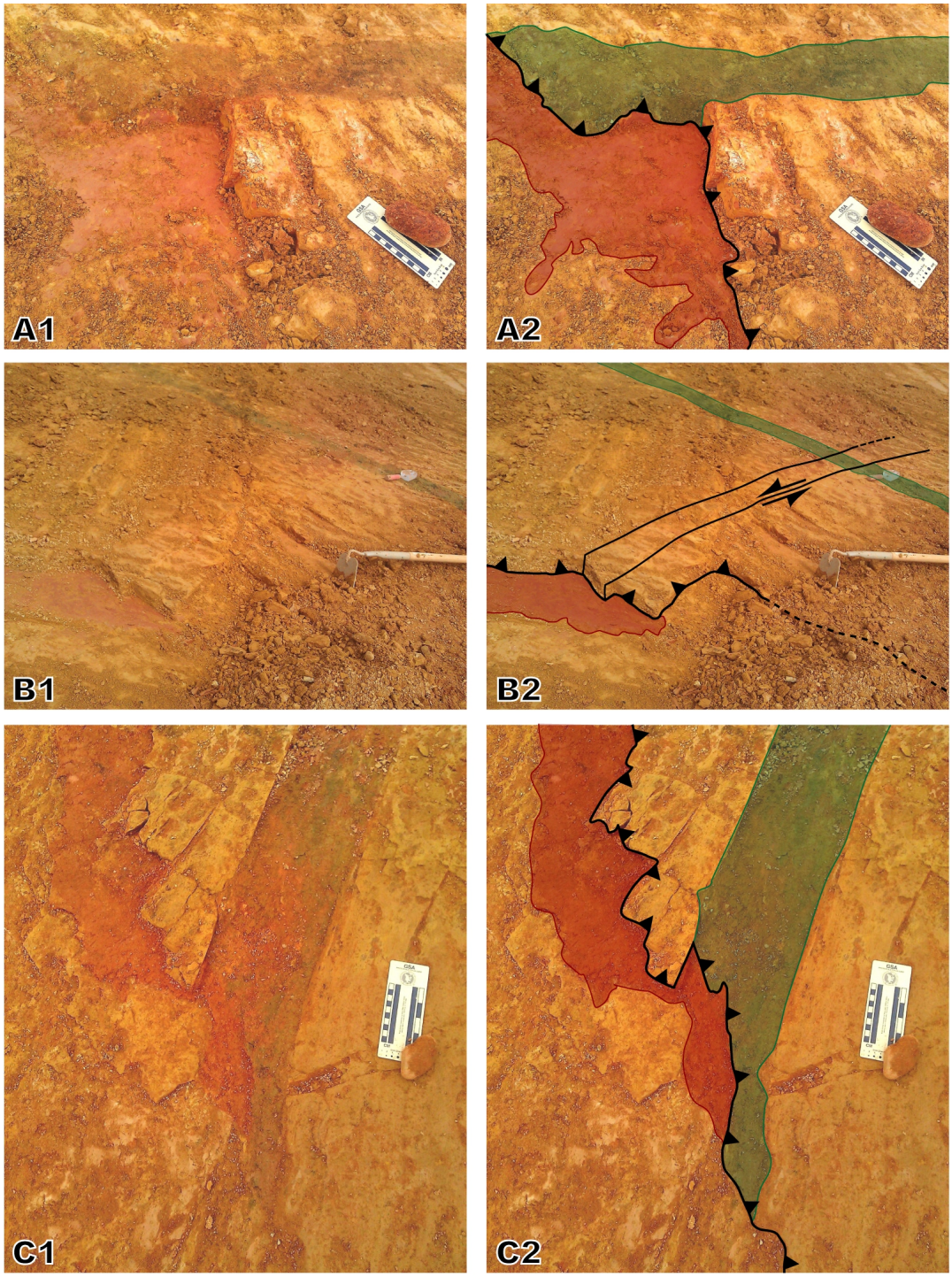


**Figure 2-16.** Continuous clay gouge immediately west of the fissure (locations in Fig. 2-7). (A1) Truncation of the W-trending branch of the fissure against the fault; (A2) interpretation. (B1) Truncation of the sinistral strike-slip against red clay gouge; (B2) interpretation. (C1) Truncation of the southern end of the fissure against the fault plane; (C2) interpretation. Green fill—fissure fill sediment; red fill—clay gouge on fault.

(Fig. 2-16B), and the southern end of the main fissure (Fig. 2-16C). The strike-slip fault truncated by the thrust fault from Trench 2 offsets the fissure, indicating that the fissure-forming event occurred prior to formation of the thrust fault in Trench 2, and that the fissure did not open as a result of tensional stresses in the hanging wall of the thrust fault. There is one set of northwest-trending fractures that are continuous on both sides of the thrust fault; several splays off of this fracture set curve northeast, and some appear to merge with the fault. This fracture set may have been either a preexisting Paleozoic fracture set that was reactivated, or a later fracture set that formed during recent faulting. In either case, the curved northeast-trending splays formed later, likely at the same time or immediately before the event that produced the fault in Trench 2.

The relationship between the terrace sediments (Qt and Qc) and the Sevier Shale (Osv) is also complicated and displays crosscutting relationships with the fractures. The terrace sediments have been subdivided into a coarse-grained, poorly sorted, weakly cemented conglomerate and a well-sorted, fine-grained sand (Fig. 2-17). The conglomerate has clast sizes ranging from sand to boulder; a layer of red clay coats intact clasts, and clasts that are not intact have been weathered to colored sand. The conglomerate occurs below the sandy terrace sediments, but is not continuous across the entire map area. The layer pinches out several times and decreases in thickness to the east (Fig. 2-17). East of Trench 2, the conglomerate layer either was not deposited or does not outcrop. This may be the result of local depositional environment of the area: swift currents in the tributary channel during storm flow were able to carry large clasts; after flowing into the main channel, the velocity changes direction and decreases, releasing clasts from suspension at the confluence at the western part of site DL-6.

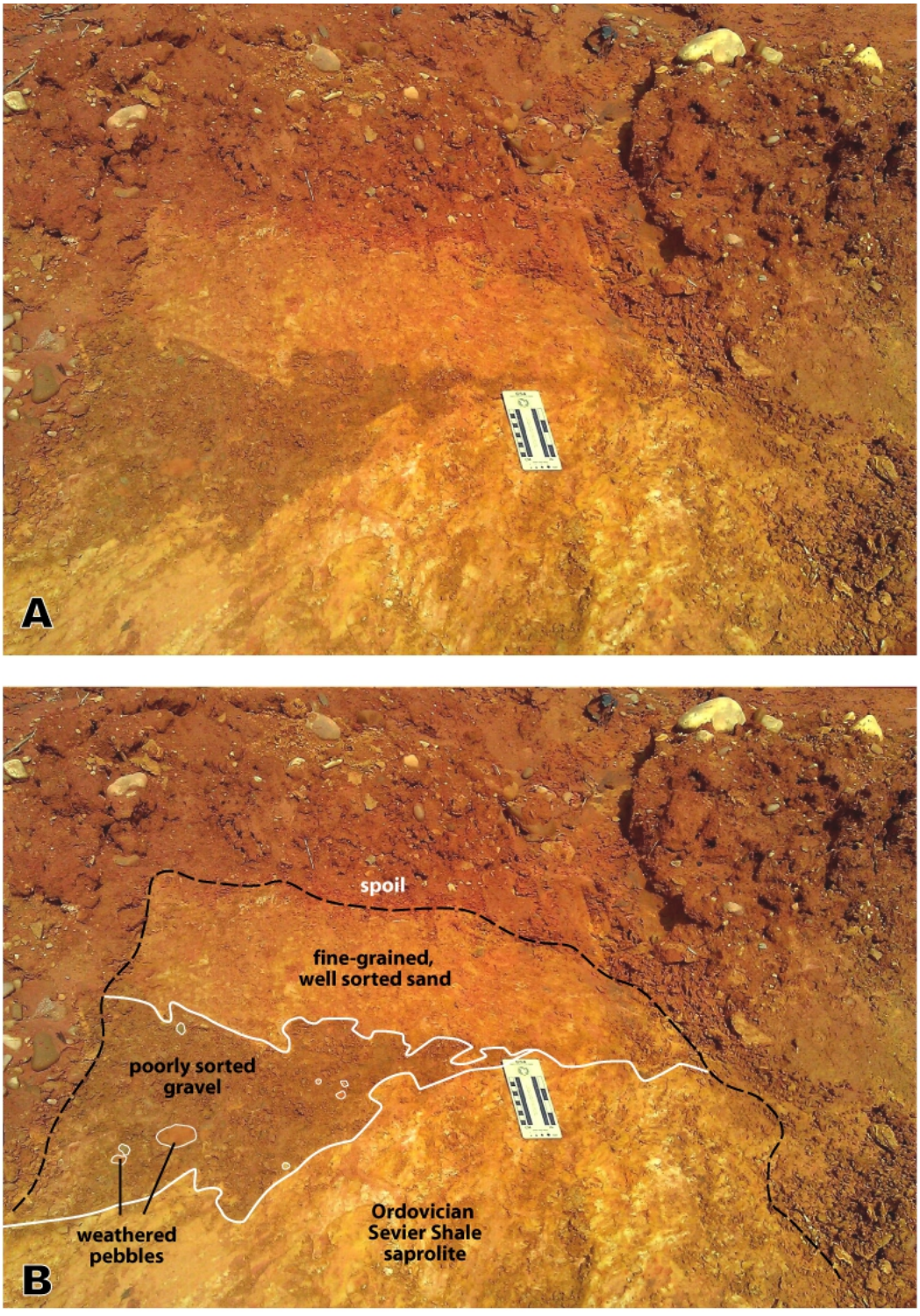


**Figure 2-17.** (A) Contact between Sevier Shale saprolite and younger terrace materials (location in Fig. 2-7). The darker gravel pinches out at this location and overlying fine sand is juxtaposed against shale saprolite. (B) Sketch overlay with interpretations.

The continuation or truncation of fractures is also variable from the shale bedrock into Quaternary sediments. The northwest-trending fracture set contacts the conglomerate (Fig. 2-18A), and the contact has a "stair-stepped" outcrop pattern. This pattern may indicate a small amount of offset along each of these fractures, although the displacement is not traceable into the conglomerate; erosional plucking of chips from the shale surface prior to gravel deposition is also a likely explanation. Farther west, the prominent, single northwest-trending fracture also contacts the conglomerate (Fig. 2-18B). This fracture truncates many smaller fractures, which may indicate that it is a fault, or that the fracture is older than those it truncates and is a barrier to fracture propagation. The contact of this fracture with the overlying conglomerate does not display any measurable displacement, nor does it continue into the conglomerate. If this fracture is a fault, it is either an old fault that has been eroded to a smooth surface prior to terrace deposition, or a young fault with no horizontal displacement. To the east where the conglomerate pinches out, the contact with overlying sandy terrace alluvium displays a different relationship. In a patch of sandy terrace alluvium filling a depression in the shale, clay-filled fractures were discovered that are continuous from the shale saprolite into the sand (Fig. 2-18C). In the eastern portion of the site, additional fractures continue into sandy alluvium (Fig. 2-19). This indicates that fractures can propagate from shale into alluvium as long as the alluvium is sandy; coarse-grained, gravelly alluvium may provide a barrier to fracture propagation.

***Summary***

The fractures and faults at this site indicate that there have been events affecting the site in the Quaternary, specifically since deposition of the terrace materials, which OSL dates indicate were deposited >103,460 years ago (Hatcher et al., 2012). The fault in Trench 2 is traceable as

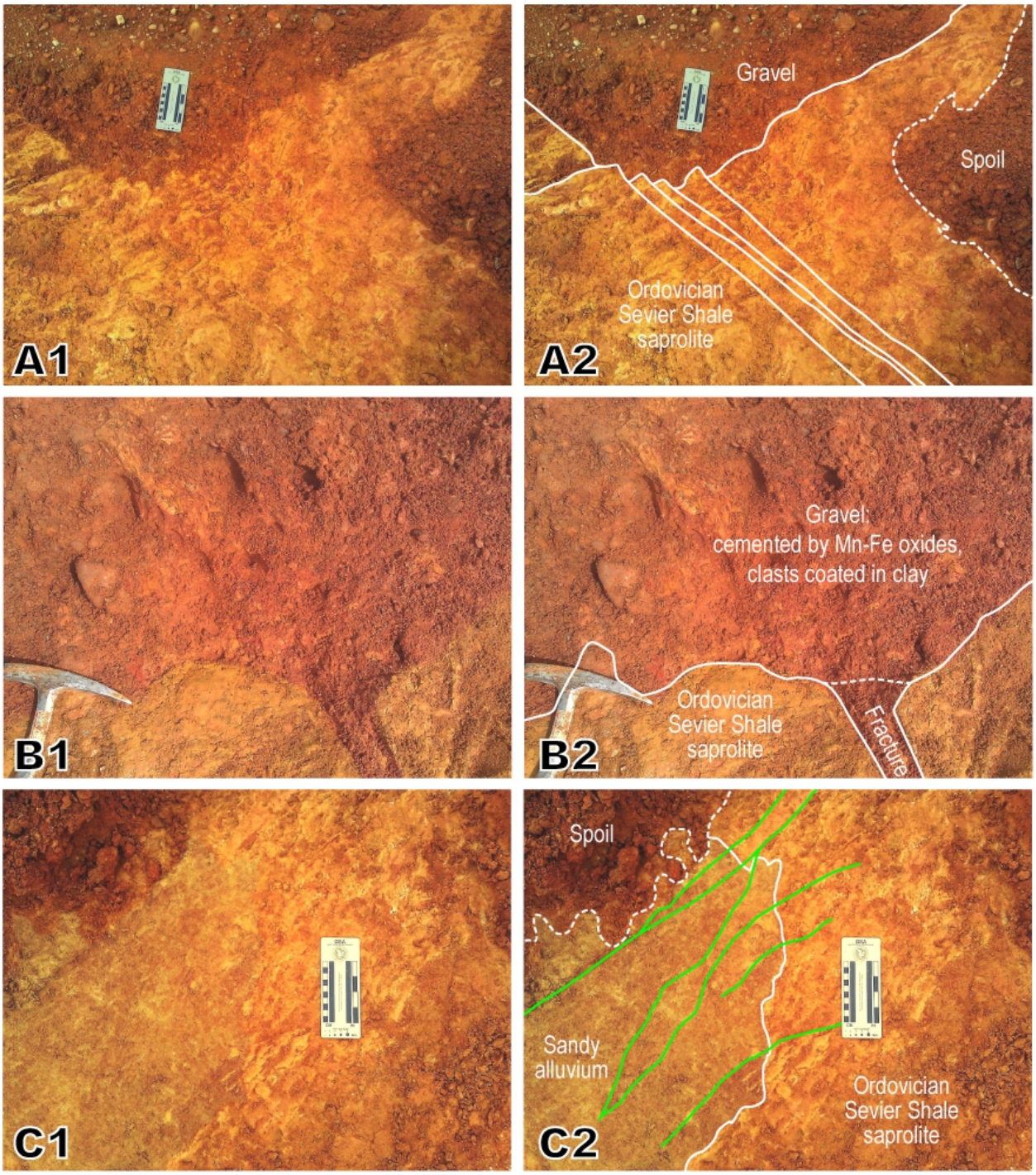


**Figure 2-18.** Contact relationships between fractures in Sevier Shale saprolite and overlying Quaternary sediments (locations in Fig. 2-7). (A1) Truncation of northwest-trending fracture set into overlying gravel; (A2) interpretation. The "stair-stepped" nature of the contact may indicate slip along these fractures. The fractures do not continue into the gravel. (B) Truncation of a large, northwest-trending fracture into overlying gravel; (B2) interpretation. (C) Fractures that are continuous from sandy Quaternary alluvium into Sevier Shale saprolite; (C2) interpretation; fractures outlined in green.

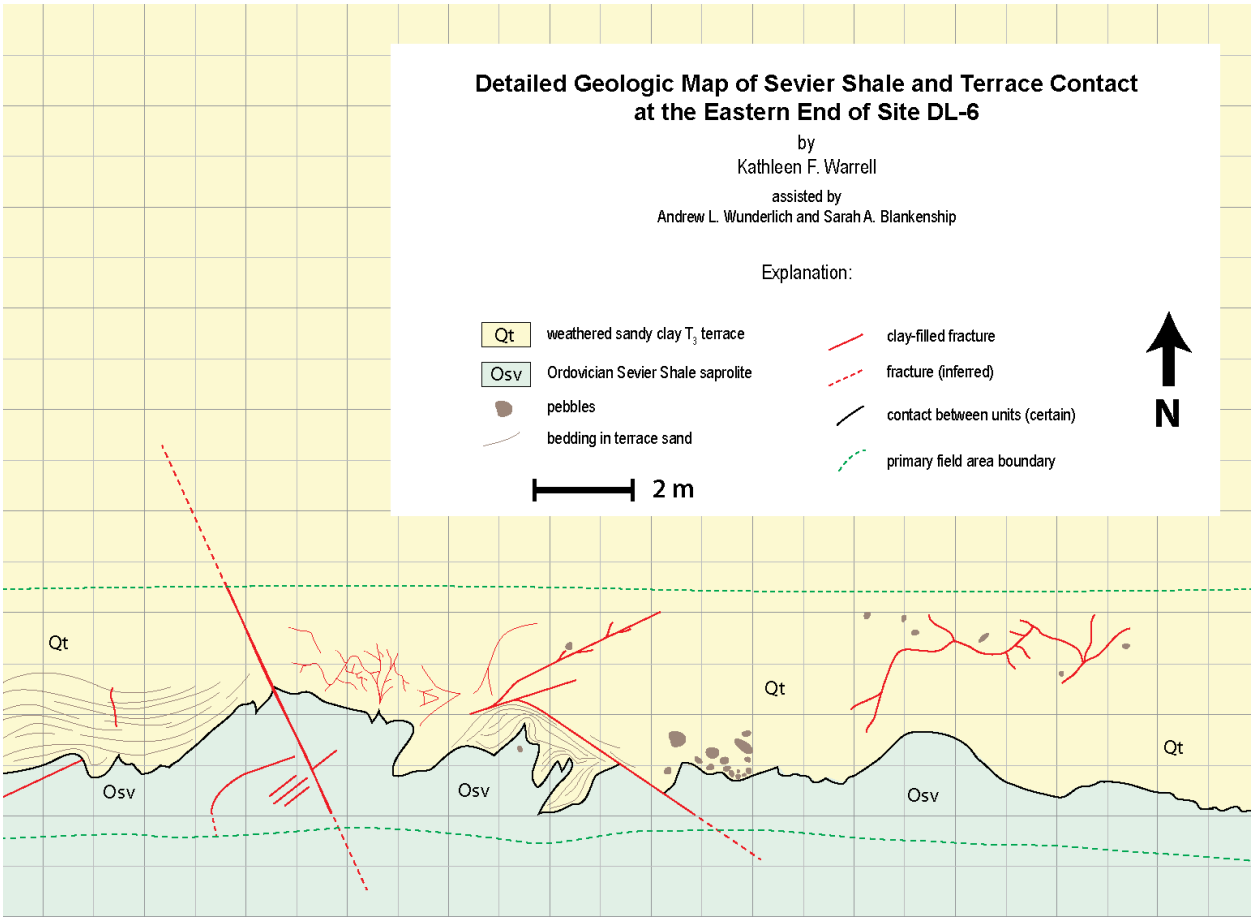


**Figure 2-19.** Detailed geologic map of Sevier Shale and terrace contact at the eastern end of site DL-6. Note how the two prominent NW-trending fractures continue from the shale into the sandy terrace alluvium, and how the pebble layer does not occur in this outcrop.

one fault to the east in Quaternary terrace sediments. To the west, displacement on the fault is partitioned into multiple splays as the fault enters Sevier Shale saprolite, which is a medium significantly different from sandy sediment. These faults and fractures display a complicated geometry: both linear and curved shapes are present. Slip on these fault planes is along strike for the most part. Events along this fault are later than ~17 ka (Table 2-1), with possible events around 11,880 ± 1,420 y and 4,890 ± 700 y, which may have resulted in the removal and refilling of portions of the sediment-filled fissure. It is also likely that these sediments may have been eroded and new sediments deposited by over-land water flow unrelated to a seismic event.

## *CHAPTER III*

## *PALEOSEISMIC EVIDENCE NEAR LYERLY, GEORGIA*

### Study Area

Lyerly, Georgia, is located ~50 km south-southwest of Chattanooga, Tennessee, and lies at the southwest edge of the East Tennessee seismic zone (Fig. 1-1). There have been three M > 4 earthquakes in this area since 1964. This study focuses on stream terraces along a portion of the Chattooga River in Chattooga County, Georgia, that lies in the Appalachian foreland fold-thrust belt. The valley through which the Chattooga River flows at this location is underlain by shale belonging to the Conasauga Group (Lawton et al., 1976). Terraces along the Chattooga River have not been mapped, nor have their ages been determined. Estimates of terrace ages for this study are based on the degree of soil development in each terrace. Land use in the area appears to be a mixture of forest, pasture, and crop-based agriculture (including cotton, corn, and soybeans).

### Paleoseismic Evidence at the Taylor Farm Site (34.37513° N, 85.41428° W)

The Taylor Farm lies on the inside of a meander along the Chattooga River (Fig. 3-1). The $T_1$ terrace lies 3-4 m above the current stream level and 1-2 m above the modern floodplain. The banks are highly vegetated, making it difficult to identify features exposed in cross section in the bank. The data here consist of aerial photo recognition of possible liquefaction features and XRD analyses of sediments from those features. Land use for this farm has been mostly pasture for the past several decades, although sand was mined from a portion of the site ~60

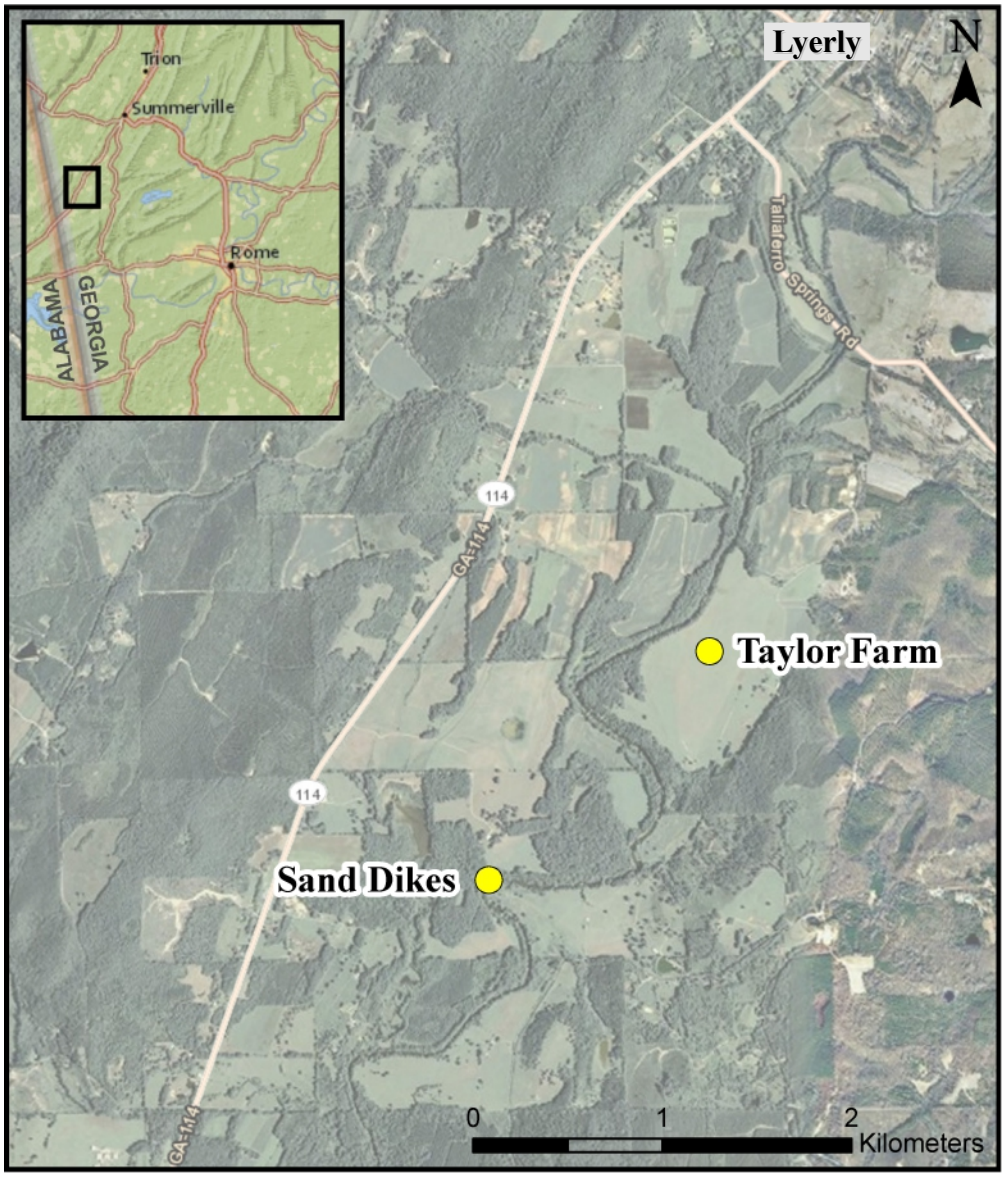


**Figure 3-1.** Mapping locations along the Chattooga River, just south of Lyerly, Georgia. (Imagery from ArcGIS and inset from National Geographic.)

years ago (James Taylor, personal commun.). This site is an appropriate candidate for recovery of sand-blow deposits, because there has been no invasive plowing since the advent of modern agricultural equipment, which can easily obliterate sand-blow deposits.

***Identification of possible liquefaction features on aerial photographs***

Focus on the Taylor Farm site was initiated via the occurrence of circular to slightly elliptical features in a 1993 USGS aerial photo that could potentially represent sand blows (Hatcher et al., 2011). Further investigation on this front has involved the acquisition of 1943 aerial photos from the Agricultural Stabilization and Conservation Service (ASCS) from the National Archives in College Park, Maryland. The 1943 aerial photo of the James Taylor Farm site shows some areas of tonal anomalies that are coincident with those in the 1993 photo (Figs. 3-2 and 3-3). Tonal anomalies such as these have been used to identify sand blow cones in the New Madrid seismic zone and Mississippi Embayment (e.g., Cox et al., 2007). The tonal anomaly is produced by the excess sand, which appears lighter in color than the surrounding soil; sand does not readily support vegetation, so vegetation tends to be sparse on sand blow cones, enhancing the contrast between the sand blow cones and surrounding area. The persistence of these tonal anomalies throughout time indicates that they are not related to some short-term phenomenon, such as a fungus affecting the vegetation or dispersion of hay bales by cattle.

***X-ray diffraction analysis of sediment samples***

Multiple high, light-colored areas at the James Taylor Farm site were identified during a field traverse in July, 2012 (Fig. 3-4). These light-colored areas are near the northern set of tonal anomalies in Figures 3-2 and 3-3. Samples of the light-colored areas and surrounding darker-colored soil were collected for later analysis.

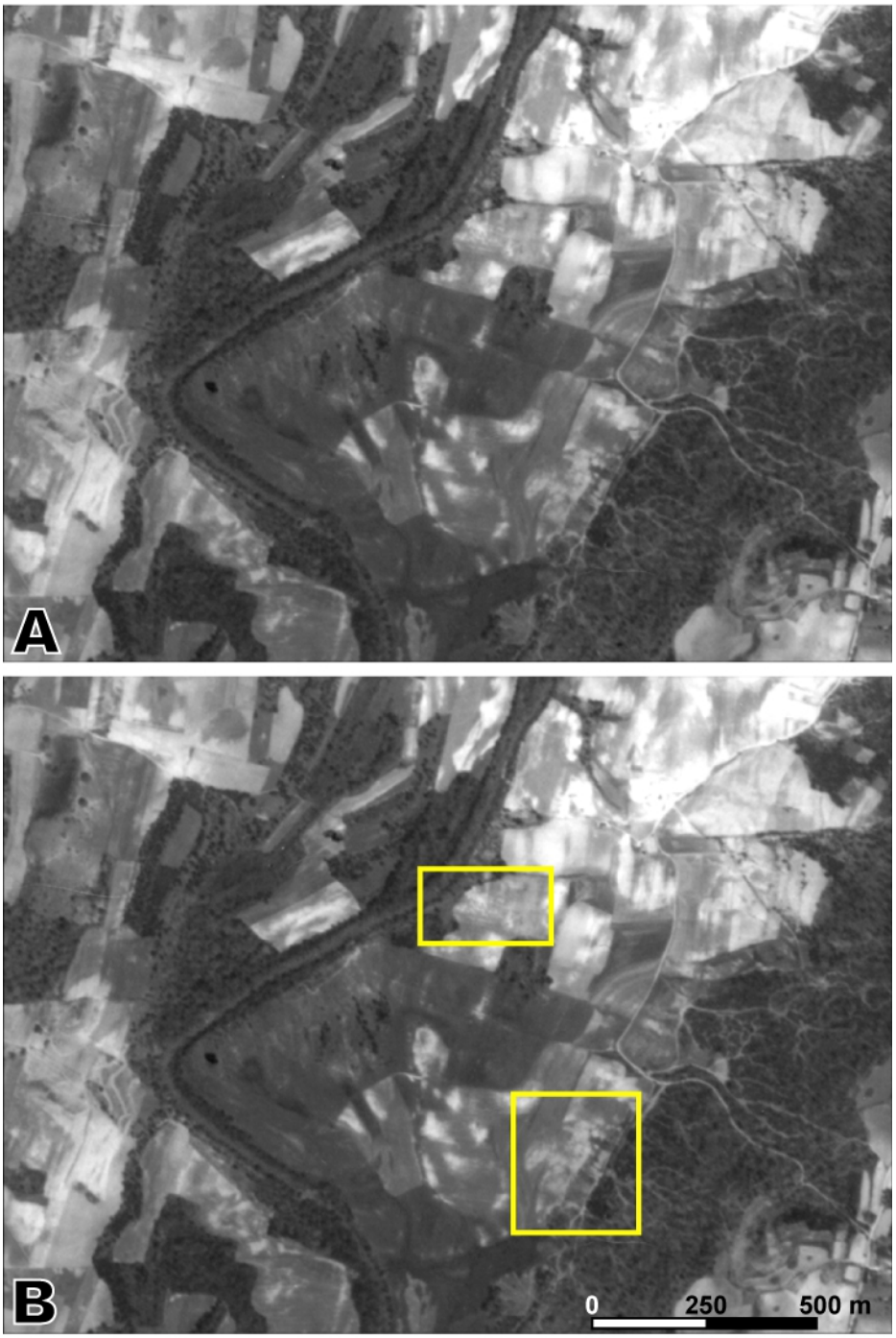


**Figure 3-2.** (A) Portion of a 1943 ASCS aerial photo showing the Taylor Farm site (Fig. 3-1); (B) tonal anomalies of interest are highlighted. Note that the highlighted areas in both Figures 3-2 and 3-3 contain small, rounded tonal anomalies, and that the tonal anomalies at this site persist for at least 50 years. The highlighted area in the northern portion of the site is approximately where high, light-colored areas were identified during the July, 2012, field traverse.

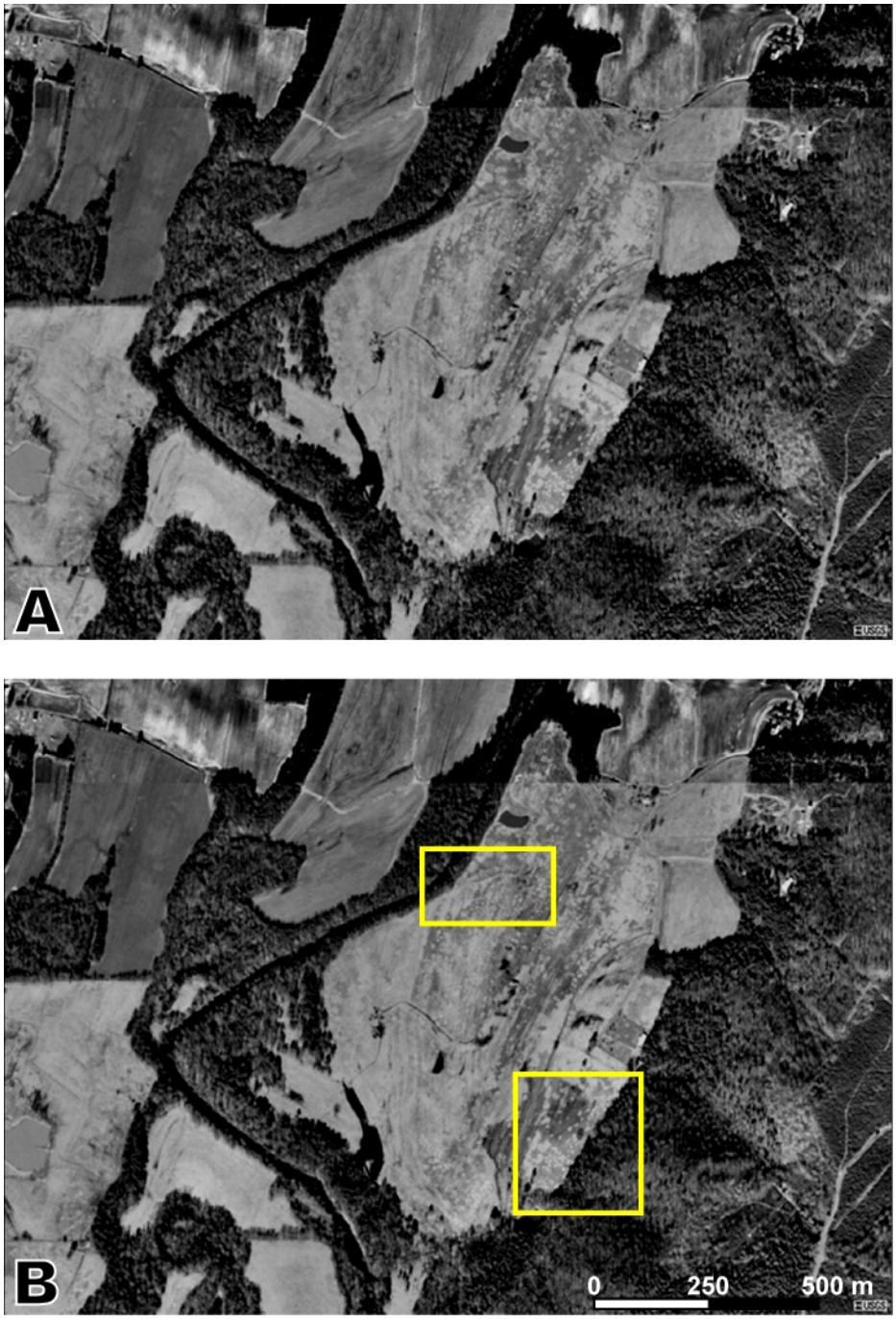


**Figure 3-3.** (A) Higher resolution 1993 USGS aerial photo of same area as in Figure 3-2A; (B) overlay of the same highlighted areas in Figure 3-2B. Note that the highlighted areas in both Figures 3-2 and 3-3 contain small, rounded tonal anomalies, and that the tonal anomalies at this site persist for at least 50 years. The highlighted area in the northern portion of the site is approximately where high, light-colored areas were identified during the July, 2012, field traverse.

**Figure 3-4.** High, light-colored sandy area surrounded by low, dark-colored soil at Taylor Farm. Note that grass does not grow as thickly in the light area, which may be related to the lack of a developed organic soil horizon. Hammer is ~30 cm. (Photo by R.D. Hatcher, Jr.)

XRD analyses were performed to determine compositional variations between the two sediments. Sediments were air dried before being ground to a fine powder with a mortar and pestle. The powdered sediment was then pressed into the depression of an XRD powder slide and analyzed. There are no significant differences in mineral composition between the two samples in the XRD analyses (Fig. 3-5). Both samples are composed mostly of quartz, with few other constituents. There are some minor peaks ($I/I_0 \leq 0.01$) that are not coincident in both samples, but these are not associated with any specific clay mineral (pink bars in Fig. 3-5). It should be noted that analysis by XRD cannot detect organic, noncrystalline constituents in the samples, and these may comprise the minor compositional differences between the two samples.

## Paleoseismic Evidence at the Sand Dikes Site (34.36341° N, 85.42666° W)

Two sand dikes are exposed on a steep, 3 m-high cut bank on the west bank of a sharp meander along the Chattooga River (Fig. 3-1). These sand dikes were discovered during a canoe traverse in July, 2012, by Dr. Randel T. Cox and myself. These sand dikes are 5-10 cm wide and extend upward ~0.5 m from a source sand bed that occurs just above the water level (Fig. 3-6). The sediment in the dikes consists of fine, subangular to subrounded, light gray sand with ~10 percent chert and opaques (R. T. Cox, personal commun.). The surrounding "host" sediment is a red clayey sand with yellow-brown mottling (Fig. 3-6). The host material is likely part of a Holocene to latest Pleistocene $T_1$ or $T_0$ terrace (R.T. Cox, personal commun.). Samples of the host material, sand dikes, and source bed were collected for analysis.

### *Analyses of sediment samples for liquefaction criteria*

The host, sand dike, and source bed sediments were air dried for one week prior to

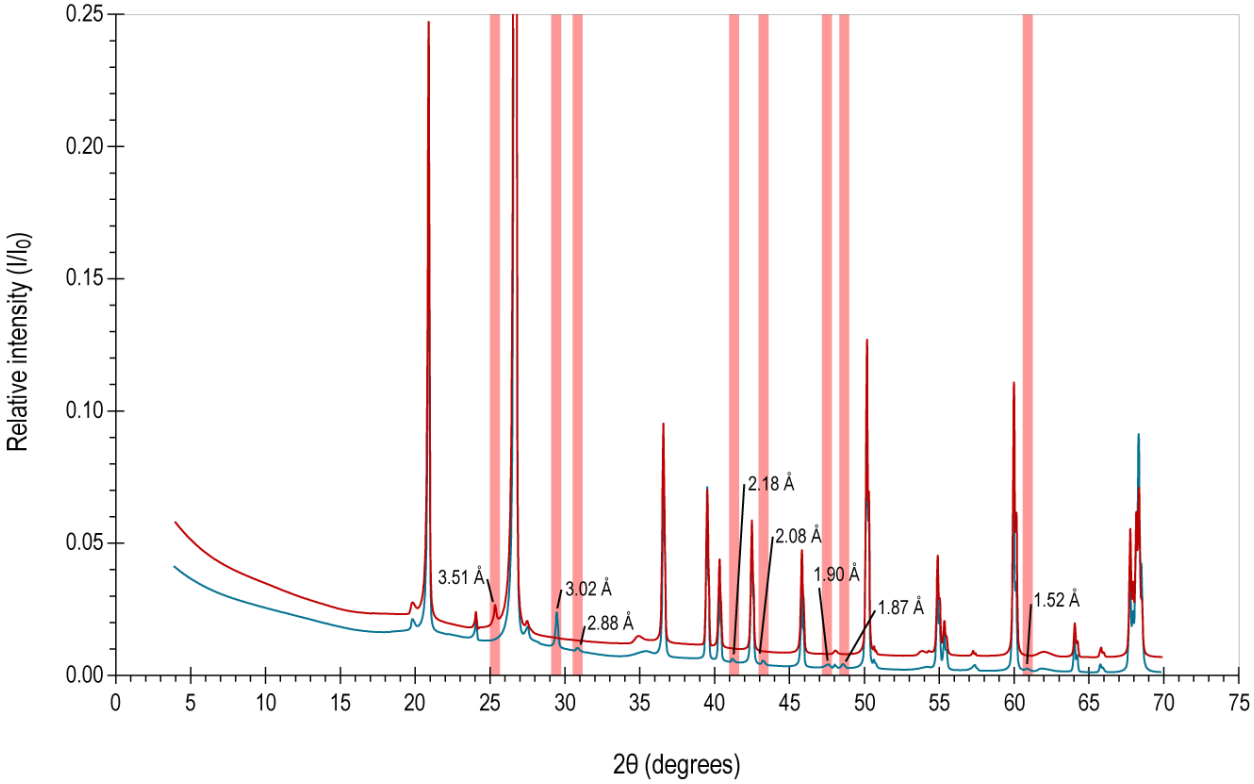


**Figure 3-5.** X-ray diffraction data obtained from samples of the high, light-colored areas (red line) and low, darker-colored areas (blue line). The relative intensity from the low areas has been decreased $I/I_0$ = 0.005 to better show differences in the data. Pink bars indicate peaks that are not present in both samples; d-spacings are shown only for these peaks. The 26.7° quartz peak has a relative intensity ($I/I_0$) of 1; all other peaks have a relative intensity less than 0.25.

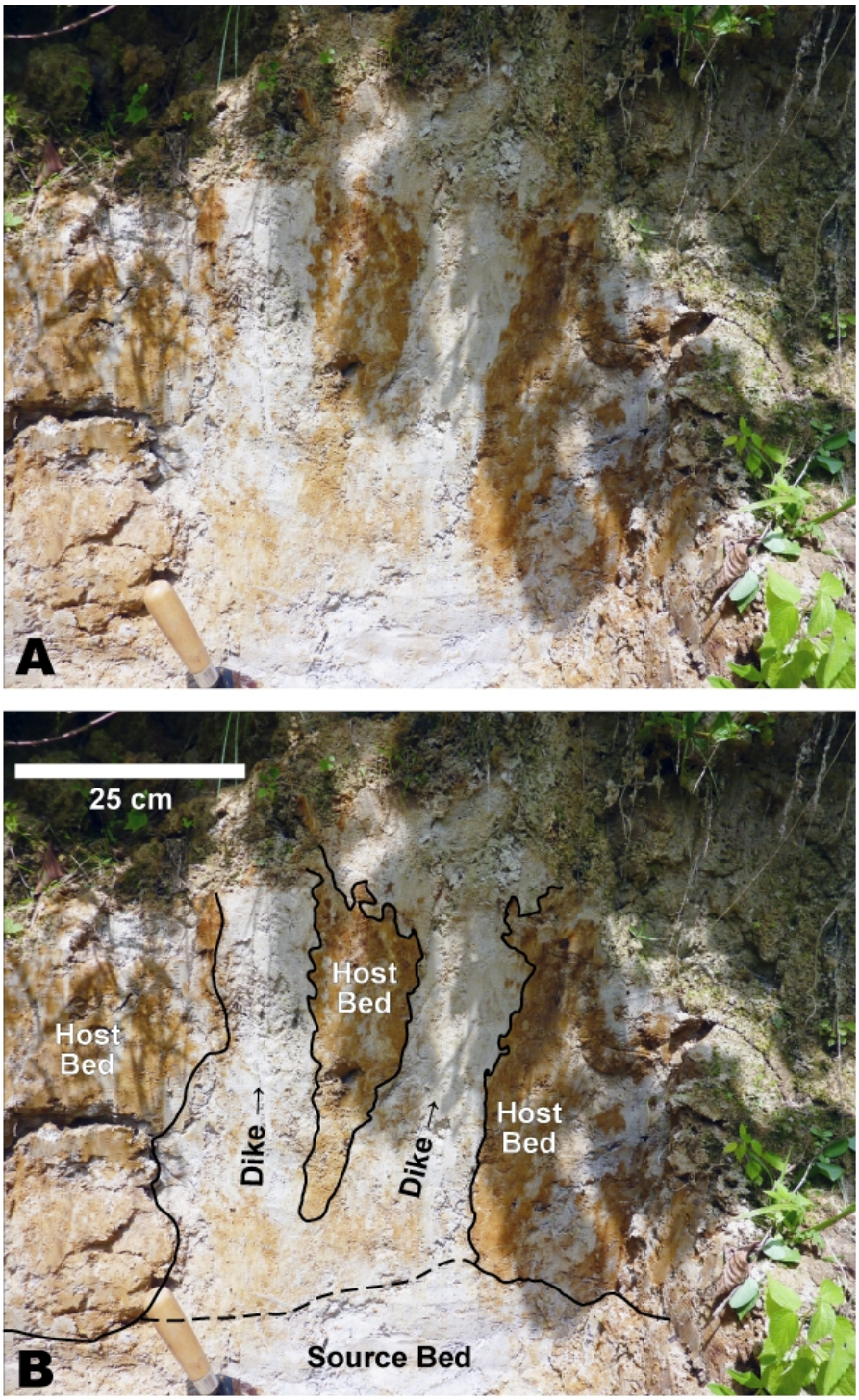


**Figure 3-6.** (A) Sand dikes exposed in a cut bank of the Chattooga River, south of Lyerly, Georgia. The white sand dikes extend from a source bed of similar white sediment, cutting through the mottled red and gray alluvium; (B) interpretation; dashed line indicates approximate boundary between source bed and sand dikes. (Photo by R.T. Cox)

performing grain-size analyses. Sediments were gently disaggregated using a mortar and pestle. Approximately 95 g of the host, 210 g of the sand dike, and 160 g of the source bed materials were sieved to measure grain size. Sediments were weighed on a calibrated scale and sorted in a Ro-Tap for approximately 30 minutes. The grain-size separations were then reweighed using the same scale.

Grain-size analyses of the host material, sand dikes, and source bed show that all three materials are similar in particle size distributions, but the host material is slightly more fine grained (Fig. 3-7A). The sand dike material is the coarsest. All three materials fall within the range of sediments that are most susceptible to liquefaction (Fig. 3-7B) (Tsuchida and Hayashi, 1971). For liquefaction to occur, it is preferred that the host material be finer grained and possibly clay rich so that the pressure in the underlying source bed can build up and hydraulically fracture the host material (Obermeier, 2009).

XRD analyses were conducted on all three samples to further determine the differences and similarities between the three sediments. Initially, the bulk sediments were air dried before being ground to a fine powder with a mortar and pestle. The powdered sediment was then pressed into the depression of an XRD powder slide and analyzed. The results reveal few differences between the peaks of the X-ray spectra, but a very slight difference occurs in the background of the host material data (Fig. 3-8A). The dominant mineral in the peaks is quartz.

To further investigate the slight differences between the sediments, the samples were run a second time, but this time the sediments were suspended in water to let the majority of the quartz grains settle out. The elutriated sediments were pipetted onto a slide and allowed to dry for 48 hours before analysis by the XRD. The data did not yield the same peak differences, nor

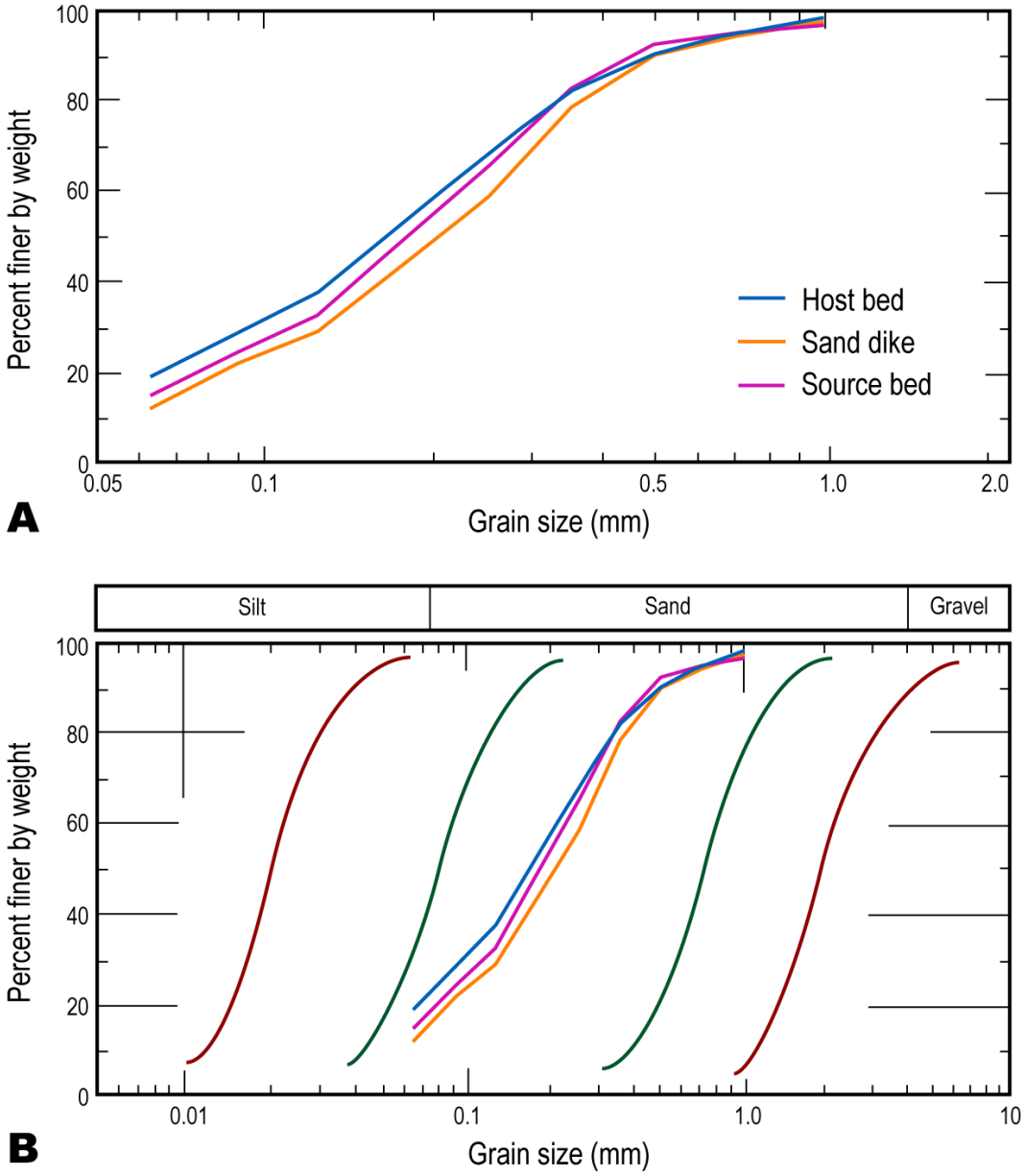


**Figure 3-7.** (A) Grain-size analyses obtained from the host bed (blue), sand dike (orange), and source bed (fuchsia). Note that the host bed has the finest overall grain-size of the three sediments. (B) Overlay of the grain size data on the liquefiable grain-size limit plot from Tsuchida and Hayashi (1971) (Fig. 1-3A). Green lines—most liquefiable sediments; red lines—potentially liquefiable sediments.

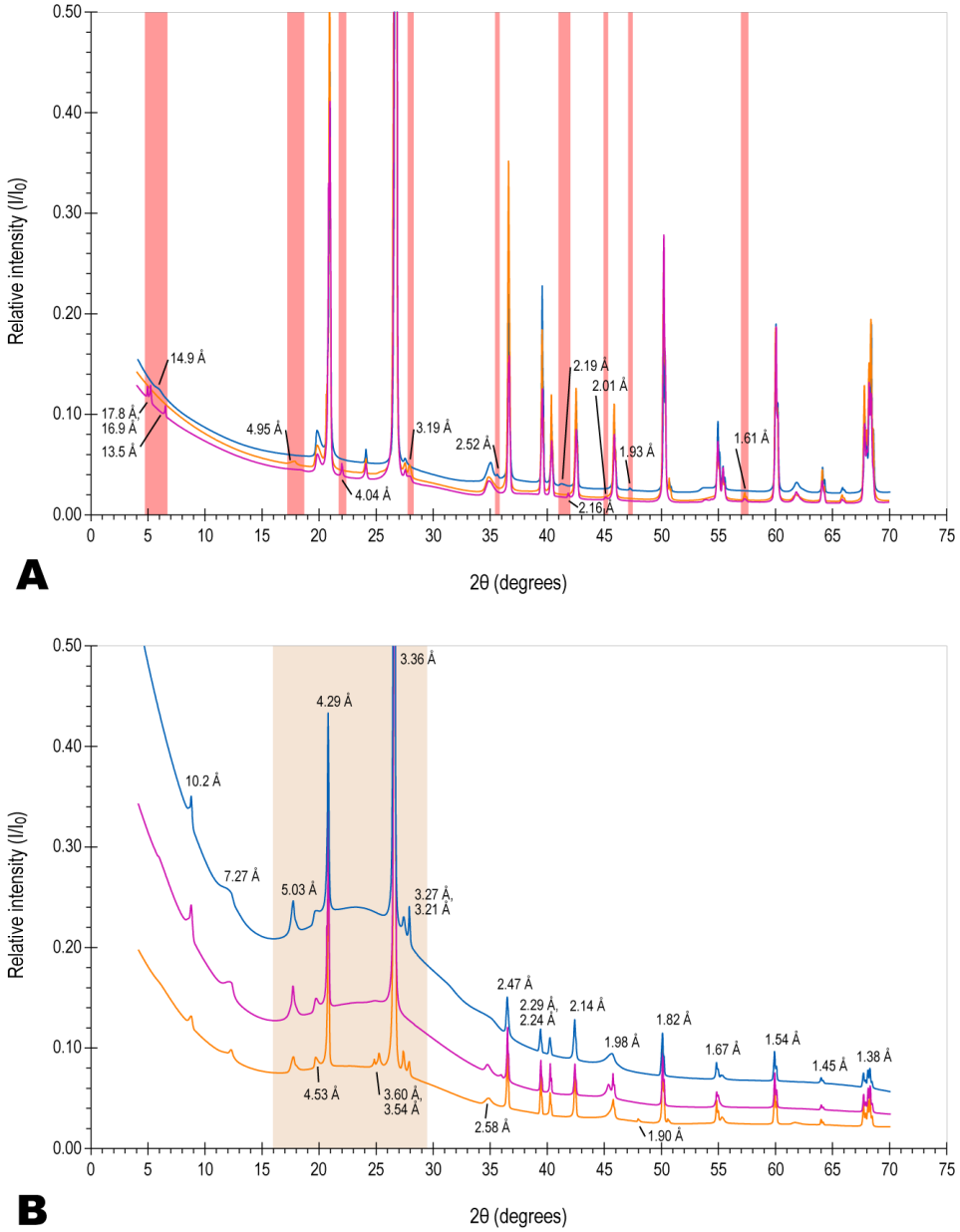


**Figure 3-8.** (A) X-ray diffraction data obtained from powdered samples of the host bed (blue), sand dike (orange), and source bed (fuchsia). Note that the sand dike data nearly overlay the host bed data where 2θ is greater than 30°. Pink bars indicate locations of peaks that are not present in all three samples; d-spacings are shown only for these peaks. The 26.7° quartz peak has a relative intensity ($I/I_0$) of 1; all other peaks have a relative intensity equal to or less than 0.25. (B) XRD data obtained from elutriated samples of the host bed (blue), sand dike (orange), and source bed (fuchsia). The peak differences in A were not reproduced in these data. The tan area highlights the wide arc associated with clay minerals; note that the arc is more pronounced in the host material, and may represent a larger amount of clay minerals in the host material. The 26.7° quartz peak has a relative intensity ($I/I_0$) of 1; all other peaks have a relative intensity less than 0.5.

did the source bed and sand dike data overlay one another, although the host material does maintain higher overall peak intensities than the other two sediments (Fig. 3-8B). The wide, round arc in the baseline centered around $2\theta = 23°$ (highlighted by the tan area in Fig. 3-8B) provides some insight into the differences between these sediments: the height of this arc above background levels is much greater in the host material than in the other two sediments. The arc in the sand dike data is the least pronounced. This arc is associated with poorly crystallized minerals or amorphous material (e.g., a gel), which may include clay minerals, and a larger amplitude arc indicates a larger proportion of these minerals (Moore and Reynolds, 1997; Bonnard et al., 2012). This may indicate that there are more clay minerals in the host material, and that the difference between the arcs in the source and sand dike sediments may indicate that the clay proportion is less in the sand dike than in the source material. The earthquake that produced these sand dikes may have been strong enough to liquefy and vent only the most clay-poor areas of sediment, which are now found in the dikes. The areas that contained slightly more clay might not have been fully liquefied and vented, and were left behind in the source bed.

## Summary

The numerous, liquefaction-induced paleoseismic features found at sites south-southwest of Lyerly, Georgia, indicate that one or more earthquakes with $M_w \geq 6$ have affected the area-. Possible sand blow cones have been identified on vintage aerial photos, and field investigations of some of these areas have identified high, light-colored spots that may represent sand dikes that fed decapitated sand blows. Approximately 1.5 km to the southwest, possible sand dikes were identified in a cut bank. Separately, these features may be explained by other processes, such as

redoximorphic conditions (e.g., Vepraskas, 1994), but together they provide a good argument for the existence of large, prehistoric earthquakes.

Much of the work done at these sites for this thesis is preliminary; more work is needed to further investigate these features. Future work should include shallow seismic reflection surveys and trenching of the high, light-colored spots on Taylor Farm. The sand dikes site should be cleared of vegetation and excavated to reveal the possible continuation of the dikes. Identification of a preserved sand blow cone above the dikes would provide substantial evidence of paleoseismic activity in the area.

## *CHAPTER IV*

## *IMPLICATIONS FOR THE ETSZ AND FUTURE WORK*

The two largest earthquakes recorded in the ETSZ were both $M_w = 4.6$: one in 1976 near Alcoa, TN, and the other in 2003 near Ft. Payne, AL (Fig. 1-1A). The frequency-magnitude relationship for the ETSZ, compared with other active seismic zones in the eastern US, indicates the ETSZ is second only to the New Madrid seismic zone in the number of earthquakes produced per year (Fig. 4-1) (Hatcher et al., 2012). Extrapolation of the curve past the largest recorded earthquakes indicates that the ETSZ may be capable of producing a $M \approx 5$ earthquake every ~100 years and a $M \approx 6$ earthquake every ~1,000 years per 25,000 $km^2$. A $M_w \geq 6$ earthquake is sufficient to produce liquefaction features (Obermeier, 2009), so it is probable that these features may be found in the ETSZ. Shaking from large earthquakes in the ETSZ was obviously strong enough to produce coseismic surface faulting. These faults have recorded up to 1 m of displacement, which can be empirically related to one or more $M_w > 6.5$ earthquakes (Fig. 1-4) (Wells and Coppersmith, 1994).

### Implications from Site DL-6 near Dandridge, Tennessee

Prior to this study, Hatcher et al. (2012) indicated that deformation at site DL-6 provided evidence of at least two strong earthquakes since 112-103 ka. Crosscutting relationships in the boat-shaped structure with soil development indicate that there has been at least one strong earthquake ($M_w \geq 6$) several thousands to a few tens of thousands of years ago (Hatcher et al., 2012), the range of which is within the timeframe of the fissure-forming event, occurring

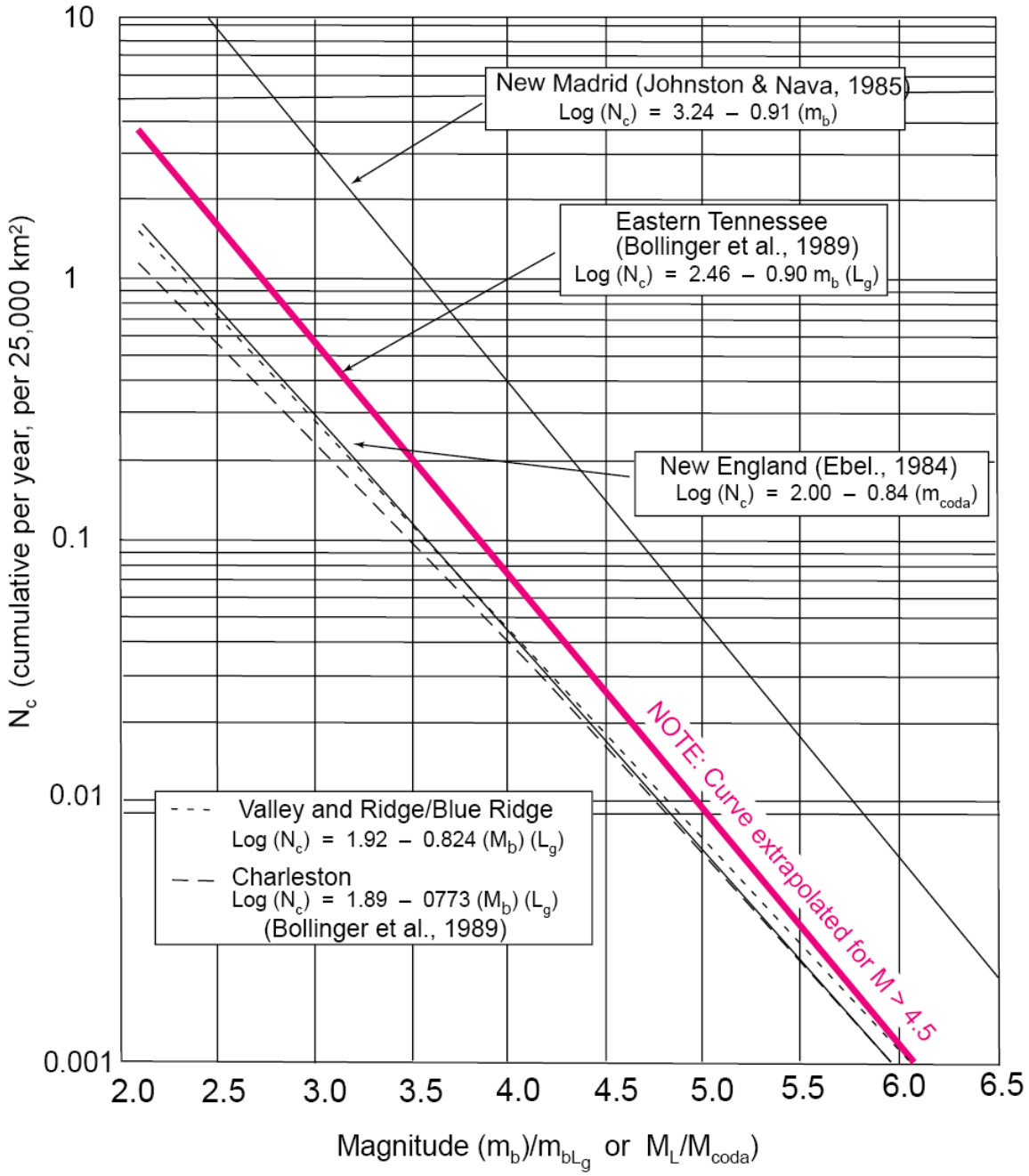


**Figure 4-1.** Frequency versus magnitude plot for the ETSZ, New Madrid seismic zone, Valley and Ridge/Blue Ridge seismic zone, and Charleston seismic zones. Note that the curve for the ETSZ is extrapolated for earthquakes >M = 4.5. $m_b$—body wave magnitude; $m_b(L_g)$—body wave magnitude scaled to $L_g$ wave; $m_{coda}$—magnitude derived from duration or coda length; $(M_b)(L_g)$—local or regional magnitude calibrated for earthquakes east of the Rocky Mountains. (From Hatcher et al., 2012)

between 17,600 and 13,705 years ago. While the timeframes of soil development over the boat-shaped structure and OSL ages of the fissure-filling sediment overlap, it is still possible that these features could represent two separate events, as the range is several thousands of years and several M ≥ 6 earthquakes could occur in the seismic zone during that timespan. It is also possible that fracturing over the boat-shaped structure is due to shrinkage or downslope movement of sediment.

A timeline of events at sites DL-6 and DL-9 can be formed from the data collected for this thesis and by Hatcher et al. (2012) (Figure 4-2). The event that formed the strike-slip fault occurred more recently than the fissure-forming event, but prior to the event that produced the listric thrust fault in Trench 2, because this fault truncates the strike-slip fault. The 10-cm displacement on the strike-slip fault indicates that the associated earthquake is estimated to have been $M_w \geq 6$, using the empirical relation between maximum displacement and magnitude derived by Wells and Coppersmith (1994). The later earthquake forming the listric thrust fault with ~1 m of offset is estimated to have been $M_w \geq 6.5$, using the same relationship. It should be noted that these crosscutting relationships only provide relative ages for these features, and the time in between these events could range from minutes to centuries. The 4,890 ± 700 y age of the fissure-filling sediments may postdate another more recent earthquake, although an earthquake-related cause is not certain. Overall, the paleoseismic data at site DL-6 provide evidence for 4 to 6 Mw ≥ 6 paleoearthquakes in the past 112 ka, with at least 3 large paleoearthquakes in the last 17,600 y (Figure 4-2).

***Implications from faults and fracture arrays in Sevier Shale saprolite***

The azimuths of gently dipping fault surfaces and slickenlines in Sevier Shale saprolite at

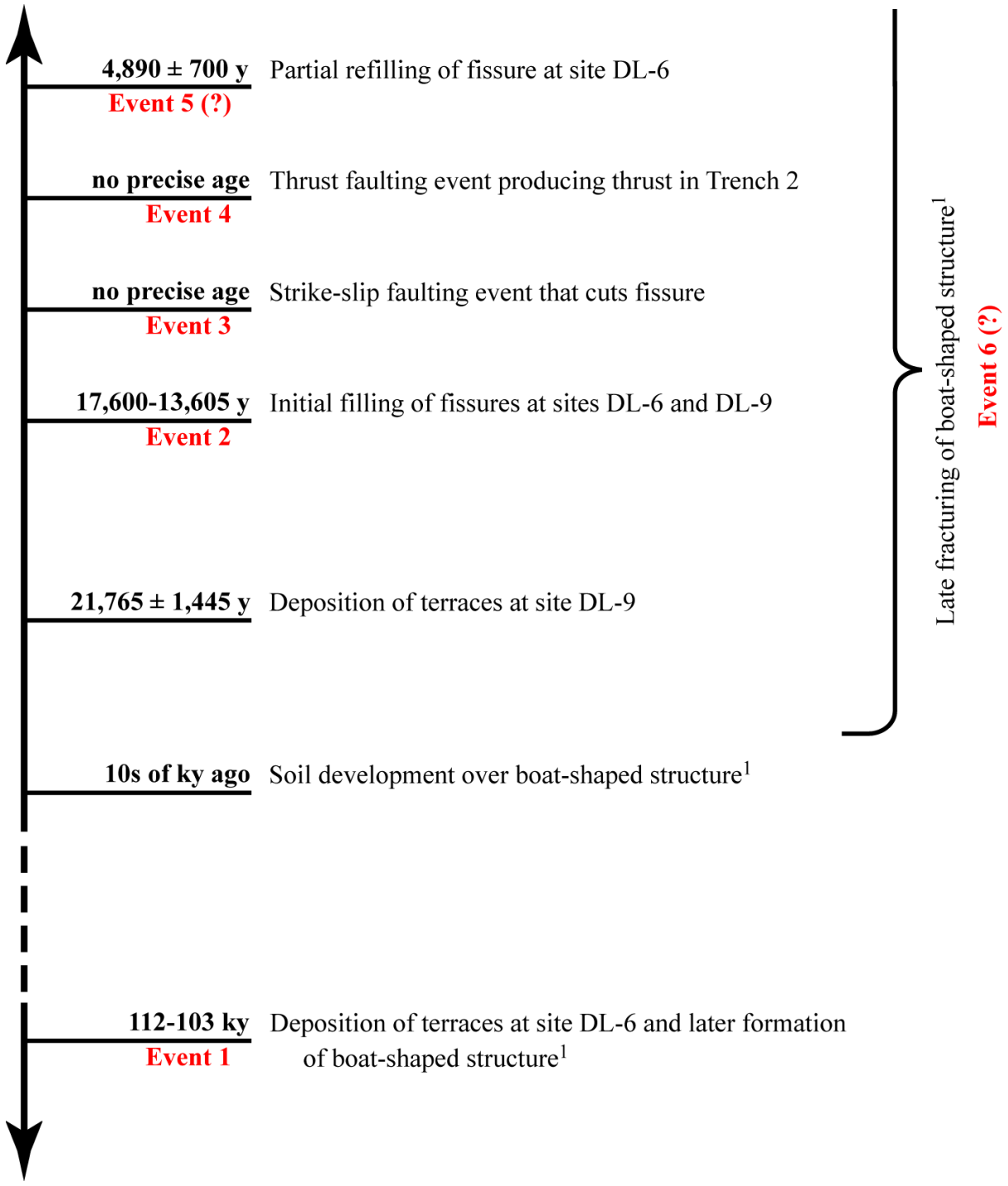


**Figure 4-2.** Timeline of events at sites DL-6 and DL-9 near Dandridge, Tennessee, with the most recent event on the top. Ages given were obtained by OSL dating of sediments (Table 2-1). Earthquake events are numbered in red. Events 3 and 4 have no OSL age and are assigned based on crosscutting relationships. Events 5 and 6 are probable earthquakes that may have non-seismic causes. Dashed line indicates break in timeline. [1]Data from Hatcher, et al., 2012.

site DL-6 nearly overlap each other: fault surfaces strike between N55°E and N70°E, and 57 percent of slickenlines trend between N50°E and N70°E and verge generally west-southwest (Fig. 2-12). Fault-surface azimuths in the shale are colinear with slickenline azimuths, indicating slip on these surfaces is roughly parallel to strike. The regional stress field of the ETSZ is oriented with the maximum principal stress ($\sigma_1$) at N70°E (Zoback and Zoback, 1991), which is subparallel with the majority of measured slickenlines in Sevier Shale saprolite; however, slickenlines on the main thrust fault in Quaternary sediment trend N62°W and plunge 28° SE, which is notably different from that of slickenlines in the shale as well as the orientation of regional maximum principal stress. Thrust fault-surface azimuths in shale saprolite are not likely related to $\sigma_1$, because they probably utilize some preexisting surfaces in the shale, although these surfaces are obviously favorably oriented for activation as fault surfaces under lower stress than is required to form new fault surfaces in Sevier Shale saprolite.

The thrust fault in Trench 2 continues as one fault to the northeast of the trench through Quaternary terrace alluvium, yet to the southwest the fault splays into Sevier Shale saprolite (Plate 1, Fig. 2-11). Terrace alluvium and bedrock saprolite are obviously two very different media with different physical properties. Terrace alluvium is mostly unconsolidated, cohesionless sediment with soil development in the upper portions, whereas Sevier Shale saprolite is cohesive with bedding planes forming weak surfaces. Sevier Shale represents turbidite deposition in the Middle Ordovician Alleghanian-Taconian foreland basin (Shanmugam and Walker, 1983); turbidite deposits, which are fining-upward sequences separated by scour surfaces, create surfaces along which cohesion is minimal. These primary surfaces of weakness in Sevier Shale are overprinted by Paleozoic and younger fractures and are cut by numerous

joints, some of which may be shear fractures related to ETSZ faulting. In Quaternary alluvium, deformation was concentrated along one fault since the entire volume lacks cohesion. Faulting in Sevier Shale saprolite was likely facilitated by preexisting surfaces of weakness in the shale, which have little to no cohesive strength and require a lower level of stress to activate than is required to form a new fracture throughout the entire volume of shale. In some areas of the Sevier Shale, however, the fault curves away from these preexisting weak surfaces, indicating that stress at that point was high enough to form a new fracture, suggesting that orientations of preexisting surfaces are not fully compatible with the applied stress. A cross section through the map area shows these relationships (Fig. 4-3): at depth in the shale saprolite, deformation is concentrated along one fault that does not follow bedding surfaces, but there are several splays from the fault that extend upward from the fault and utilize bedding surfaces.

In Quaternary sediments, displacement along the fault verges northwest, whereas in Sevier Shale saprolite displacement verges west-southwest, indicating that material has an influence on direction of displacement. One hypothesis is that preexisting, near-vertical fractures in the shale, the majority of which trend N55-75°E and N40-50°W (discussed in detail later), facilitated extension along numerous fractures in the hanging wall. If the orientation of slickenlines along the fault in Quaternary alluvium represents the direction of maximum principal stress, preexisting fractures could displace shale east-northeast and west-southwest (Fig. 4-4). This would shorten the volume of shale parallel to the axis of maximum principal stress, and displace shale to the northeast and southwest via movement along preexisting fractures. This movement may be responsible for the difference in orientation of slickenlines in Sevier Shale saprolite and Quaternary alluvium. Slickenlines along the near-vertical fractures

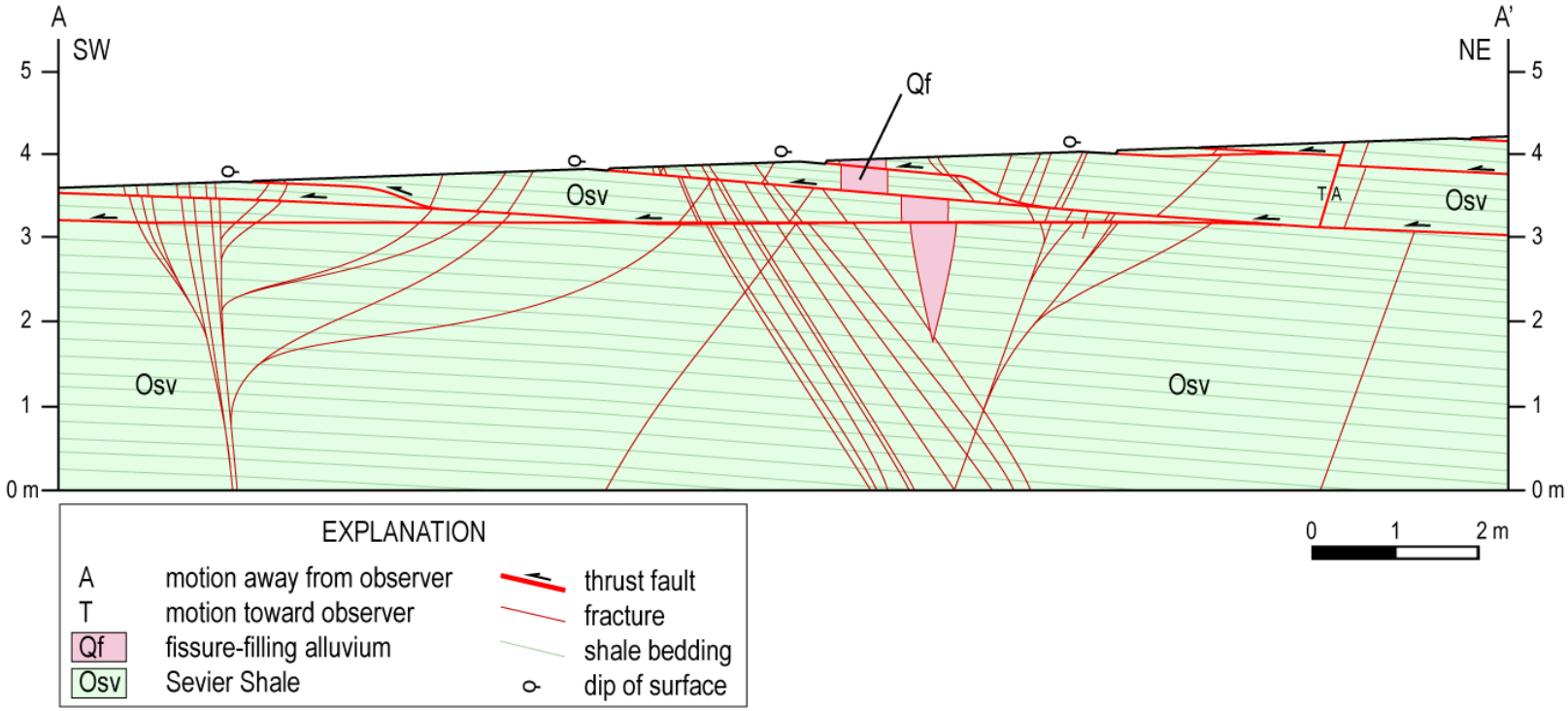


**Figure 4-3.** Cross section A-A' through map area at site DL-6 near Dandridge, Tennessee (location of cross section line on Fig. 2-7 and Plate 1). Note how the fault splays into several smaller faults with small displacements that utilize bedding surfaces in many places.

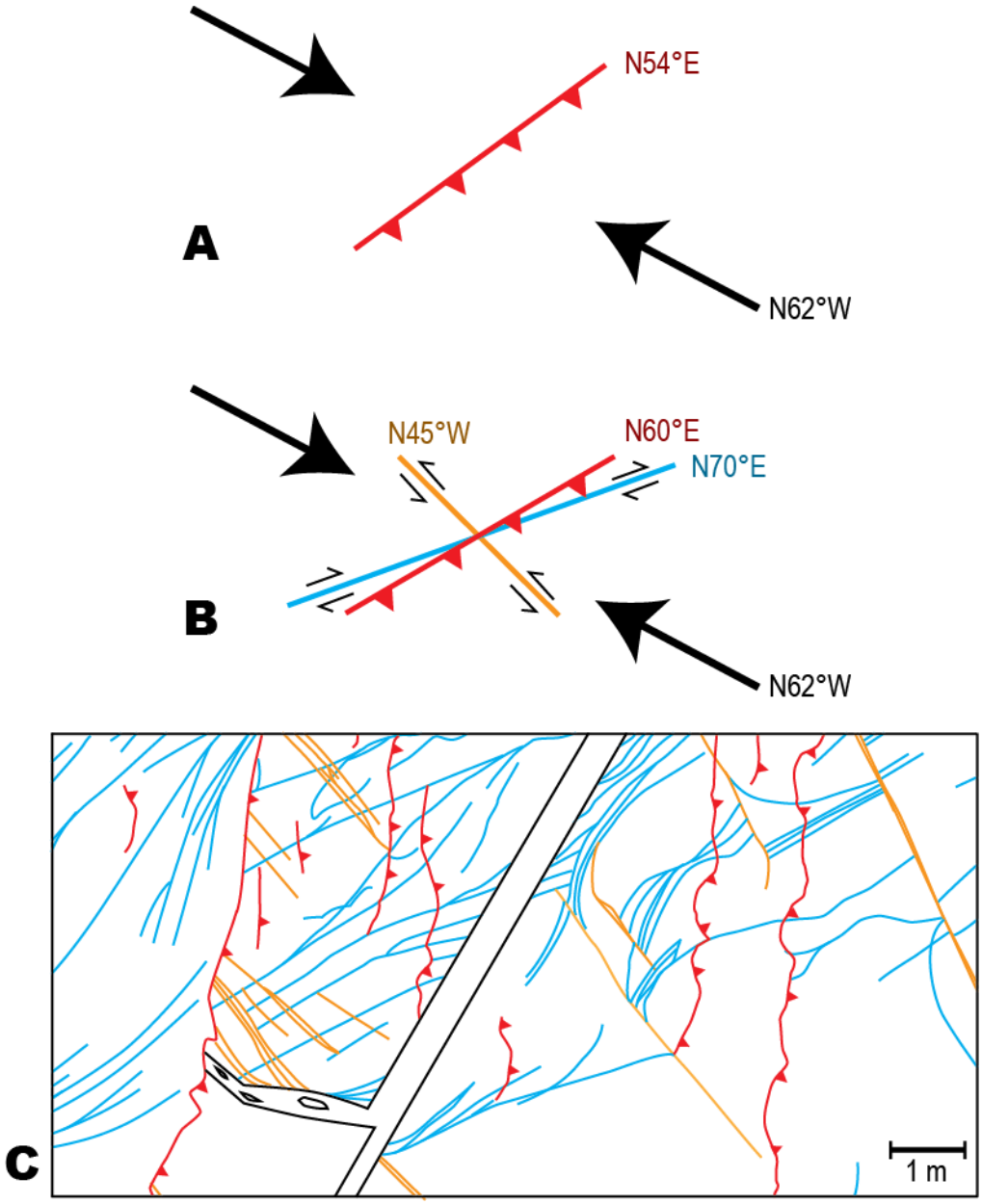


**Figure 4-4.** Extrusion of shale along preexisting fractures in Sevier Shale saprolite. (A) Orientation of fault generated in Quaternary terrace alluvium with arrows indicating direction of maximum principal stress derived from slickenlines on fault in alluvium. (B) General orientations of preexisting surfaces in Sevier Shale saprolite and their relative motions under the maximum principal stress from A. Red line—thrust faults in saprolite dipping ~20° southeast; blue line—near-vertical fractures trending northeast; orange line—near-vertical fractures trending northwest. (C) Portion of map from Plate 1 with northeast-trending fractures colored blue and northwest-trending fractures colored orange and thrust faults (with teeth on the hanging wall) colored red.

would help confirm this, but none were observed during mapping.

An alternative hypothesis is that motion along the fault was rotational. Slickenlines measured in the area suggest counterclockwise motion along the fault, since from east to west on the map slickenline azimuths rotate from west-northwest counterclockwise to southwest (Fig. 4-5). A larger, more dense population of slickenline measurements in both the shale saprolite and overlying alluvium may provide additional support for this hypothesis. It is possible that motion along this fault as recorded by the slickenlines is due to a combination of both hypotheses, and that there may be additional factors influencing motion on the fault that have not yet been observed in the field. Ground penetrating radar surveys of the area would provide additional insight into areas not trenched and may provide additional insight to motion along this fault.

Fracture azimuths in the saprolite are clustered into two populations centered around N55-75°E and N40-50°W (Fig. 2-12). These azimuths are not entirely coincident with those measured at other sites along Douglas Reservoir, the bulk of which trend N45°E, N65°E, N85°E, and N55°W at site DL-4 and N55°E, N25°W, and N55°W at site DL-5b (Hatcher et al., 2012). The differences in fracture azimuths between site DL-6 and other sites around Douglas Reservoir may be because the fractures measured at DL-6 occur in bedrock rather than sediment, and bedrock has preexisting surfaces of weakness that fractures and faults may utilize to distribute strain if they are suitably oriented. Unconsolidated terrace sediments may have preexisting surfaces of weakness that vary between sites, but these may not concentrate stress to the same extent that surfaces of weakness in solid rock would, because the sediment has a lower cohesive strength. Azimuths of bedrock fractures measured in shale and siltstone in the Blue Ridge Foothills near Pigeon Forge, Tennessee, and the Valley and Ridge near Oak Ridge, Tennessee,

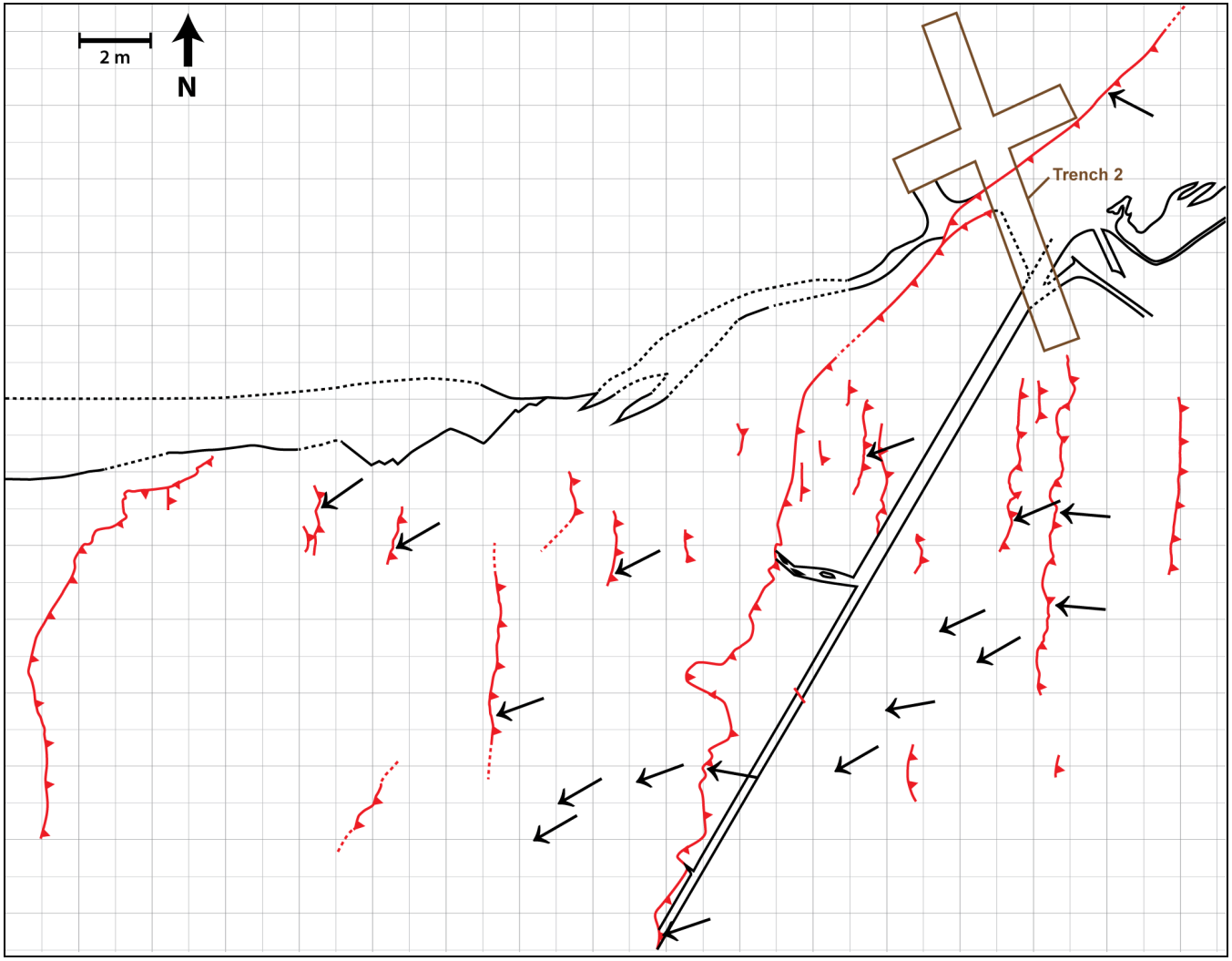


**Figure 4-5.** Slickenline orientations measured at site DL-6 (black arrows) enlarged to demonstrate trends throughout the map area. Note that from east to west, there is a counterclockwise rotation from west-northwest to southwest. Red lines are thrust faults (with teeth on the hanging wall).

contain populations of fractures with azimuths centered at N55-75°E, N80°W, and N45°W (Hatcher et al., 2012). The near-vertical fractures at site DL-6 are likely preexisting Paleozoic fractures based on matching orientations of measured fracture populations at site DL-6 and those measured in the Blue Ridge Foothills and Valley and Ridge, although they are suitably oriented for reactivation as faults in the current stress regime. Reactivation of these fractures as faults would likely be strike-slip, since most of the fractures have near-vertical dips.

Features in Sevier Shale saprolite at site DL-6 indicate that faulting and most fracturing here is related to activation of favorably oriented surfaces in bedrock at lower stress than required to form new fractures. While slickenlines in Sevier Shale saprolite indicate displacement nearly parallel to strike with west-southwest vergence, there is still a component of dip slip motion, as seen the thrust fault in Trench 2 (Fig. 1-9). This thrust displays bedding-parallel slip in the shale and curves steeply upward (listric) across bedding with northwest vergence where it crosscuts the sandy terrace alluvium, placing Ordovician Sevier Shale saprolite above Quaternary alluvium. The contrast in vergence throughout the site may be due to heterogeneous extrusion of shale along preexisting fractures (Fig. 4-4) along with counterclockwise rotational motion along the fault (Fig. 4-5). Paleozoic fractures in the Sevier Shale are abundant and intricately related to traceable faults at site DL-6, and newer fractures appear to be concentrated near and splay from faults and sediment-filled fissures (Plate 1). Fault splays appear to merge with preexisting fractures and sediment-filled fissures in some places and truncate against these fractures in others. Reactivation of fractures likely produces strike-slip displacement with minor (if any) dip-slip displacement due to near vertical dip on most fractures.

**Implications from Sites near Lyerly, Georgia**

While the reconnaissance in this area was mostly preliminary, liquefaction features discovered at these sites are far too numerous to be explained by other processes. A variety of probable liquefaction features were identified, including: sand dikes in a cut bank; possible sand blow cones on aerial photographs; and decapitated feeder dikes to sand blow cones. For liquefied sediments to build enough pressure to hydraulically fracture overlying sediments and form sand dikes and sand blow cones, a $M_w \geq 6$ earthquake is required (Obermeier, 2009). The presence of these liquefaction features requires at least one prehistoric $M_w \geq 6$ earthquake to have affected the area. Paleoliquefaction evidence for multiple earthquakes in this area would require either crosscutting relationships and/or precise age dating of the liquefied sediments and their host materials. Further work in this area may yield these data.

It is unlikely that these liquefaction features are the results of far-field earthquakes sourced in the New Madrid or Charleston seismic zones. Johnston and Schweig (1996) reported that effects felt at a radius of 500 km away (approximate distance between New Madrid and ETSZ) from the 1811-1812 New Madrid earthquakes were rated Modified Mercalli Intensity (MMI) VI. Earthquakes with MMI VI generally have moment magnitudes in the range of $M_w$ = 5.0-5.9 (United States Geological Survey). Attenuation of a $M_w = 8$ earthquake sourced in the New Madrid seismic zone is too great to induce liquefaction by the time it reaches the ETSZ. The Charleston seismic zone is ~500 km from the ETSZ, so it would also be expected that attenuation would be too great for earthquakes sourced in the Charleston seismic zone to induce liquefaction in the ETSZ.

The greatest revelation from reconnaissance in this area is that liquefaction features

related to the ETSZ are numerous, even if they are initially difficult to identify. While the most obvious features may have been obliterated (e.g., sand blow cones), their feeder dikes still remain. These dikes may be below the resolution of aerial photography, but sites that may have once had sand blow cones are appropriate candidates to find decapitated feeder dikes. XRD analyses can help to identify slight differences in the mineralogy of these sediments, although they do not tell the complete story: future analyses should quantify the amount of organic matter present in sediments to better understand the organic content.

Future work should also include shallow seismic reflection surveys, ground penetrating radar surveys, and resistivity studies (e.g., Obermeier et al., 2005) in addition to trenching; these methods will provide a better understanding of the three-dimensional structure, stratigraphy, and continuity of Quaternary deposits. Trenching may also provide additional opportunities to collect samples for OSL dating and possibly radiocarbon dating to better delimit the ages of the terraces and paleoseismic features therein.

### Identification of New Sites in the ETSZ

Aerial photographs have revealed additional areas of tonal anomalies in central East Tennessee (Fig. 4-6). The terraces containing these tonal anomalies lie along the Tennessee River and Little Tennessee River, and have since been inundated by Watts Bar and Tellico Reservoirs, respectively. This area is nearer the locus of highest earthquake density than the field sites described in this thesis (Fig. 1-1B). New methods will be required to further investigate these terraces, because all remain under water throughout the year. New methods should include high-resolution “marine” seismic reflection surveys over the inundated floodplains of these

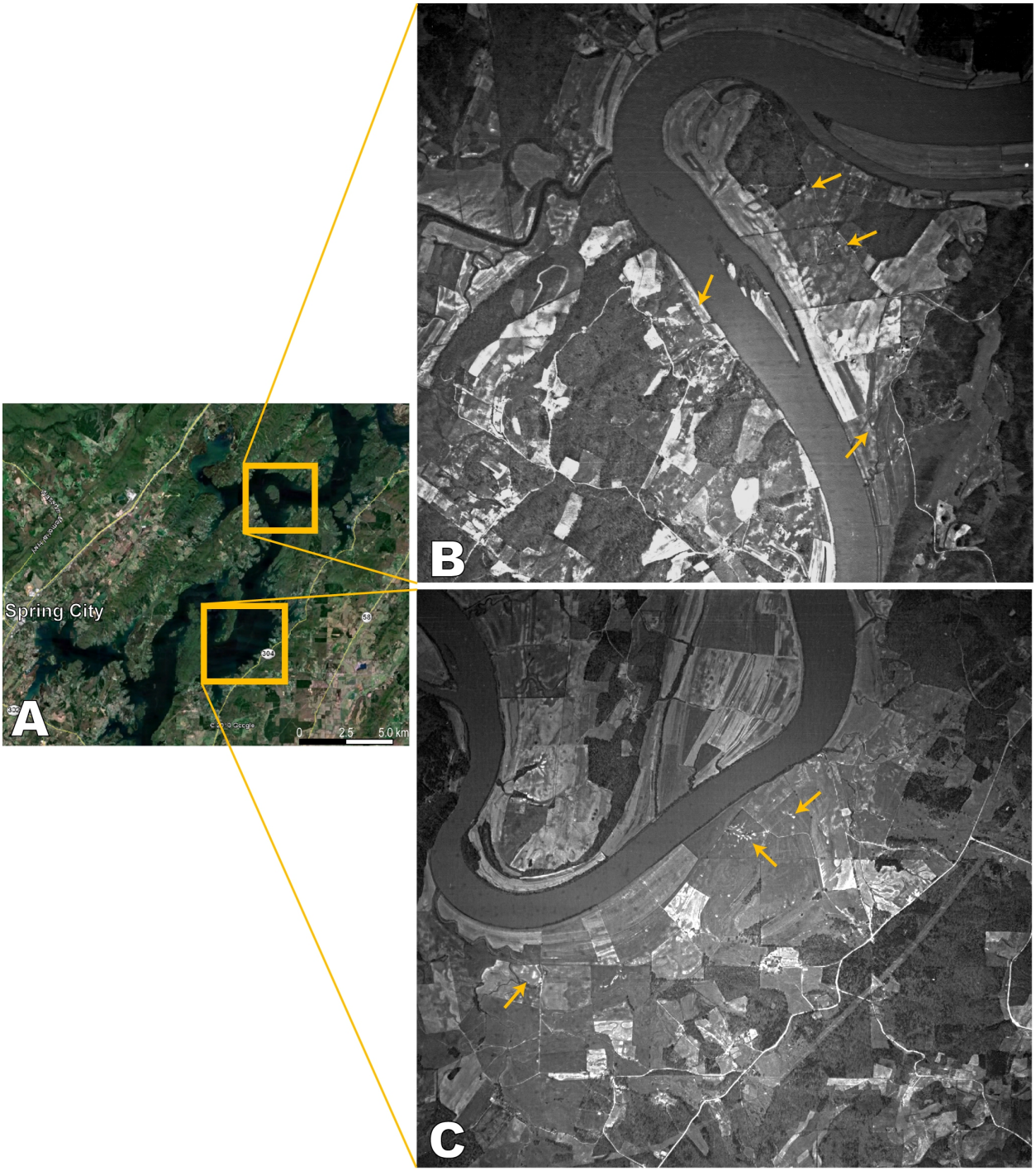


**Figure 4-6.** (A) Present-day Watts Bar Reservoir near Spring City, Tennessee, 80 km southwest of Knoxville, Tennessee. Image from Google Earth. (B) Pre-impoundment 1938 TVA aerial photograph of a meander along the Tennessee River with arrows pointing to areas containing tonal anomalies along the floodplain. (C) 1938 TVA aerial photograph of another meander along the Tennessee River south of that in B with arrows pointing to some areas on the floodplain containing tonal anomalies. Note that the areas of tonal anomalies are all currently inundated by Watts Bar Reservoir in A.

reservoirs, such as those performed by Guo et al. (2011) along the Mississippi River. This study resolved liquefied sediments and faulted strata on the bottom of the Mississippi River channel. Additionally, field reconnaissance along nearby rivers and tributaries of Watts Bar and Tellico Reservoirs should provide some useful data.

## *CHAPTER V*

## *CONCLUSIONS*

**1)** X-ray diffraction analysis of shale chips collected at site DL-5 near Dandridge, Tennessee, indicates that chips have the same mineralogy as underlying Sevier Shale. Matching mineralogy supports the hypothesis that chips boiled up through Quaternary sediments during an earthquake.

**2)** The fissure at site DL-6 near Dandridge, Tennessee, was filled around 15,450 ± 1,745 y, and partially refilled around 4,890 ± 700 y, both of which may be related to seismic events in the ETSZ; it is also possible that these ages are associated with other processes, like erosion and redeposition by floods. A similar fissure at site DL-9 was filled around 15,865 ± 1,735 y, which indicates that the total range of initial filling for both fissures was 13,705 to 17,600 y.

**3)** A large proportion of slickenline (57 percent verge N50-70°E) and fracture (55 percent trend N50-80°E) azimuths measured at site DL-6, southwest of Dandridge, Tennessee, are nearly parallel to the current maximum compressive stress ($\sigma_1$ = N70°E [Zoback and Zoback, 1991]) of the region. However, the orientations of slickenlines vary systematically throughout the map area and may reflect counterclockwise-rotational motion along the fault. Near-vertical fractures are suitable for reactivation with dominantly strike-slip motion and may have facilitated extension perpendicular to the axis of maximum applied stress in the Sevier Shale saprolite. Thrust faults in the area are the result of activation of surfaces striking ~N65°E and dipping less than 20° to the south, with motion near-parallel to strike, although thrust faults do vary from this orientation where applied stress exceeded the rock strength.

**4)** Crosscutting relationships of fractures and faults mapped for this thesis at site DL-6 near Dandridge, Tennessee, indicate a history of at least 3-4 strong earthquakes affecting the area in the last 17,600 y. The thrust fault exposed in Trench 2 continues northeast through Quaternary sediment as one traceable fault; to the southwest, the fault splays into several faults as it continues into Sevier Shale saprolite. The fissure is truncated by this fault, indicating that it formed during a separate, earlier compressional event. A small strike-slip fault that displaces the fissure is truncated by this thrust fault, indicating another compressional event occurred between the fissure-forming event and thrust fault-forming event. The timeframes of the fissure-forming event (15,450 ± 1,745 y) and fractured soil development overprinting the boat-shaped structure (several to tens of thousands of years ago [Hatcher et al., 2012]) overlap and may represent one or separate paleoearthquakes. The younger filling of parts of the fissure (4,890 ± 700 y) may represent another paleoearthquake.

**5)** Sand dikes in a cut bank along the Chattooga River near Lyerly, Georgia, provide additional evidence of liquefaction-inducing prehistoric earthquakes in the ETSZ. Grain-size and X-ray diffraction analysis of sediments suggest that the cap sediments are finer grained and more clay-rich than are source bed or sand dike sediments. Possible decapitated sand blow feeder dikes exposed in a nearby field also support the existence of prehistoric liquefaction-inducing earthquakes in the ETSZ, although more work is needed to confirm this possibility.

**6)** The data presented here support the occurrence of large ($M_w > 6$), prehistoric earthquakes in the ETSZ. These data fortify the need to readdress seismic risk estimates in East Tennessee, which contains several large population centers and vital infrastructures (highways, railroads, etc.) that, if damaged, would have widespread effects. A $M_w > 6$ earthquake would cause

damage that would affect people in the ETSZ for weeks to months, including: structural damage to houses and buildings, collapse of areally extensive buildings (e.g., warehouses and grocery stores), damage to highways and railroads, damage to older dams and bridges, damage to underground storage tanks and related contamination of aquifers, and increased landslide risk (especially during a wet season). Structural engineers in the ETSZ should include seismic loading in their design analysis, as a large earthquake could occur during a structure's lifetime. It is important that people living in the ETSZ be prepared for a large earthquake, and increasing seismic risk estimates would communicate the increased danger to the public.

## *REFERENCES CITED*

Allmendinger, R.W., Cardozo, N., and Fisher, D., 2012, Structural geology algorithms: Vectors and tensors: Cambridge, United Kingdom, Cambridge University Press, 289 p.

Bartholomew, M.J., and Hatcher, R.D., Jr., 2010, The Grenville orogenic cycle of southern Laurentia: Unraveling sutures, rifts, and shear zones as potential piercing points for Amazonia: Journal of South American Earth Sciences, v. 29, p. 4-20.

Bartholomew, M.J., and Van Arsdale, R.B., 2012, Structural controls on intraplate earthquakes in the eastern United States, *in* Cox, R.T., Boyd, O.L., and Locat, J., eds., Recent advances in North American paleoseismology and neotectonics east of the Rockies: Boulder, Colorado, Geological Society of America Special Paper 493, p. 165-189.

Bezerra, F.H.R., do Nascimento, A.F., Ferreira, J.M., Nogueira, F.C., Fuck, R.A., Brito Neves, B.B., and Sousa, M.O.L., 2011, Review of active faults in the Borborema Province, Intraplate South America—Integration of seismological and paleoseismological data: Tectonophysics, v. 510, p. 269-290.

Biasi, G.P., and Weldon, R.J., 2006, Estimating surface rupture length and magnitude of paleoearthquakes from point measurements of rupture displacement: Bulletin of the Seismological Society of America, v. 96, p. 1612-1623.

Bollinger, G.A., Chapman, M.C., and Sibol, M.S., 1993, A comparison of earthquake damage areas as a function of magnitude across the United States: Bulletin of the Seismological Society of America, v. 83, p. 1064-1080.

Bollinger, G.A., Davison, F.C., Sibol, M.S., and Birch, J.B., 1989, Magnitude recurrence relations for the southeastern United-States and its subdivisions: Journal of Geophysical Research-Solid Earth and Planets, v. 94, p. 2857-2873.

Bonnard, P., Basile-Doelsch, I., Balesdent, J., Masion, A., Borschneck, D., and Arrouays, D., 2012, Organic matter content and features related to associated mineral fractions in an acid, loamy soil: European Journal of Soil Science, v. 63, p. 625-636.

Carpenter, N.S., Payne, S.J., and Schafer, A.L., 2012, Toward reconciling magnitude discrepancies estimated from paleoearthquake data: Seismological Research Letters, v. 83, p. 555-565.

Chapman, J., 1977, Archaic Period research in the lower Little Tennessee River valley; 1975: University of Tennessee, Department of Anthropology Report of Investigations 18, 206 p.

Chapman, M.C., Powell, C.A., Vlahovic, G., and Sibol, M.S., 1997, A statistical analysis of earthquake focal mechanisms and epicenter locations in the eastern Tennessee seismic zone: Bulletin of the Seismological Society of America, v. 87, p. 1522-1536.

Counts, R.C., and Obermeier, S.F., 2012, Seismic signatures: Small-scale features and ground-fractures, *in* Cox, R.T., Boyd, O.L., and Locat, J., eds., Recent advances in North American paleoseismology and neotectonics east of the Rockies: Boulder, Colorado, Geological Society of America Special Paper 493, p. 203-219.

Cox, R.T., Hill, A.A., Larsen, D., Holzer, T., Fonnan, S.L., Noce, T., Gardner, C., and Morat, J., 2007, Seismotectonic implications of sand blows in the southern Mississippi Embayment: Engineering Geology, v. 89, p. 278-299.

Dentith, M., O'Neill, A., and Clark, D., 2010, Ground penetrating radar as a means of studying palaeofault scarps in a deeply weathered terrain, southwestern Western Australia: Journal of Applied Geophysics, v. 72, p. 92-101.

Dunn, M.M., and Chapman, M.C., 2006, Fault orientation in the eastern Tennessee seismic zone:

A study using the double-difference earthquake location algorithm: Seismological Research Letters, v. 77, p. 494-504.

Ebel, J.E., 1984, Statistical aspects of New-England seismicity from 1975 to 1982 and implications for past and future earthquake activity: Bulletin of the Seismological Society of America, v. 74, p. 1311-1329.

Fetter, C.W., 2001, Applied Hydrogeology: Upper Saddle River, New Jersey, Prentice Hall, 598 p.

Galbraith, R.F., Roberts, R.G., Laslett, G.M., Yoshida, H., and Olley, J.M., 1999, Optical dating of single and multiple grains of quartz from Jinmium rock shelter, northern Australia: Archaeometry, v. 41, p. 339-364.

Gosse, J.C., and Phillips, F.M., 2001, Terrestrial *in situ* cosmogenic nuclides: theory and application: Quaternary Science Reviews, v. 20, p. 1475-1560.

Grollimund, B., and Zoback, M.D., 2001, Did deglaciation trigger intraplate seismicity in the New Madrid seismic zone?: Geology, v. 29, p. 175-178.

Guccione, M.J., 2005, Late Pleistocene and Holocene paleoseismology of an intraplate seismic zone in a large alluvial valley, the New Madrid seismic zone, Central USA: Tectonophysics, v. 408, p. 237-264.

Guo, L., Magnani, M.B., McIntosh, K.D., Waldron, B., Meyer, D., 2011, Preliminary interpretation of the major fault zones responsible for the earthquakes that triggered sand liquefaction in southern Mississippi embayment Central US from high-resolution marine seismic reflection data: presented at 2011 Fall Meeting, AGU, San Francisco, Calif., 5-9 Dec.

Gutierrez, F., Masana, E., Gonzalez, A., Lucha, P., Guerrero, J., and McCalpin, J.P., 2009, Late

Quaternary paleoseismic evidence on the Munbrega half-graben fault (Iberian Range, Spain): International Journal of Earth Sciences, v. 98, p. 1691-1703.

Hardeman, W.D., Miller, R.A., and Swingle, G.D., 1966, Geologic map of Tennessee, East Sheet: Tennessee Division of Geology, State Geologic Map, Scale 1:250,000.

Hatcher, R.D., Jr., and Bridge, J., 1973, Geologic Map of the Jefferson City Quadrangle, Tennessee: Tennessee Division of Geology Geologic Map GM-163-SW, Scale 1:24,000.

Hatcher, R.D., Jr., Bream, B.R., and Merschat, A.J., 2007a, Tectonic map of the southern and central Appalachians: A tale of three orogens and a complete Wilson cycle, *in* Hatcher, R.D., Jr., Carlson, M.P., McBride, J.H., and Martinez-Catalan, J.R., eds., 4-D Framework of Continental Crust: Boulder, Colorado, Geological Society of America Memoir 200, p. 1-38.

Hatcher, R.D., Jr., Lemiszki, P.J., and Whisner, J.B., 2007b, Boundaries and internal deformation in the curved southern Appalachian foreland fold-thrust belt, *in* Sears, J.W., Harms, T., and Evenchick, C., eds., Whence the mountains? Inquiries into the evolution of orogenic systems: A volume in honor of Raymond A. Price: Boulder, Colorado, Geological Society of America Special Paper 433, p. 243-276.

Hatcher, R.D., Jr., Vaughn, J.D., and Obermeier, S.F., 2011, Large earthquake paleoseismology in the East Tennessee seismic zone: Results of an 18-month pilot study: First year annual report to the Nuclear Regulatory Commission.

Hatcher, R.D., Jr., Vaughn, J.D., and Obermeier, S.F., 2012, Large earthquake paleoseismology in the East Tennessee seismic zone: Results of an 18-month pilot study, *in* Cox, R.T., Boyd, O.L., and Locat, J., eds., Recent advances in North American paleoseismology and

neotectonics east of the Rockies: Boulder, Colorado, Geological Society of America Special Paper 493, p. 111-142.

Hemphill-Haley, M.A., and Weldon, R.J., 1999, Estimating prehistoric earthquake magnitude from point measurements of surface rupture: Bulletin of the Seismological Society of America, v. 89, p. 1264-1279.

Hough, S.E., and Page, M., 2011, Toward a consistent model for strain accrual and release for the New Madrid seismic zone, central United States: Journal of Geophysical Research-Solid Earth, v. 116, doi:10.1029/2010JB007783.

Ishihara, K., 1985, Stability of natural soil deposits during earthquakes: Proceedings of the 11th International Conference on Soil Mechanics and Foundation Engineering, San Francisco, California, v. 1, p. 321-376.

Jacoby, G.C., 1997, Application of tree ring analysis to paleoseismology: Reviews of Geophysics, v. 35, p. 109-124.

Johnston, A.C., and Nava, S.J., 1985, Recurrence rates and probability estimates for the New Madrid seismic zone: Journal of Geophysical Research-Solid Earth and Planets, v. 90, p. 6737-6753.

Johnston, A.C., and Schweig, E.S., 1996, The enigma of the New Madrid earthquakes of 1811-1812: Annual Review of Earth and Planetary Sciences, v. 24, p. 339-384.

Kelson, K.I., Simpson, G.D., VanArsdale, R.B., Haraden, C.C., and Lettis, W.R., 1996, Multiple late Holocene earthquakes along the Reelfoot fault, central New Madrid seismic zone: Journal of Geophysical Research-Solid Earth, v. 101, p. 6151-6170.

King, E.R., and Zietz, I., 1978, New-York Alabama lineament—Geophysical evidence for a

major crustal break in basement beneath Appalachian basin: Geology, v. 6, p. 312-318.

Lawton, D.E., and others, 1976, Geologic Map of Georgia: Georgia Geological Survey, scale 1:500,000.

Lienkaemper, J.J., Dawson, T.E., Personius, S.F., Seitz, G.G., Reidy, L.M., and Schwartz, D.P., 2002, A record of large earthquakes on the southern Hayward fault for the past 500 years: Bulletin of the Seismological Society of America, v. 92, p. 2637-2658.

Liu, M., Stein, S., and Wang, H., 2011, 2000 years of migrating earthquakes in North China: How earthquakes in midcontinents differ from those at plate boundaries: Lithosphere, v. 3, p. 128-132.

McCalpin, J., and Nelson, A., 2009, Introduction to paleoseismology, Ch. 1, *in* McCalpin, J.P., ed., Paleoseismology, 2nd ed.: Burlington, Massachusetts, Academic Press, p. 1-27.

Mills, H.H., and Delcourt, P.A., 1991, Quaternary geology of the Appalachian Highlands and Interior Low Plateaus, *in* Morrison, R.B., ed., Quaternary non-glacial geology; Conterminous U.S.: Boulder, Colorado, Geological Society of America, The Geology of North America, v. K-2, p. 611-628.

Moore, D.M., and Reynolds, R.C., Jr., 1997, X-Ray Diffraction and the Identification and Analysis of Clay Minerals: New York City, New York, Oxford University Press, 378 p.

Murray, A. S., and Wintle, A. G., 2003, The single aliquot regenerative dose protocol: potential for improvements in reliability: Radiation Measurements, v. 37, p. 377-381.

Nesse, W.D., 2000, Introduction to Mineralogy: New York City, New York, Oxford University Press, 442 p.

Obermeier, S.F., 2009, Using liquefaction-induced and other soft-sediment features for

paleoseismic analysis, Ch. 7, *in* McCalpin, J.P., ed., Paleoseismology, 2nd ed.: Burlington, Massachusetts, Academic Press, p. 497-564.

Obermeier, S.F., Olson, S.M., and Green, R.A., 2005, Field occurrences of liquefaction-induced features: A primer for engineering geologic analysis of paleoseismic shaking: Engineering Geology, v. 76, p. 209-234.

Ortuno, M., Masana, E., Garcia-Melendez, E., Martinez-Diaz, J., Stepancikova, P., Cunha, P.P., Sohbati, R., Canora, C., Buylaert, J.P., and Murray, A.S., 2012, An exceptionally long paleoseismic record of a slow-moving fault: The Alhama de Murcia fault (Eastern Betic shear zone, Spain): Geological Society of America Bulletin, v. 124, p. 1474-1494.

Post, J.L., 1984, Saponite from near Ballarat, California: Clays and Clay Minerals, v. 32, no. 2, p. 147-153.

Powell, C.A., and Chapman, M.C., 2012, The relationship between earthquake locations and velocity structure in the Eastern Tennessee seismic zone: Seismological Research Letters, v. 83, no. 2, p. 454.

Powell, C.A., Bollinger, G.A., Chapman, M.C., Sibol, M.S., Johnston, A.C., and Wheeler, R.L., 1994, A seismotectonic model for the 300-kilometer-long Eastern Tennessee seismic zone: Science, v. 264, p. 686-688.

Pratt, T.L., 2012, Kinematics of the New Madrid seismic zone, central United States, based on stepover models: Geology, v. 40, p. 371-374.

Pratt, T.L., Williams, R.A., Odum, J.K., and Stephenson, R.A., 2012, Origin of the Blytheville arch, and long-term displacement on the New Madrid seismic zone, Central U.S., *in* Cox, R.T., Boyd, O.L., and Locat, J., eds., Recent advances in North American

paleoseismology and neotectonics east of the Rockies: Boulder, Colorado, Geological Society of America Special Paper 493, p. 1-15.

Prescott, J.R., and Hutton, J.T., 1994, Cosmic ray contributions to dose rates for luminescence and ESR dating: large depths and long-term time variations: Radiation Measurements, v. 23, p. 497-500.

Seed, H.B., Idriss, I.M., and Arango, I., 1983, Evaluation of liquefaction potential using field performance data: Journal of Geotechnical Engineering, American Society of Civil Engineers, v. 109, p. 458-482.

Shanmugam, G., and Walker, K.R., 1983, Anatomy of the Middle Ordovician Sevier Shale basin, eastern Tennessee: Sedimentary Geology, v. 34, p. 315-337.

Steltenpohl, M.G., Zietz, I., Horton, J.W., Jr., and Daniels, D.L., 2010, New York-Alabama lineament: A buried right-slip fault bordering the Appalachians and mid-continent North America: Geology, v. 38, p. 571-574.

Talwani, P., and Cox, J., 1985, Paleoseismic evidence for recurrence of earthquakes near Charleston, South-Carolina: Science, v. 229, p. 379-381.

Tavakoli, B., Pezeshk, S., and Cox, R.T., 2010, Seismicity of the New Madrid seismic zone derived from a deep-seated strike-slip fault: Bulletin of the Seismological Society of America, v. 100, p. 1646-1658.

Tennessee Valley Authority, 2012, TVA: Douglas Reservoir, TVA Reservoirs and Power Plants: http://www.tva.com/sites/douglas.htm (accessed February, 2012).

Tsuchida, H., and Hayashi, S., 1971, Estimation of liquefaction potential of sandy soils: Proceedings of the 3rd Joint Meeting, US-Japan Panel on Wind and Seismic Effects,

UJNR, May 1971, p. 91-109.

United States Geological Survey, 2013, Magnitude/intensity comparison: http://earthquake.usgs.gov/learn/topics/mag_vs_int.php (Accessed July 16, 2013).

Vepraskas, M.J., 1994, Redoximorphic features for identifying aquic conditions: North Carolina Agricultural Research Service, Technical Bulletin 301, 33 p.

Vlahovic, G., Powell, C.A., Chapman, M.C., and Sibol, M.S., 1998, Joint hypocenter-velocity inversion for the eastern Tennessee seismic zone: Journal of Geophysical Research: Solid Earth, v. 103, p. 4879-4896.

Warrell, K.F., Cox, R.T., Hatcher, R.D., Jr., Counts, R.C., Vaughn, J.D., and Obermeier, S.F., 2012, Paleoseismic evidence for large, prehistoric earthquakes in the East Tennessee seismic zone: Geological Society of America Abstracts with Programs, v. 44, p. 291.

Wells, D.L., and Coppersmith, K.J., 1994, new empirical relationships among magnitude, rupture length, rupture width, rupture area, and surface displacement: Bulletin of the Seismological Society of America, v. 84, p. 974-1002.

Zoback, M.D., and Zoback, M.L., 1991, Tectonic stress field of North America and relative plate motions, *in* Slemmons, D.B., Engdahl, E.R., Zoback, M.D., and Blackwell, D.D., eds., Neotectonics of North America, Volume Geology of North America Decade Map Volume 1: Boulder, Colorado, Geological Society of America, p. 339-366.

# *APPENDIX*

Data measured at stations on the map in Plate 1 and Figure 2-11.

| Station | Latitude (°) | Longitude (°) | Feature | Strike | Dip | Trend | Plunge |
|---|---|---|---|---|---|---|---|
| 3/13 – 4 | 35.97345 | 83.44118 | clay surface | 62 | 19 | | |
| 3/13 – 5 | 35.97342 | 83.44117 | clay surface | 71 | 19 | | |
| 3/13 – 5a | 35.97342 | 83.44117 | fracture | 325 | | | |
| 3/13 – 5b | 35.97342 | 83.44117 | fracture | 150 | 84 | | |
| 3/13 – 8 | 35.97338 | 83.44120 | fracture | 315 | | | |
| 3/14 – 6 | 35.97342 | 83.44118 | clay surface | 65 | 16 | | |
| 3/14 – 8 | 35.97338 | 83.44118 | clay surface | 75 | 17 | | |
| 3/14 – 10 | 35.97334 | 83.44121 | clay surface | 70 | 19 | | |
| 3/14 – 11 | 35.97334 | 83.44121 | clay surface | 60 | 18 | | |
| 3/22 – 1 | 35.97341 | 83.44125 | clay surface | 55 | 16 | 290 | 12 |
| 3/22 – 1a | 35.97341 | 83.44125 | fracture | 70 | | | |
| 3/22 – 1b | 35.97341 | 83.44125 | fracture | 60 | | | |
| 3/22 – 1c | 35.97341 | 83.44125 | fracture | 310 | 76 | | |
| 3/22 – 1d | 35.97341 | 83.44125 | fracture | 310 | | | |
| 3/22 – 1e | 35.97341 | 83.44125 | fracture | 80 | | | |
| 3/22 – 1f | 35.97341 | 83.44125 | fracture | 65 | | | |
| 3/22 – 2 | 35.97340 | 83.44126 | oxide surface | 75 | 15 | 60 | 3 |
| 3/22 – 3 | 35.97336 | 83.44126 | oxide surface | 80 | 17 | 60 | 4 |
| 3/22 – 3a | 35.97336 | 83.44126 | fracture | 310 | | | 14 |
| 3/22 – 5 | 35.97338 | 83.44122 | oxide surface | 75 | 12 | 70 | 3 |
| 3/22 – 6a | 35.97340 | 83.44122 | fracture | 310 | 82 | | |
| 3/22 – 6b | 35.97340 | 83.44122 | fracture | 300 | | | |
| 3/22 – 6c | 35.97340 | 83.44122 | fracture | 295 | 89 | | |
| 3/22 – 6d | 35.97340 | 83.44122 | fracture | 300 | 80 | | |
| 3/22 – 7a | 35.97340 | 83.44121 | fracture | 330 | 85 | | |
| 3/22 – 7b | 35.97340 | 83.44121 | fracture | 135 | 82 | | |
| 3/22 – 7c | 35.97340 | 83.44121 | fracture | 150 | 85 | | |
| 3/22 – 8a | 35.97342 | 83.44126 | fracture | 280 | 75 | | |
| 3/22 – 8b | 35.97342 | 83.44126 | fracture | 310 | 85 | | |
| 3/22 – 8c | 35.97342 | 83.44126 | fracture | 320 | | | |
| 3/22 – 9a | 35.99342 | 83.44122 | fracture | 130 | 75 | | |
| 3/22 – 9b | 35.97342 | 83.44122 | fracture | 115 | 55 | | |
| 3/22 – 9c | 35.97342 | 83.44122 | fracture | 315 | | | |
| 3/22 – 9d | 35.97342 | 83.44122 | fracture | 315 | | | |
| 1 | 35.97340 | 83.44113 | oxide surface | 55 | 14 | | |
| 2 | 35.97341 | 83.44114 | fracture | 250 | 76 | | |
| 3 | 35.97341 | 83.44113 | fracture | 240 | 80 | | |

| Station | Latitude (°) | Longitude (°) | Feature | Strike | Dip | Trend | Plunge |
|---|---|---|---|---|---|---|---|
| 4 | 35.97340 | 83.44113 | oxide surface | 70 | 19 | 80 | 3 |
| 5 | 35.97342 | 83.44112 | oxide surface | 68 | 12 | 65 | 2 |
| 6 | 35.97343 | 83.44111 | oxide surface | 70 | 16 | 60 | 2 |
| 7 | 35.97343 | 83.44110 | clay surface | 71 | 20 | 85 | 10 |
| 8 | 35.97345 | 83.44110 | clay surface | 63 | 20 | 86 | 3 |
| 9 | 35.97342 | 83.44109 | oxide surface | 61 | 16 | | |
| 10 | 35.97339 | 83.44116 | oxide surface | 69 | 17 | | |
| 11 | 35.97339 | 83.44115 | fracture | 320 | | | |
| 12 | 35.97340 | 83.44116 | fracture | 320 | 90 | | |
| 13 | 35.97340 | 83.44116 | fracture | 73 | 89 | | |
| 14 | 35.97339 | 83.44114 | fracture | 66 | 20 | | |
| 15 | 35.97339 | 83.44114 | oxide surface | 66 | 16 | | |
| 16 | 35.97339 | 83.44115 | oxide surface | 67 | 15 | 60 | 5 |
| 17 | 35.97339 | 83.44109 | fracture | 318 | 70 | | |
| 18 | 35.97340 | 83.44110 | fracture | 72 | | | |
| 19 | 35.97340 | 83.44110 | fracture | 60 | | | |
| 20 | 35.97339 | 83.44110 | clay surface | 80 | 13 | | |
| 21 | 35.97339 | 83.44110 | fracture | 52 | | | |
| 22 | 35.97342 | 83.44108 | clay surface | 67 | 15 | | |
| 23 | 35.97348 | 83.44108 | fracture | 340 | | | |
| 24a | 35.97348 | 83.44108 | fracture | 58 | 16 | | |
| 24b | 35.97348 | 83.44108 | fracture | 58 | | | |
| 25 | 35.97348 | 83.44107 | clay surface | 55 | 16 | | |
| 26 | 35.97347 | 83.44109 | fracture | 65 | | | |
| 27 | 35.97347 | 83.44109 | clay surface | 65 | 15 | | |
| 28 | 35.97348 | 83.44111 | fracture | 255 | 65 | | |
| 29 | 35.97349 | 83.44111 | fracture | 245 | 65 | | |
| 30 | 35.97344 | 83.44110 | fracture | 320 | | | |
| 31 | 35.97345 | 83.44111 | clay surface | 63 | 14 | 67 | 1 |
| 32 | 35.97344 | 83.44112 | fracture | 67 | | | |
| 33 | 35.97344 | 83.44112 | fracture | 12 | | | |
| 34 | 35.97345 | 83.44115 | fracture | 54 | | | |
| 35 | 35.97345 | 83.44115 | clay surface | 60 | 14 | | |
| 36 | 35.97348 | 83.44114 | oxide surface | 64 | 13 | 70 | 2 |
| 37 | 35.97349 | 83.44114 | oxide surface | 57 | 14 | | |
| 38 | 35.97348 | 83.44116 | fracture | 70 | | | |
| 39 | 35.97345 | 83.44118 | fracture | 320 | | | |
| 40 | 35.97347 | 83.44116 | fracture | 150 | 84 | | |
| 41 | 35.97348 | 83.44119 | fracture | 55 | | | |

| Station | Latitude (°) | Longitude (°) | Feature | Strike | Dip | Trend | Plunge |
|---|---|---|---|---|---|---|---|
| 42 | 35.97348 | 83.44119 | fracture | 70 | | | |
| 43 | 35.97339 | 83.44120 | fracture | 306 | | | |
| 44 | 35.97338 | 83.44120 | fracture | 330 | | | |
| 45 | 35.97339 | 83.44120 | oxide surface | 70 | 15 | 100 | 10 |
| 46 | 35.97342 | 83.44124 | fracture | 132 | 80 | | |
| 47 | 35.97341 | 83.44125 | fracture | 138 | 80 | | |
| 48 | 35.97341 | 83.44122 | fracture | 80 | | | |
| 49 | 35.97343 | 83.44129 | clay surface | 70 | 20 | | |
| 50 | 35.97338 | 83.44130 | fracture | 15 | | | |
| 51 | 35.97338 | 83.44131 | fracture | 35 | | | |
| 52 | 35.97338 | 83.44132 | fracture | 50 | | | |
| 53 | 35.97337 | 83.44132 | clay surface | 65 | 20 | | |
| 54 | 35.97342 | 83.44130 | fracture | 55 | | | |
| 55 | 35.97342 | 83.44131 | fracture | 75 | | | |
| 56 | 35.97342 | 83.44131 | fracture | 30 | | | |
| 57 | 35.97337 | 83.44133 | fracture | 40 | | | |
| 58 | 35.97337 | 83.44134 | fracture | 46 | | | |
| 59 | 35.97340 | 83.44130 | fracture | 64 | | | |
| 61 | 35.97342 | 83.44133 | fracture | 260 | 84 | | |
| 62 | 35.97342 | 83.44135 | fracture | 72 | | | |
| 63 | 35.97338 | 83.44135 | fracture | 340 | | | |
| 64 | 35.97337 | 83.44138 | fracture | 60 | | | |
| 65 | 35.97338 | 83.44136 | fracture | 56 | | | |
| 66 | 35.97339 | 83.44138 | fracture | 65 | | | |
| 67 | 35.97340 | 83.44137 | fracture | 245 | 70 | | |
| 68 | 35.97339 | 83.44134 | fracture | 60 | | | |
| 69 | 35.97342 | 83.44144 | fracture | 305 | | | |
| 70 | 35.97342 | 83.44140 | fracture | 62 | | | |
| 71 | 35.97341 | 83.44144 | fracture | 58 | | | |
| 72 | 35.97341 | 83.44145 | fracture | 50 | | | |
| 73 | 35.97342 | 83.44147 | fracture | 320 | | | |
| 74 | 35.97342 | 83.44147 | fracture | 56 | | | |
| 75 | 35.97338 | 83.44148 | clay surface | 60 | 20 | | |
| 76 | 35.97340 | 83.44148 | fracture | 70 | | | |
| 77 | 35.97341 | 83.44148 | fracture | 62 | | | |
| 78 | 35.97341 | 83.44148 | fracture | 64 | | | |
| 79 | 35.97346 | 83.44118 | fracture | 69 | | | |
| 80 | 35.97345 | 83.44118 | fracture | 70 | | | |
| 81 | 35.97344 | 83.44120 | fracture | 54 | | | |

| Station | Latitude (°) | Longitude (°) | Feature | Strike | Dip | Trend | Plunge |
|---|---|---|---|---|---|---|---|
| 82 | 35.97345 | 83.44121 | fracture | 55 | | | |
| 83 | 35.97346 | 83.44121 | fracture | 50 | | | |
| 84a | 35.97344 | 83.44122 | fracture | 60 | | | |
| 84b | 35.97343 | 83.44122 | fracture | 70 | | | |
| 85 | 35.97345 | 83.44121 | clay surface | 65 | 11 | | |
| 86 | 35.97346 | 83.44122 | fracture | 245 | 82 | | |
| 87 | 35.97345 | 83.44122 | clay surface | 69 | 17 | | |
| 88 | 35.97345 | 83.44123 | clay surface | 62 | 11 | 63 | 2 |
| 89 | 35.97344 | 83.44123 | fracture | 52 | | | |
| 90 | 35.97346 | 83.44129 | fracture | 312 | | | |
| 91 | 35.97347 | 83.44115 | fracture | 68 | | | |
| 92 | 35.97345 | 83.44115 | clay surface | 65 | 13 | | |
| 93 | 35.97346 | 83.44115 | clay surface | 68 | 15 | | |
| 94 | 35.97346 | 83.44117 | fracture | 72 | | | |
| 95 | 35.97346 | 83.44118 | fracture | 324 | | | |
| 96 | 35.97346 | 83.44114 | clay surface | 64 | 17 | | |
| 97 | 35.97345 | 83.44129 | fracture | 62 | | | |
| 98 | 35.97345 | 83.44129 | fracture | 275 | | | |
| 99 | 35.97346 | 83.44130 | fracture | 58 | 72 | | |
| 100 | 35.97344 | 83.44131 | clay surface | 72 | 18 | 60 | 2 |
| 101 | 35.97346 | 83.44133 | fracture | 130 | 82 | | |
| 102 | 35.97345 | 83.44132 | fracture | 115 | 72 | | |
| 103 | 35.97346 | 83.44134 | clay surface | 70 | 15 | 55 | 3 |
| 104 | 35.97346 | 83.44136 | fracture | 85 | | | |
| 105 | 35.97345 | 83.44136 | fracture | 55 | | | |
| 106 | 35.97345 | 83.44136 | fracture | 50 | | | |
| 107 | 35.97346 | 83.44140 | fracture | 65 | | | |
| 108 | 35.97346 | 83.44140 | fracture | 61 | | | |
| 109 | 35.97347 | 83.44139 | fracture | 90 | | | |
| 110 | 35.97346 | 83.44139 | fracture | 160 | 73 | | |
| 111 | 35.97345 | 83.44140 | fracture | 310 | | | |
| 112a | 35.97345 | 83.44137 | fracture | 315 | | | |
| 112b | 35.97346 | 83.44137 | fracture | 60 | 80 | | |
| 113 | 35.97346 | 83.44133 | fracture | 60 | 72 | | |
| 114 | 35.97345 | 83.44130 | fracture | 58 | | | |
| 115 | 35.97344 | 83.44144 | fracture | 67 | | | |
| 116 | 35.97345 | 83.44145 | clay surface | 62 | 21 | | |
| 117 | 35.97347 | 83.44143 | fracture | 79 | | | |
| 118 | 35.97346 | 83.44143 | fracture | 83 | | | |

| Station | Latitude (°) | Longitude (°) | Feature | Strike | Dip | Trend | Plunge |
|---|---|---|---|---|---|---|---|
| 119 | 35.97345 | 83.44146 | fracture | 66 | | | |
| 120 | 35.97348 | 83.44114 | fracture | 282 | | | |
| 121 | 35.97348 | 83.44115 | clay surface | 62 | 19 | | |
| 122 | 35.97349 | 83.44116 | fracture | 315 | | | |
| 123 | 35.97349 | 83.44116 | oxide surface | 65 | 17 | | |
| 124 | 35.97347 | 83.44121 | fracture | 30 | | | |
| 125 | 35.97347 | 83.44122 | fracture | 57 | | | |
| 126 | 35.97347 | 83.44122 | fracture | 34 | | | |
| 127 | 35.97348 | 83.44119 | clay surface | 74 | 14 | | |
| 128 | 35.97346 | 83.44122 | fracture | 45 | | | |
| 129 | 35.97346 | 83.44123 | clay surface | 72 | 17 | | |
| 130 | 35.97347 | 83.44132 | fracture | 132 | 79 | | |
| 131 | 35.97347 | 83.44131 | fracture | 309 | 89 | | |
| 132 | 35.97347 | 83.44131 | fracture | 310 | 82 | | |
| 133 | 35.97347 | 83.44129 | fracture | 37 | | | |
| 134 | 35.97348 | 83.44131 | fracture | 61 | | | |
| 135 | 35.97352 | 83.44109 | fracture | 80 | | | |
| 136 | 35.97352 | 83.44108 | fracture | 245 | 70 | | |
| 137 | 35.97352 | 83.44108 | fracture | 244 | 77 | | |
| 138 | 35.97352 | 83.44109 | fracture | 275 | | | |
| 139 | 35.97353 | 83.44109 | fracture | 282 | | | |
| 140 | 35.97353 | 83.44108 | fracture | 335 | 52 | | |
| 141 | 35.97351 | 83.44107 | fracture | 312 | | | |
| 142 | 35.97359 | 83.44107 | clay surface | 58 | 40 | | |

X-ray diffraction peaks from fresh Sevier Shale. Relative intensity is scaled to peak number 8. deg—degrees; ang—angstroms; cps—counts per second.

| Peak No. | 2-theta (deg) | D-spacing (ang.) | Intensity (cps) | Rel. Intensity |
|---|---|---|---|---|
| 1 | 8.9062 | 9.92082 | 983.21 | 0.01335 |
| 2 | 17.7001 | 5.00675 | 1186.94 | 0.01612 |
| 3 | 19.7389 | 4.49396 | 3373.99 | 0.04582 |
| 4 | 20.8954 | 4.24777 | 13481.83 | 0.18309 |
| 5 | 21.2634 | 4.17508 | 1454.89 | 0.01976 |
| 6 | 23.1323 | 3.84182 | 4901.35 | 0.06656 |
| 7 | 25.3296 | 3.51331 | 718.76 | 0.00976 |
| 8 | 26.6978 | 3.33628 | 73633.29 | 1.00000 |
| 9 | 27.9588 | 3.18860 | 895.37 | 0.01216 |
| 10 | 29.4857 | 3.02686 | 69094.01 | 0.93835 |
| 11 | 31.5229 | 2.83575 | 1538.72 | 0.02090 |
| 12 | 34.9578 | 2.56457 | 2908.63 | 0.03950 |
| 13 | 36.0632 | 2.48846 | 8308.48 | 0.11284 |
| 14 | 36.5776 | 2.45463 | 6255.09 | 0.08495 |
| 15 | 39.5235 | 2.27820 | 16263.42 | 0.22087 |
| 16 | 40.3627 | 2.23275 | 2655.64 | 0.03607 |
| 17 | 41.1004 | 2.19436 | 293.84 | 0.00399 |
| 18 | 42.5170 | 2.12447 | 4719.40 | 0.06409 |
| 19 | 43.2526 | 2.09003 | 12291.27 | 0.16693 |
| 20 | 45.8751 | 1.97646 | 2912.66 | 0.03956 |
| 21 | 47.2072 | 1.92375 | 3310.75 | 0.04496 |
| 22 | 47.6114 | 1.90836 | 12655.31 | 0.17187 |
| 23 | 48.6071 | 1.87156 | 13307.62 | 0.18073 |
| 24 | 50.2090 | 1.81554 | 11684.89 | 0.15869 |
| 25 | 53.3122 | 1.71695 | 394.14 | 0.00535 |
| 26 | 54.9410 | 1.66984 | 3392.05 | 0.04607 |
| 27 | 55.3959 | 1.65719 | 1225.21 | 0.01664 |
| 28 | 55.8399 | 1.64506 | 377.48 | 0.00513 |
| 29 | 56.6665 | 1.62301 | 2187.99 | 0.02971 |
| 30 | 57.5067 | 1.60128 | 5198.02 | 0.07059 |
| 31 | 60.0373 | 1.53969 | 7384.98 | 0.10029 |
| 32 | 60.7836 | 1.52257 | 3609.00 | 0.04901 |
| 33 | 61.1177 | 1.51504 | 1475.04 | 0.02003 |
| 34 | 61.4829 | 1.50691 | 1936.77 | 0.02630 |
| 35 | 61.7684 | 1.50063 | 1451.40 | 0.01971 |
| 36 | 63.1538 | 1.47101 | 1124.46 | 0.01527 |
| 37 | 64.1045 | 1.45146 | 1598.68 | 0.02171 |
| 38 | 64.7725 | 1.43810 | 3648.15 | 0.04954 |
| 39 | 65.7371 | 1.41932 | 1860.14 | 0.02526 |
| 40 | 67.8131 | 1.38083 | 4684.33 | 0.06362 |
| 41 | 68.2128 | 1.37371 | 6052.79 | 0.08220 |
| 42 | 68.3811 | 1.37074 | 3279.09 | 0.04453 |

X-ray diffraction peaks from shale chips at site DL-5. Relative intensity is scaled to peak number 9. deg—degrees; ang—angstroms; cps—counts per second.

| Peak no. | 2-theta(deg) | d(ang.) | Intensity (cps) | Rel. Intensity |
|---|---|---|---|---|
| 1 | 8.8465 | 9.98757 | 1621.86 | 0.099182 |
| 2 | 11.6314 | 7.60180 | 2141.09 | 0.130935 |
| 3 | 17.8336 | 4.96955 | 1452.65 | 0.088834 |
| 4 | 19.8508 | 4.46887 | 9984.84 | 0.610606 |
| 5 | 20.9178 | 4.24326 | 1917.24 | 0.117246 |
| 6 | 21.2838 | 4.17112 | 2966.49 | 0.181411 |
| 7 | 24.4549 | 3.63695 | 617.62 | 0.037770 |
| 8 | 25.3173 | 3.51499 | 2615.64 | 0.159955 |
| 9 | 26.6677 | 3.33997 | 16352.34 | 1.000000 |
| 10 | 33.4987 | 2.67287 | 437.03 | 0.026726 |
| 11 | 34.8842 | 2.56982 | 8089.00 | 0.494669 |
| 12 | 36.6785 | 2.44811 | 1449.70 | 0.088654 |
| 13 | 37.6450 | 2.38745 | 2518.23 | 0.153998 |
| 14 | 40.3166 | 2.23519 | 967.07 | 0.059140 |
| 15 | 42.5163 | 2.12450 | 1230.39 | 0.075242 |
| 16 | 45.7737 | 1.98060 | 1611.85 | 0.098570 |
| 17 | 48.0253 | 1.89287 | 803.20 | 0.049118 |
| 18 | 50.1964 | 1.81597 | 2175.03 | 0.133010 |
| 19 | 55.1238 | 1.66473 | 1380.25 | 0.084407 |
| 20 | 60.0009 | 1.54054 | 996.90 | 0.060964 |
| 21 | 61.7121 | 1.50187 | 3344.36 | 0.204519 |
| 22 | 62.4149 | 1.48663 | 2065.25 | 0.126297 |
| 23 | 64.1178 | 1.45120 | 318.70 | 0.019490 |
| 24 | 67.7537 | 1.38189 | 906.28 | 0.055422 |
| 25 | 68.1557 | 1.37472 | 960.13 | 0.058715 |

X-ray diffraction peaks from fissure-filling material DL-6-02 at site DL-6. Relative intensity is scaled to peak number 8. deg—degrees; ang—angstroms; cps—counts per second.

| Peak No. | 2-theta (deg) | D-spacing (ang.) | Intensity (cps) | Rel. Intensity |
|---|---|---|---|---|
| 1 | 8.3919 | 10.52758 | 2987.69 | 0.162523 |
| 2 | 11.7130 | 7.54901 | 3091.78 | 0.168185 |
| 3 | 17.2371 | 5.14015 | 1037.37 | 0.056430 |
| 4 | 20.3552 | 4.35927 | 3278.36 | 0.178335 |
| 5 | 20.5389 | 4.32068 | 1543.20 | 0.083946 |
| 6 | 20.7166 | 4.28401 | 1408.75 | 0.076633 |
| 7 | 24.4281 | 3.64089 | 2138.40 | 0.116324 |
| 8 | 26.0807 | 3.41380 | 18383.19 | 1.000000 |
| 9 | 36.0488 | 2.48942 | 748.35 | 0.040708 |
| 10 | 41.8215 | 2.15818 | 301.29 | 0.016389 |
| 11 | 44.4518 | 2.03638 | 1506.12 | 0.081929 |
| 12 | 44.9227 | 2.01612 | 1228.89 | 0.066849 |
| 13 | 49.6231 | 1.83560 | 1044.53 | 0.056820 |
| 14 | 52.7563 | 1.73372 | 224.32 | 0.012202 |
| 15 | 54.4935 | 1.68248 | 458.09 | 0.024919 |
| 16 | 59.5010 | 1.55228 | 902.47 | 0.049092 |
| 17 | 60.2447 | 1.53489 | 510.09 | 0.027748 |
| 18 | 61.7640 | 1.50073 | 212.23 | 0.011545 |
| 19 | 63.0624 | 1.47292 | 223.62 | 0.012164 |
| 20 | 67.7088 | 1.38270 | 333.25 | 0.018128 |

X-ray diffraction peaks from clay fault-gouge material at site DL-6. Relative intensity is scaled to peak number 8. deg—degrees; ang—angstroms; cps—counts per second.

| Peak No. | 2-theta (deg) | D-spacing (ang.) | Intensity (cps) | Rel. Intensity |
|---|---|---|---|---|
| 1 | 5.6704 | 15.57278 | 2804.81 | 0.283514 |
| 2 | 11.8116 | 7.48624 | 4495.51 | 0.454412 |
| 3 | 17.7403 | 4.99549 | 775.87 | 0.078426 |
| 4 | 19.3348 | 4.58697 | 566.91 | 0.057304 |
| 5 | 20.2939 | 4.37229 | 2612.62 | 0.264087 |
| 6 | 24.4273 | 3.64099 | 4028.65 | 0.407221 |
| 7 | 26.0963 | 3.41180 | 4711.94 | 0.476289 |
| 8 | 26.1756 | 3.40164 | 9893.02 | 1.000000 |
| 9 | 34.3514 | 2.60845 | 364.68 | 0.036862 |
| 10 | 35.9358 | 2.49699 | 764.25 | 0.077251 |
| 11 | 41.9214 | 2.15326 | 769.95 | 0.077828 |
| 12 | 44.9789 | 2.01374 | 750.57 | 0.075869 |
| 13 | 49.5870 | 1.83685 | 1315.64 | 0.132987 |
| 14 | 54.3898 | 1.68545 | 585.24 | 0.059157 |
| 15 | 54.6936 | 1.67680 | 612.91 | 0.061954 |
| 16 | 59.4744 | 1.55292 | 1110.27 | 0.112228 |
| 17 | 67.3086 | 1.38994 | 748.32 | 0.075641 |
| 18 | 67.7441 | 1.38207 | 966.25 | 0.097670 |

X-ray diffraction peaks from high, light-colored areas at Taylor Farm, near Lyerly, Georgia. Relative intensity is scaled to peak number 6. deg—degrees; ang—angstroms; cps—counts per second.

| Peak No. | 2-theta (deg) | D-spacing (ang.) | Intensity (cps) | Rel. Intensity |
|---|---|---|---|---|
| 1 | 13.8948 | 6.36816 | 135.34 | 0.000506 |
| 2 | 19.8300 | 4.47351 | 910.64 | 0.003408 |
| 3 | 20.9417 | 4.23847 | 54989.88 | 0.205769 |
| 4 | 24.0973 | 3.69011 | 1728.30 | 0.006467 |
| 5 | 25.3752 | 3.50709 | 1951.80 | 0.007304 |
| 6 | 26.7091 | 3.33489 | 267241.01 | 1.000000 |
| 7 | 27.5040 | 3.24029 | 962.78 | 0.003603 |
| 8 | 34.9244 | 2.56695 | 623.47 | 0.002333 |
| 9 | 36.6188 | 2.45196 | 22056.04 | 0.082532 |
| 10 | 39.5528 | 2.27658 | 15828.36 | 0.059229 |
| 11 | 40.3758 | 2.23205 | 9035.36 | 0.033810 |
| 12 | 42.5385 | 2.12344 | 13568.23 | 0.050772 |
| 13 | 45.8779 | 1.97635 | 11137.55 | 0.041676 |
| 14 | 48.0936 | 1.89034 | 364.84 | 0.001365 |
| 15 | 50.2279 | 1.81490 | 35636.34 | 0.133349 |
| 16 | 50.6940 | 1.79930 | 821.01 | 0.003072 |
| 17 | 53.8152 | 1.70208 | 405.53 | 0.001517 |
| 18 | 54.3368 | 1.68697 | 302.53 | 0.001132 |
| 19 | 54.9508 | 1.66956 | 11378.97 | 0.042579 |
| 20 | 55.4009 | 1.65706 | 3737.14 | 0.013984 |
| 21 | 57.3313 | 1.60576 | 612.79 | 0.002293 |
| 22 | 60.0433 | 1.53955 | 32108.04 | 0.120146 |
| 23 | 61.9821 | 1.49597 | 394.54 | 0.001476 |
| 24 | 64.1021 | 1.45151 | 3950.19 | 0.014781 |
| 25 | 65.8675 | 1.41682 | 1129.53 | 0.004227 |
| 26 | 67.8130 | 1.38083 | 14851.74 | 0.055574 |
| 27 | 68.2105 | 1.37375 | 14871.39 | 0.055648 |
| 28 | 68.3955 | 1.37048 | 11781.50 | 0.044086 |

X-ray diffraction peaks from low, dark-colored areas at Taylor Farm, near Lyerly, Georgia. Relative intensity is scaled to peak number 4. deg—degrees; ang—angstroms; cps—counts per second.

| Peak No. | 2-theta (deg) | D-spacing (ang.) | Intensity (cps) | Rel. Intensity |
|---|---|---|---|---|
| 1 | 19.8971 | 4.45859 | 936.93 | 0.003629 |
| 2 | 21.0251 | 4.22185 | 61878.90 | 0.239707 |
| 3 | 24.2092 | 3.67331 | 1977.65 | 0.007661 |
| 4 | 26.8217 | 3.32115 | 258144.23 | 1.000000 |
| 5 | 27.6307 | 3.22572 | 1250.33 | 0.004844 |
| 6 | 27.7700 | 3.20986 | 523.82 | 0.002029 |
| 7 | 29.5779 | 3.01764 | 3606.08 | 0.013969 |
| 8 | 30.9039 | 2.89112 | 305.19 | 0.001182 |
| 9 | 35.5294 | 2.52461 | 571.54 | 0.002214 |
| 10 | 36.7234 | 2.44522 | 23120.56 | 0.089565 |
| 11 | 39.6371 | 2.27193 | 18699.70 | 0.072439 |
| 12 | 40.4639 | 2.22739 | 8345.86 | 0.032330 |
| 13 | 41.2650 | 2.18599 | 448.94 | 0.001739 |
| 14 | 42.6138 | 2.11986 | 13978.41 | 0.054150 |
| 15 | 43.3262 | 2.08664 | 521.80 | 0.002021 |
| 16 | 45.9578 | 1.97310 | 8791.12 | 0.034055 |
| 17 | 47.7391 | 1.90355 | 316.75 | 0.001227 |
| 18 | 48.1462 | 1.88840 | 421.22 | 0.001632 |
| 19 | 48.6986 | 1.86826 | 432.21 | 0.001674 |
| 20 | 50.2987 | 1.81251 | 35383.82 | 0.137070 |
| 21 | 50.7554 | 1.79727 | 912.93 | 0.003537 |
| 22 | 54.3044 | 1.68790 | 237.68 | 0.000921 |
| 23 | 55.0267 | 1.66744 | 11936.57 | 0.046240 |
| 24 | 55.4866 | 1.65470 | 4339.62 | 0.016811 |
| 25 | 57.5182 | 1.60099 | 597.08 | 0.002313 |
| 26 | 60.1088 | 1.53803 | 21137.97 | 0.081884 |
| 27 | 61.0019 | 1.51764 | 249.02 | 0.000965 |
| 28 | 61.8271 | 1.49935 | 251.29 | 0.000973 |
| 29 | 64.1700 | 1.45014 | 4234.05 | 0.016402 |
| 30 | 65.8941 | 1.41631 | 1039.03 | 0.004025 |
| 31 | 67.8822 | 1.37959 | 12098.86 | 0.046869 |
| 32 | 68.2862 | 1.37241 | 14801.37 | 0.057338 |
| 33 | 68.4437 | 1.36963 | 23147.73 | 0.089670 |

X-ray diffraction peaks from sand dike sediment at the Sand Dikes site along the Chattooga River, near Lyerly, Georgia. Relative intensity is scaled to peak number 9. deg—degrees; ang—angstroms; cps—counts per second.

| Peak No. | 2-theta (deg) | d-spacing (ang.) | Intensity (cps) | Rel. Intensity |
|---|---|---|---|---|
| 1 | 17.8999 | 4.95128 | 488.99 | 0.001762 |
| 2 | 19.7915 | 4.48213 | 3063.05 | 0.011038 |
| 3 | 20.6285 | 4.30212 | 6079.42 | 0.021907 |
| 4 | 20.7661 | 4.27391 | 10442.15 | 0.037628 |
| 5 | 20.9163 | 4.24356 | 76743.26 | 0.276543 |
| 6 | 24.1088 | 3.68837 | 2206.59 | 0.007951 |
| 7 | 25.3519 | 3.51026 | 196.40 | 0.000708 |
| 8 | 26.5435 | 3.35533 | 73500.02 | 0.264856 |
| 9 | 26.7185 | 3.33375 | 277509.27 | 1.000000 |
| 10 | 27.5239 | 3.23799 | 1652.65 | 0.005955 |
| 11 | 27.9162 | 3.19337 | 1780.78 | 0.006417 |
| 12 | 34.7943 | 2.57625 | 2172.15 | 0.007827 |
| 13 | 36.5971 | 2.45337 | 57920.50 | 0.208716 |
| 14 | 39.5479 | 2.27685 | 28246.67 | 0.101786 |
| 15 | 40.3491 | 2.23347 | 18714.66 | 0.067438 |
| 16 | 42.5262 | 2.12403 | 18114.83 | 0.065276 |
| 17 | 45.8620 | 1.97699 | 16547.92 | 0.059630 |
| 18 | 50.2037 | 1.81572 | 47333.09 | 0.170564 |
| 19 | 50.6746 | 1.79995 | 3736.44 | 0.013464 |
| 20 | 54.9414 | 1.66982 | 9933.80 | 0.035796 |
| 21 | 55.2478 | 1.66129 | 648.60 | 0.002337 |
| 22 | 55.3998 | 1.65709 | 4572.65 | 0.016477 |
| 23 | 57.3099 | 1.60631 | 1443.20 | 0.005201 |
| 24 | 60.0071 | 1.54040 | 33896.46 | 0.122145 |
| 25 | 61.6241 | 1.50380 | 819.92 | 0.002955 |
| 26 | 64.0975 | 1.45161 | 6230.43 | 0.022451 |
| 27 | 65.8360 | 1.41742 | 1324.56 | 0.004773 |
| 28 | 67.7877 | 1.38128 | 22614.78 | 0.081492 |
| 29 | 68.1949 | 1.37402 | 23569.54 | 0.084932 |
| 30 | 68.3638 | 1.37104 | 23733.31 | 0.085523 |

X-ray diffraction peaks from source bed sediment at the Sand Dikes site along the Chattooga River, near Lyerly, Georgia. Relative intensity is scaled to peak number 10. deg—degrees; ang—angstroms; cps—counts per second.

| Peak No. | 2-theta (deg) | d-spacing (ang.) | Intensity (cps) | Rel. Intensity |
|---|---|---|---|---|
| 1 | 4.9399 | 17.87378 | 1805.16 | 0.005756 |
| 2 | 5.2085 | 16.95258 | 2604.53 | 0.008304 |
| 3 | 6.5106 | 13.56481 | 1647.62 | 0.005253 |
| 4 | 18.4080 | 4.81577 | 162.79 | 0.000519 |
| 5 | 19.7966 | 4.48100 | 2661.33 | 0.008486 |
| 6 | 20.8151 | 4.26397 | 33377.58 | 0.106423 |
| 7 | 20.9326 | 4.24030 | 60744.71 | 0.193682 |
| 8 | 21.9776 | 4.04099 | 2472.83 | 0.007885 |
| 9 | 24.1008 | 3.68959 | 2660.15 | 0.008482 |
| 10 | 26.7376 | 3.33140 | 313630.64 | 1.000000 |
| 11 | 27.5506 | 3.23491 | 1212.17 | 0.003865 |
| 12 | 27.9744 | 3.18686 | 947.99 | 0.003023 |
| 13 | 34.8258 | 2.57399 | 2243.84 | 0.007154 |
| 14 | 36.5942 | 2.45356 | 23036.63 | 0.073451 |
| 15 | 36.6612 | 2.44923 | 15042.38 | 0.047962 |
| 16 | 39.5635 | 2.27599 | 18440.26 | 0.058796 |
| 17 | 40.3809 | 2.23178 | 9535.02 | 0.030402 |
| 18 | 41.8437 | 2.15708 | 901.92 | 0.002876 |
| 19 | 42.5247 | 2.12410 | 12471.57 | 0.039765 |
| 20 | 45.0886 | 2.00909 | 490.85 | 0.001565 |
| 21 | 45.8644 | 1.97689 | 12940.61 | 0.041261 |
| 22 | 50.2027 | 1.81575 | 54704.34 | 0.174423 |
| 23 | 53.7499 | 1.70399 | 309.97 | 0.000988 |
| 24 | 54.3598 | 1.68631 | 214.27 | 0.000683 |
| 25 | 54.9382 | 1.66991 | 11825.01 | 0.037704 |
| 26 | 55.3998 | 1.65709 | 6601.42 | 0.021048 |
| 27 | 57.2647 | 1.60747 | 623.95 | 0.001989 |
| 28 | 60.0540 | 1.53931 | 34549.62 | 0.110160 |
| 29 | 61.8037 | 1.49986 | 1914.02 | 0.006103 |
| 30 | 64.0851 | 1.45186 | 4604.69 | 0.014682 |
| 31 | 65.8403 | 1.41734 | 802.03 | 0.002557 |
| 32 | 67.8084 | 1.38091 | 16074.91 | 0.051254 |
| 33 | 68.2055 | 1.37384 | 16763.40 | 0.053449 |
| 34 | 68.3640 | 1.37104 | 12349.99 | 0.039377 |

X-ray diffraction peaks from host bed sediment at the Sand Dikes site along the Chattooga River, near Lyerly, Georgia. Relative intensity is scaled to peak number 8. deg—degrees; ang—angstroms; cps—counts per second.

| Peak No. | 2-theta (deg) | d-spacing (ang.) | Intensity (cps) | Rel. Intensity |
|---|---|---|---|---|
| 1 | 5.9146 | 14.93025 | 458.94 | 0.001571 |
| 2 | 19.6706 | 4.50941 | 3720.57 | 0.012739 |
| 3 | 20.6396 | 4.29984 | 11775.82 | 0.040321 |
| 4 | 20.7574 | 4.27569 | 27270.57 | 0.093375 |
| 5 | 20.8525 | 4.25640 | 45804.17 | 0.156834 |
| 6 | 24.0098 | 3.70335 | 2279.01 | 0.007803 |
| 7 | 26.5326 | 3.35668 | 53784.07 | 0.184157 |
| 8 | 26.6232 | 3.34546 | 292054.89 | 1.000000 |
| 9 | 27.4157 | 3.25053 | 997.55 | 0.003416 |
| 10 | 34.9362 | 2.56611 | 2547.48 | 0.008723 |
| 11 | 35.5238 | 2.52500 | 550.31 | 0.001884 |
| 12 | 36.5310 | 2.45766 | 33216.09 | 0.113732 |
| 13 | 39.4524 | 2.28214 | 36513.76 | 0.125024 |
| 14 | 40.2721 | 2.23756 | 12026.55 | 0.041179 |
| 15 | 41.0548 | 2.19669 | 332.94 | 0.001140 |
| 16 | 42.4407 | 2.12811 | 16678.81 | 0.057108 |
| 17 | 45.7695 | 1.98077 | 13548.67 | 0.046391 |
| 18 | 47.1261 | 1.92687 | 461.14 | 0.001579 |
| 19 | 50.1215 | 1.81851 | 34786.83 | 0.119111 |
| 20 | 50.6026 | 1.80234 | 1703.91 | 0.005834 |
| 21 | 53.4858 | 1.71178 | 514.65 | 0.001762 |
| 22 | 54.8527 | 1.67231 | 13330.50 | 0.045644 |
| 23 | 55.3031 | 1.65976 | 4504.51 | 0.015424 |
| 24 | 59.9441 | 1.54186 | 33322.79 | 0.114098 |
| 25 | 61.7231 | 1.50162 | 1631.50 | 0.005586 |
| 26 | 64.0234 | 1.45311 | 5148.54 | 0.017629 |
| 27 | 65.7863 | 1.41837 | 1075.91 | 0.003684 |
| 28 | 67.7210 | 1.38248 | 16331.40 | 0.055919 |
| 29 | 68.1317 | 1.37514 | 23737.21 | 0.081277 |
| 30 | 68.3019 | 1.37213 | 22082.57 | 0.075611 |

X-ray diffraction peaks from elutriated sand dike sediment at the Sand Dikes site along the Chattooga River, near Lyerly, Georgia. Relative intensity is scaled to peak number 9. deg—degrees; ang—angstroms; cps—counts per second.

| Peak No. | 2-theta (deg) | D-spacing (ang.) | Intensity (cps) | Rel. Intensity |
|---|---|---|---|---|
| 1 | 6.0031 | 14.71048 | 362.70 | 0.002708 |
| 2 | 8.6512 | 10.21268 | 1325.24 | 0.009896 |
| 3 | 12.1559 | 7.27492 | 1252.71 | 0.009354 |
| 4 | 17.6046 | 5.03368 | 1919.32 | 0.014332 |
| 5 | 19.5061 | 4.54707 | 1344.60 | 0.010040 |
| 6 | 20.6825 | 4.29100 | 30627.47 | 0.228699 |
| 7 | 24.7093 | 3.60009 | 1095.63 | 0.008181 |
| 8 | 25.0940 | 3.54575 | 2062.43 | 0.015400 |
| 9 | 26.4689 | 3.36461 | 133920.47 | 1.000000 |
| 10 | 27.2209 | 3.27334 | 3435.48 | 0.025653 |
| 11 | 27.7698 | 3.20987 | 1897.40 | 0.014168 |
| 12 | 34.7089 | 2.58239 | 870.68 | 0.006501 |
| 13 | 36.3793 | 2.46756 | 8333.23 | 0.062225 |
| 14 | 39.3045 | 2.29038 | 6059.71 | 0.045249 |
| 15 | 40.1272 | 2.24531 | 3885.38 | 0.029013 |
| 16 | 42.2790 | 2.13587 | 8077.60 | 0.060316 |
| 17 | 45.6680 | 1.98494 | 2718.90 | 0.020302 |
| 18 | 47.8399 | 1.89977 | 492.33 | 0.003676 |
| 19 | 49.9791 | 1.82335 | 12942.92 | 0.096646 |
| 20 | 50.4217 | 1.80838 | 744.82 | 0.005562 |
| 21 | 54.7319 | 1.67572 | 4075.60 | 0.030433 |
| 22 | 55.1702 | 1.66344 | 936.02 | 0.006989 |
| 23 | 59.8189 | 1.54479 | 7831.29 | 0.058477 |
| 24 | 61.4604 | 1.50741 | 241.12 | 0.001800 |
| 25 | 63.8756 | 1.45611 | 1048.21 | 0.007827 |
| 26 | 67.6050 | 1.38457 | 4213.59 | 0.031463 |
| 27 | 68.0048 | 1.37740 | 4370.53 | 0.032635 |
| 28 | 68.1742 | 1.37439 | 3493.82 | 0.026089 |

X-ray diffraction peaks from elutriated source bed sediment at the Sand Dikes site along the Chattooga River, near Lyerly, Georgia. Relative intensity is scaled to peak number 9. deg—degrees; ang—angstroms; cps—counts per second.

| Peak No. | 2-theta (deg) | D-spacing (ang.) | Intensity (cps) | Rel. Intensity |
|---|---|---|---|---|
| 1 | 5.8517 | 15.09054 | 446.57 | 0.005836 |
| 2 | 8.6358 | 10.23078 | 2380.55 | 0.031109 |
| 3 | 12.1836 | 7.25846 | 1094.36 | 0.014301 |
| 4 | 17.5557 | 5.04759 | 2538.21 | 0.033169 |
| 5 | 19.5624 | 4.53409 | 956.66 | 0.012502 |
| 6 | 20.5328 | 4.32196 | 4707.69 | 0.061520 |
| 7 | 20.6807 | 4.29138 | 16454.33 | 0.215024 |
| 8 | 24.8493 | 3.58012 | 329.03 | 0.004300 |
| 9 | 26.4671 | 3.36484 | 76523.28 | 1.000000 |
| 10 | 34.5882 | 2.59113 | 633.34 | 0.008276 |
| 11 | 35.8316 | 2.50401 | 248.66 | 0.003249 |
| 12 | 36.3839 | 2.46726 | 5141.03 | 0.067183 |
| 13 | 39.2977 | 2.29077 | 3140.07 | 0.041034 |
| 14 | 40.1271 | 2.24531 | 3099.64 | 0.040506 |
| 15 | 42.2887 | 2.13540 | 2965.41 | 0.038752 |
| 16 | 45.2182 | 2.00363 | 1055.43 | 0.013792 |
| 17 | 45.6259 | 1.98667 | 2377.52 | 0.031069 |
| 18 | 49.9834 | 1.82321 | 5340.66 | 0.069791 |
| 19 | 54.6969 | 1.67671 | 1529.65 | 0.019989 |
| 20 | 59.8031 | 1.54516 | 3790.59 | 0.049535 |
| 21 | 63.9002 | 1.45561 | 562.42 | 0.007350 |
| 22 | 67.5955 | 1.38474 | 1899.29 | 0.024820 |
| 23 | 68.0008 | 1.37747 | 2372.47 | 0.031003 |
| 24 | 68.1642 | 1.37457 | 1833.95 | 0.023966 |

X-ray diffraction peaks from elutriated host bed sediment at the Sand Dikes site along the Chattooga River, near Lyerly, Georgia. Relative intensity is scaled to peak number 6. deg—degrees; ang—angstroms; cps—counts per second.

| Peak No. | 2-theta (deg) | D-spacing (ang.) | Intensity (cps) | Rel. Intensity |
|---|---|---|---|---|
| 1 | 8.6511 | 10.21275 | 1353.90 | 0.032360 |
| 2 | 12.1463 | 7.28065 | 819.59 | 0.019589 |
| 3 | 17.5956 | 5.03624 | 1683.94 | 0.040248 |
| 4 | 19.4958 | 4.54944 | 597.95 | 0.014292 |
| 5 | 20.6567 | 4.29632 | 11029.90 | 0.263629 |
| 6 | 26.4608 | 3.36563 | 41838.73 | 1.000000 |
| 7 | 27.2687 | 3.26771 | 1089.68 | 0.026045 |
| 8 | 27.7721 | 3.20962 | 2333.49 | 0.055773 |
| 9 | 31.0420 | 2.87857 | 453.45 | 0.010838 |
| 10 | 34.8560 | 2.57183 | 520.51 | 0.012441 |
| 11 | 36.3597 | 2.46884 | 2224.18 | 0.053161 |
| 12 | 39.2897 | 2.29121 | 1318.85 | 0.031522 |
| 13 | 40.1043 | 2.24654 | 1021.99 | 0.024427 |
| 14 | 42.2861 | 2.13553 | 2348.67 | 0.056136 |
| 15 | 45.5530 | 1.98968 | 727.87 | 0.017397 |
| 16 | 49.9847 | 1.82316 | 2606.20 | 0.062292 |
| 17 | 54.7043 | 1.67650 | 1136.04 | 0.027153 |
| 18 | 55.1043 | 1.66527 | 243.79 | 0.005827 |
| 19 | 59.8111 | 1.54497 | 2051.43 | 0.049032 |
| 20 | 63.8761 | 1.45610 | 380.43 | 0.009093 |
| 21 | 67.6058 | 1.38456 | 1025.64 | 0.024514 |
| 22 | 67.9986 | 1.37751 | 1274.16 | 0.030454 |
| 23 | 68.1565 | 1.37471 | 776.49 | 0.018559 |

Grain size analysis data from the sand dike, source bed, and host bed sediments at the Sand Dikes site along the Chattooga River, near Lyerly, Georgia.

**DIKE**

| Sieve No. | Held on (m) | Raw Wt. (g) | Cumulative Wt. | Cumulative % | Individual % | % Finer than |
|---|---|---|---|---|---|---|
| >18 | 0.001000 | 6.03 | 6.03 | 2.90 | 2.90 | 97.10 |
| 25 | 0.000710 | 6.55 | 12.58 | 6.05 | 3.15 | 93.95 |
| 35 | 0.000500 | 9.1 | 21.68 | 10.43 | 4.38 | 89.57 |
| 45 | 0.000355 | 23.58 | 45.26 | 21.77 | 11.34 | 78.23 |
| 60 | 0.000250 | 41.87 | 87.13 | 41.91 | 20.14 | 58.09 |
| 120 | 0.000125 | 60.74 | 147.87 | 71.12 | 29.21 | 28.88 |
| 170 | 0.000090 | 14.73 | 162.6 | 78.20 | 7.08 | 21.80 |
| 230 | 0.000063 | 20.45 | 183.05 | 88.04 | 9.84 | 11.96 |
| pan | | 24.87 | 207.92 | 100.00 | 11.96 | 0.00 |

**SOURCE BED**

| Sieve No. | Held on (m) | Raw Wt. (g) | Cumulative Wt. | Cumulative % | Ind. % | % Finer than |
|---|---|---|---|---|---|---|
| >18 | 0.001000 | 5.84 | 5.84 | 3.73 | 3.73 | 96.27 |
| 25 | 0.000710 | 2.37 | 8.21 | 5.24 | 1.51 | 94.76 |
| 35 | 0.000500 | 4.15 | 12.36 | 7.89 | 2.65 | 92.11 |
| 45 | 0.000355 | 15.3 | 27.66 | 17.65 | 9.76 | 82.35 |
| 60 | 0.000250 | 27.48 | 55.14 | 35.19 | 17.54 | 64.81 |
| 120 | 0.000125 | 50.62 | 105.76 | 67.49 | 32.30 | 32.51 |
| 170 | 0.000090 | 13 | 118.76 | 75.78 | 8.30 | 24.22 |
| 230 | 0.000063 | 14.71 | 133.47 | 85.17 | 9.39 | 14.83 |
| pan | | 23.24 | 156.71 | 100.00 | 14.83 | 0.00 |

**HOST BED**

| Sieve No. | Held on (m) | Raw Wt. (g) | Cumulative Wt. | Cumulative % | Ind. % | % Finer than |
|---|---|---|---|---|---|---|
| >18 | 0.001000 | 2.02 | 2.02 | 2.12 | 2.12 | 97.88 |
| 25 | 0.000710 | 3.1 | 5.12 | 5.37 | 3.25 | 94.63 |
| 35 | 0.000500 | 4.63 | 9.75 | 10.23 | 4.86 | 89.77 |
| 45 | 0.000355 | 7.38 | 17.13 | 17.97 | 7.74 | 82.03 |
| 60 | 0.000250 | 13.76 | 30.89 | 32.40 | 14.43 | 67.60 |
| 120 | 0.000125 | 28.7 | 59.59 | 62.51 | 30.11 | 37.49 |
| 170 | 0.000090 | 8.49 | 68.08 | 71.42 | 8.91 | 28.58 |
| 230 | 0.000063 | 9.12 | 77.2 | 80.98 | 9.57 | 19.02 |
| pan | | 18.13 | 95.33 | 100.00 | 19.02 | 0.00 |

## *VITA*

Kathleen Frances Warrell was born in Atlanta, Georgia, to the parents Thomas and Marie Warrell. She attended Berkeley Lake Elementary School, continuing to Duluth Middle School and graduated from Duluth High School in 2008. She participated in a dual-enrollment program at Georgia Perimeter College during her senior year of high school, where she took her first geology course and decided to major in geology. She began attending The Georgia Institute of Technology in 2008, majoring in Earth and Atmospheric Sciences (it was the most similar major to geology offered). In 2010, Kathleen began undergraduate research with Dr. Josef Dufek studying gravity currents in a laboratory setting. Hungry for a more field-based research experience, she started a second undergraduate research project under the direction of Dr. Kurt Frankel with a fellowship from the Keck Geology Consortium, which allowed her to map terraces in Colorado. She was awarded the Rutt Bridges Fellowship for Undergraduate Research Initiative for her work. Kathleen graduated with a Bachelor of Science degree in 2011. Dr. Frankel encouraged Kathleen to apply to graduate schools for a Master of Science degree, and suggested that the University of Tennessee-Knoxville was a good fit. She applied to work with Dr. Robert D. Hatcher, Jr., for her Master of Science degree and was accepted. She was offered the George Swingle Fellowship for Excellence in Geological Field Research to study paleoseismic features in the East Tennessee Seismic Zone.